PFG

Photogrammetrie Fernerkundung Geoinformation

Journal for Photogrammetry, Remote Sensing and Geoinformation Science

Organ der Deutschen Gesellschaft für Photogrammetrie, Fernerkundung und Geoinformation (DGPF) e. V.

Jahrgang 2016, Heft 3

E. Schweizerbart'sche Verlagsbuchhandlung
(Nägele u. Obermiller) Stuttgart 2016

Deutsche Gesellschaft für Photogrammetrie, Fernerkundung
und Geoinformation (DGPF) e.V.
Gegründet 1909

Die *Deutsche Gesellschaft für Photogrammetrie, Fernerkundung und Geoinformation* (DGPF) e.V. unterstützt als Mitglieds- bzw. Trägergesellschaft die folgenden Dachverbände:

International Society
for Photogrammetry
and Remote Sensing

Deutsche Arbeits-
gemeinschaft für
Mustererkennung e.V.

GeoUnion
Alfred-Wegener-Stiftung

Herausgeber:

Präsident: Prof. Dr. Thomas Kolbe, Technische Universität München, Institut für Geodäsie, GIS und Landmanagement, Lehrstuhl für Geoinformatik, Arcisstraße 21, 80333 München, Germany, Tel. +49-89-289-23888
Geschäftsstelle: Tanja Nyc, c/o Technische Universität München, Institut für Geodäsie, GIS und Landmanagement, Lehrstuhl für Geoinformatik, Arcisstraße 21, 80333 München, Germany, Tel.: +49-89-289-22578, e-mail: geschaeftsstelle@dgpf.de

Published by: E. Schweizerbart'sche Verlagsbuchhandlung (Nägele u. Obermiller), Johannesstraße 3A, 70176 Stuttgart, Germany, Tel.: +49-711 351456-0, Fax: +49-711 351456-99, e-mail: mail@schweizerbart.de
Internet: http://www.schweizerbart.de

♾ Gedruckt auf alterungsbeständigem Papier nach ISO 9706-1994

ISSN 1432-8364 / e-ISSN 2363-7145

Science Citation Index Expanded (also known as SciSearch®) Journal Citation Reports/Science Edition
Hauptschriftleiter: Prof. Dr.-Ing. Wolfgang Kresse, Hochschule Neubrandenburg, Fachbereich Landschaftswissenschaften und Geomatik, Brodaer Straße 2, 17033 Neubrandenburg, Germany, e-mail: kresse@hs-nb.de
Schriftleiter: Prof. Dr.-Ing. Stefan Hinz, Karlsruher Institut für Technologie – KIT, Institut für Photogrammetrie und Fernerkundung, Englerstraße 7, 76131 Karlsruhe, Germany, e-mail: stefan.hinz@ipf.uni-karlsruhe.de, Prof. Dr. techn. Franz Rottensteiner, Leibniz Universität Hannover, Institut für Photogrammetrie und GeoInformation, Nienburger Straße 1, 30167 Hannover, Germany, e-mail: rottensteiner@ipi.uni-hannover.de, Prof. Dr. rer. nat. Christopher Conrad, Universität Würzburg, Institut für Geographie und Geologie, Oswald-Külpe-Weg 86, 97074 Würzburg, Germany, e-mail: christopher.conrad@uni-wuerzburg.de, Prof. Dr. rer. nat. Lars Bernard, Technische Universität Dresden, Fachrichtung Geowissenschaften, Helmholtzstraße 10, 01062 Dresden, Germany, e-mail: lars.bernard@tu-dresden.de, und Dr.-Ing. Eckhardt Seyfert, Landesvermessung und Geobasisinformation Brandenburg, Heinrich-Mann-Allee 103, 14473 Potsdam, Germany, e-mail: eckhardt.seyfert@geobasis-bb.de

Erscheinungsweise: 6 Hefte pro Jahrgang.
Bezugspreis im Abonnement: € 262,– pro Jahrgang. Mitglieder der DGPF erhalten die Zeitschrift kostenlos. Der Online-Zugang ist im regulären Subskriptionspreis enthalten.
Anzeigenverwaltung: E. Schweizerbart'sche Verlagsbuchhandlung (Nägele u. Obermiller), Johannesstraße 3A, 70176 Stuttgart, Germany, Tel.: +49-711 351456-0; Fax: +49-711 351456-99.
e-mail: mail@schweizerbart.de, Internet: http://www.schweizerbart.de
Bernhard Harzer Verlag GmbH, Westmarkstraße 59/59a, 76227 Karlsruhe, Germany, Tel.: +49-721 944020, Fax: +49-721 9440230, e-mail: Info@harzer.de, Internet: www.harzer.de
Printed in Germany by Tutte Druckerei & Verlagsservice GmbH, 94121 Salzweg, Germany.

PFG – Jahrgang 2016, Heft 3
Inhaltsverzeichnis

Originalbeiträge

Beitrag aus Wissenschaft und Praxis

Mitteilungen

Zusammenfassungen der „Originalbeiträge“ und der „Beiträge aus Wissenschaft und Praxis“ (deutsch und englisch) sind auch verfügbar unter www.dgpf.de/neu/pfg/ausgaben.htm

PFG 2016 / 3, 109 – 123
Stuttgart, Juni 2016

Article

Using Digital Aerial Photogrammetry and the Random Forest Approach to Model Forest Inventory Attributes in Beech- and Spruce-dominated Central European Forests

Christoph Straub & Christoph Stepper, Freising

Keywords: Digital aerial photographs, semi-global matching, canopy height model, random forest, forest inventory

Summary: Surface models generated using dense image matching of aerial photographs have potential for use in the area-based prediction of forest inventory attributes. Few studies have examined the impact of the forest type on the performance of models used to predict forest attributes. Moreover, with regard to central European forests, little is known about how accurately attributes other than volume and basal area can be estimated using image-based surface models. Thus, in this study, we assessed the accuracy of such estimates for five forest attributes – stem density *N*, basal area *G*, quadratic mean diameter *QMD*, volume *V*, and Lorey's mean height H_L – for a beech- and a spruce-dominated forest in northern Bavaria, Germany. These estimates were made using a workflow combining data from aerial photographs obtained from regularly scheduled surveys and field plot measurements from periodic forest inventories conducted in Bavarian state forests. Semi-Global Matching was used to derive surface models from the air photos which were normalized with terrain models from airborne laser scanning to derive canopy height models (CHM). Based on the CHM values at the respective field plots, a set of 14 predictor variables characterizing tree height distribution was computed. For the prediction, individual random forest models were trained and cross-validated separately for both test sites. With respect to relative *RMSEs*, i.e., divided by the observation means, most distinct differences were observed for the prediction of *QMD* with a slightly higher level of accuracy for the spruce-dominated forest. Best results were achieved for H_L, while poorest model performances were obtained for *N*. The relative plot-level *RMSEs* for *N*, *G*, *QMD*, *V*, and H_L were: 70.3%, 36.0%, 32.3%, 37.8%, and 12.4% for the beech-dominated and 74.9%, 35.2%, 24.9%, 33.3%, and 12.4% for the spruce-dominated forest. Thus, with the exception of *QMD*, the forest type did not considerably influence the model accuracies.

Zusammenfassung: *Verwendung von photogrammetrischen Oberflächenmodellen und Random Forest zur Modellierung forstlicher Kenngrößen in buchen- und fichtendominierten Wäldern in Mitteleuropa.* Aus Stereo-Luftbildern abgeleitete Oberflächenmodelle können für die flächige Modellierung forstlicher Kenngrößen verwendet werden. Bisher wurde der Einfluss des Waldtyps auf die Genauigkeit der Modellierung nur in wenigen Studien untersucht. Außer für die Kenngrößen Holzvolumen und Grundfläche gibt es für mitteleuropäische Wälder bisher wenig Erfahrung, mit welcher Genauigkeit forstliche Kennwerte mit bildbasierten Oberflächenmodellen modelliert werden können. Deshalb wurde in dieser Studie die Modellierungsgenauigkeit für fünf verschiedene forstliche Inventurmerkmale untersucht – Stammzahl *N*, Grundfläche *G*, quadratischer Mitteldurchmesser *QMD*, Volumen *V* und Lorey'sche Mittelhöhe H_L – sowohl für eine buchendominierte als auch für eine fichtendominierte Untersuchungsfläche im Norden von Bayern. Hierfür wurde ein Arbeitsablauf angewendet, der regelmäßig erhobene amtliche Luftbilder mit terrestrischen Stichprobenmessungen einer Forstbetriebsinventur in bayerischen Staatswaldflächen kombiniert. Die Berechnung von Oberflächenmodellen aus den Luftbildern erfolgte mittels Semi-Global Matching, welche zur Ableitung von Kronenhöhenmodellen (KHM) mit einem Geländemodell aus Laserscannermessung normalisiert wurden. Auf Grundlage der KHM wurden an den Stichprobenkreisen der Forstbetriebsinventur 14 Prädiktorvariablen zur Charakterisierung der Höhenverteilung abgeleitet. Für die Schätzung wurden einzelne Random Forest Modelle jeweils getrennt für beide Untersuchungsgebiete trainiert und validiert. Bezogen auf relative *RMSEs*, d.h. normalisiert mit dem Mittelwert der Beobachtungen, wurden die deutlichsten Unterschiede für die Schätzung des *QMD* festgestellt, mit einer etwas besseren Genauigkeit für die fichtendominierte

www.schweizerbart.de
DOI: 10.1127/pfg/2016/0292
1432-8364/16/0292 $ 3.75

Fläche. Die besten Ergebnisse wurden für die Modellierung der H_L erzielt, wohingegen die geringsten Genauigkeiten für *N* festgestellt wurden. Auf Inventurkreisebene wurden die folgenden relativen *RMSEs* für *N*, *G*, *QMD*, *V*, und H_L berechnet: 70.3%, 36.0%, 32.3%, 37.8% und 12.4% für die buchendominierte Fläche und 74.9%, 35.2%, 24.9%, 33.3% und 12.4% für den fichtendominierten Wald. Mit Ausnahme für den *QMD* hatte der Waldtyp demnach keinen maßgeblichen Einfluss auf die Genauigkeit der Modelle.

1 Introduction

Quantitative estimates of certain forest inventory attributes, such as mean tree height or timber volume per hectare, are crucial for sustainable forest management practice. At present, state forests in Bavaria, Germany, which account for 30% of the total forest area in Bavaria (Thünen-Institut 2015), are inventoried once every 10 years by the Bavarian State Forest Enterprise (BaySF) to gain quantitative information about the current state and future development of the forest. In 2015, the BaySF conducted such inventories for 73,805 hectares, i.e., 10.2% of the total state forest area (BaySF 2015). As fieldwork is time-consuming and labour-intensive, terrestrial measurements are restricted to sample plots which are distributed systematically across the state forests based on a regular 200 m × 200 m grid. The field inventories are designed for evaluations at the forest enterprise level for which characteristic values of specific forest attributes can be estimated based on statistical evidence. These key figures are very valuable for strategic planning purposes. However, information for forest stand regions, which are the smallest management units, cannot be deduced from these data. Thus, in order to support operational planning and monitoring, higher resolution information about the spatial distribution of forest characteristics, which cannot be provided by the sample plot measurements alone, would be beneficial.

Remote sensing can support such terrestrial forest inventories. Here, remotely sensed measurements are frequently used as auxiliary data that enable the generation of wall-to-wall estimates of forest inventory attributes, thus providing maps of key elements of forest structure across the entire area of interest. In particular, high-resolution canopy height models (CHMs) can be valuable auxiliary datasets for this kind of application.

Canopy height measurements from airborne laser scanning (ALS) have been used successfully in operational forest management inventories in different countries, e.g. in Norway (Næsset 2014), Finland (Maltamo & Packalen 2014), and Canada (Woods et al. 2011). The most commonly used method for modelling forest inventory attributes is the area-based approach (Næsset 2002a). For this purpose, height and density metrics describing the vertical distribution of ALS returns are related to measurements at field plots in order to train predictive models for subsequent wall-to-wall mapping. Both parametric and non-parametric approaches can be used in such modelling efforts, e.g. linear regressions (Means et al. 2000), the *k*-most similar neighbours method (Packalen & Maltamo 2007), or random forest (Yu et al. 2010). As forest management planning can benefit from species-specific data, Packalen & Maltamo (2007) combined ALS data with aerial photographs to generate area-based predictions separately for Scots pine, Norway spruce and broadleaved trees (as a group) for a managed boreal forest in Finland. A general introduction to area-based predictions using ALS and field plot data is given in Næsset (2014).

According to White et al. (2013a) there has been a growing interest in alternative technologies capable of mapping surface heights over large areas, and image-based digital surface models (DSMs) have emerged as a suitable substitute for ALS-based DSMs (White et al. 2015). Ongoing improvements in camera technology, as well as enhanced algorithms for image matching such as Semi-Global Matching (SGM; Hirschmüller 2008) have provided further stimulus for these developments (Haala & Rothermel 2012). Currently, digital aerial photogrammetry (DAP) is viable for practical forestry applications in Germany and several other European countries, since aerial photographs are updated regularly by the surveying authorities, e.g. in two- or three-year cycles in Germany (Straub & Seitz 2014) or a maximum of six-year cycles in Switzerland (Ginzler & Hobi 2015). In contrast, ALS

data are currently not updated on a regular basis by the surveying authorities.

As image-based height measurements are limited to the outer 'envelope' of the forest canopy, additional detailed information about the topography is a basic prerequisite for calculating vegetation heights above ground. Here, pre-existing ALS-based digital terrain models (DTMs) can be used to normalize the photogrammetric measurements. With respect to utilizing DAP for practical forestry applications in Germany, availability of the required ALS-based DTMs is not a limitation, since most surveying authorities have already produced DTMs based on ALS data for extensive areas, e.g. a 1 m-DTM is available for the entire state of Bavaria (LDBV 2015a).

The computation of surface models from aerial photographs has been studied for many years. In the study of Adler & Koch (1999) an automatically generated surface model was compared to manually measured elevation points for a spruce-dominated stand in southern Germany. It was found that the automatically generated surface model had a similar reliability as the manually measured height values. Several studies, conducted in Germany, Norway, and Finland, have assessed the direct estimation of stand heights from surface models derived from scanned aerial photographs (Kätsch & Stöcker 2000, Næsset 2002b, Korpela & Anttila 2004). In these studies, it was observed that, on average, stand heights were underestimated. To decrease this *bias*, Næsset (2002b) suggested a calibration with field data. Kätsch & Stöcker (2000) mentioned the difficulty to obtain reliable height measurements of the terrain (bare Earth) from the aerial photographs. As possible solution to this problem, St-Onge et al. (2004) proposed a normalization of photogrammetric tree height measurements with an ALS-based DTM. Moreover, St-Onge et al. (2008) compared CHMs derived from DAP (normalized with an ALS-based DTM) to purely ALS-based CHMs. The authors concluded that height metrics derived from both types of CHMs were generally highly correlated.

More recent studies have compared the capability of using canopy height data obtained from DAP in conjunction with an ALS-based DTM to the use of purely ALS-based height data for the area-based estimation of forest inventory attributes. Most of these studies were carried out in conifer-dominated boreal forests, e.g. in Finland (Nurminen et al. 2013, Vastaranta et al. 2013), in Norway (Rahlf et al. 2014, Gobakken et al. 2015), and in northeastern Ontario, Canada (Pitt et al. 2014). Generally, the aforementioned studies have confirmed the applicability of image-based height measurements as an alternative to ALS data for the prediction of forest attributes such as mean height, mean diameter, total volume, total biomass or basal area, although root-mean-squared errors (*RMSEs*) were frequently slightly higher for DAP. Additionally, as stated e.g. by Vastaranta et al. (2013), DAP lacks the penetration into the sub-canopy, and thus is disadvantageous to ALS when characterizing the vegetation density.

Similarly, White et al. (2015) investigated the modelling performance of both DAP and ALS for a complex coastal temperate rainforest on Vancouver Island, Canada; and Straub et al. (2013) compared DAP and ALS in a mixed central European test site dominated by double and multi-layered stands in southeastern Bavaria, Germany. Both studies affirmed the general finding that DAP is a suitable alternative for modelling forest inventory attributes, but the *RMSEs* reported for both ALS and DAP exceeded those obtained in the boreal test sites previously mentioned, though to a minor extend. Several factors might have influenced the modelling performances in the above-mentioned studies: the aerial camera systems, the photogrammetric software packages used for image matching, the size of the field plots, the modelling approaches, and the validation techniques used. Nevertheless, we assume that the differences in *RMSEs* observed for the aforementioned studies can be largely attributed to the different forest types and structures in the different test sites. As described by Næsset (2002b), the forest structure might even influence the performance of the image matching itself. He speculated that matching performs better for dense, even-aged broadleaved stands with rounded crowns compared with more heterogeneous coniferous stands with peaked crowns.

Thus, the present study was designed to explicitly evaluate the potential impact of the prevailing forest type on the modelling of forest attributes in central European forests. For this objective, we adopted a workflow developed in previously published work (Straub et al. 2013, Stepper et al. 2015). In the work presented here, this workflow is verified under practical conditions in both a beech- and a spruce-dominated test site, which represent common broadleaf- and conifer-dominated forest environments in Germany (Thünen-Institut 2015). As the above-mentioned studies conducted in central European forests have focussed on the prediction of basal area and timber volume, there is still a need to test how accurately other attributes can be estimated. Thus, we evaluated models for a set of five different forest inventory attributes – stem density, basal area, quadratic mean diameter, volume, and Lorey's mean height.

2 Materials

2.1 *Test Sites*

For this study, we selected two test sites (Spessart 49° 57' N, 9° 24' E and Frankenwald, 50° 21' N, 11° 27' E) in the northern part of Bavaria, Germany, because the relative stocking of the species, present in each of the two test sites, represent common forest types in Germany, i.e., the beech and the spruce types (which cover 16.6% and 29.3% of the total forest area in Germany, respectively; Thünen-Institut 2015). Tab. 1 summarizes the total size, the extent of the state forests, the topography, and the main tree species proportions at each site. In the Spessart area, European beech (*Fagus sylvatica* L.) is the dominant tree species on mesic sites, while dryer sites contain a higher proportion of sessile oak (*Quercus petraea* (Mattuschka) Liebl.). In the Frankenwald test site, the forests are mainly dominated by Norway spruce (*Picea abies* (L.) H. Karst).

2.2 *Forest Inventory Data*

Field measurements from regularly conducted forest management inventories of the BaySF served as training data for the modelling. Neufanger (2011) provides a concise outline of how forest management inventories in the state forests of Bavaria are planned and conducted. These inventories make use of three concentric sampling circles, as described in detail in Straub et al. (2013) and Stepper et al. (2015). A general introduction to the use of concentric sample plots for forest inventories can be found in Van Laar & Akça (2007).

Tab. 1: Summary of the topography and main tree species at the Spessart and Frankenwald test sites; tree species proportions were calculated based on the respective basal areas at the forest inventory plots.

Test site	Spessart	Frankenwald
Total size (ha)	20824	15139
State forest area (ha)	8440	3821
Elevation range (m a.s.l.)	230 – 587	367 – 723
Elevation average (m a.s.l.)	418	580
Forest type	beech-dominated	spruce-dominated
Tree species:		
Norway spruce (%)	9	78
Scots pine (%)	1	0
other conifers (%)	8	4
European beech (%)	56	14
Sessile oak (%)	24	0
other broadleaves (%)	2	4

Here, the trees are recorded in dependency of their diameter at breast height (measured 1.3 m above ground) and their distance to the plot centre. Whilst in the innermost circle with a radius of 2.82 m (25 m²) all trees are measured, the minimum diameter for inclusion is 30 cm in the largest circle with a radius of 12.62 m (500 m²). This 500 m² circle represents the reference area for the analysis of the remote sensing data in this study.

Permanent field plots were distributed systematically across the state forests in both test sites based on a regular 200 m × 200 m grid. In the Spessart test site, the terrestrial measurements used in this analysis were carried out from May to September 2011; while in the Frankenwald test site, sampling took place between April and September 2014. The plot centres were located using a Trimble GeoExplorer XT GPS device (maximum deviations of ±3–5 m; H. Grünvogel, personal communication, 4 August 2014). Within each circular plot, several characteristics such as species, diameter at breast height d, and tree height h were recorded for individual trees. For our examination, we considered only trees with $d \geq 7$ cm, i.e., those trees that exceed the threshold for merchantable timber. Due to the concentric sampling method used, a different weight w_i is applied to each measured value for each tree when computing per-hectare inventory attributes, which is related to the size of the concentric circle with radius r (m) in which the tree was measured: $w_i = 10000/(\pi r^2)$.

The following attributes were computed for each of the field plots (where m is the number of trees measured at the respective plot):

- Stem density N: Number of trees per hectare;

$$N\,(\text{trees ha}^{-1}) = \sum_{i=1}^{m} w_i \tag{1}$$

- Basal area G per hectare: Sum of the basal areas g_i, i.e., cross-sectional areas measured at 1.3 m above ground, of the trees measured multiplied by their respective weights;

$$G\left(\text{m}^2\text{ha}^{-1}\right) = \sum_{i=1}^{m} g_i w_i \tag{2}$$

- Quadratic mean diameter QMD;

$$QMD\,(\text{cm}) = \sqrt{\frac{\sum_{i=1}^{m} d_i^2 w_i}{\sum_{i=1}^{m} w_i}} \tag{3}$$

- Volume V per hectare: Sum of the single tree stem volumes v_i multiplied by their respective weights;

$$V\,(\text{m}^3\text{ha}^{-1}) = \sum_{i=1}^{m} v_i w_i \tag{4}$$

- Lorey's mean height H_L: Weighted mean height, where each single tree height h_i is weighted by the basal area g_i, multiplied by its respective weight;

$$H_L\left(\text{m}\right) = \frac{\sum_{i=1}^{m} h_i g_i w_i}{\sum_{i=1}^{m} g_i w_i} \tag{5}$$

This set of forest inventory attributes was computed for a total of 2010 field plots in the Spessart test site and 801 plots in the Frankenwald test site. Tab. 2 lists descriptive statistics for each of these attributes for the two test sites. In addition, statistics of the mean age, as derived from overstorey trees, i.e., those trees forming the upper canopy layer, are shown in Tab. 2.

2.3 *Remote Sensing Data*

All remote sensing data used in this study were acquired as a part of regular programs conducted by the Bavarian Administration for Surveying. Currently, aerial photographs are updated every three years in Bavaria. The general specifications for these official aerial photographs are provided in LDBV (2015b). An UltraCamXp camera was used in both test sites to acquire the stereo photography used in this analysis. The aerial survey covering the Spessart test site was conducted on 6 August 2011, while the aerial photographs for the Frankenwald test site were acquired in two separate flights – on 21 May and 8 June 2014. The forward and side overlaps of the images were 75% and 25% for the Spessart area and 75% and 40% for the Frankenwald area, resulting in a total of 122 and 210 stereo

Tab. 2: Descriptive statistics for the forest inventory attributes (stem density *N*, basal area *G*, quadratic mean diameter *QMD*, volume *V*, and Lorey's mean height H_L) derived from field plot observations (*n* = number of field plots with trees exceeding the minimum threshold $d \geq 7$ cm). In addition, statistics of the mean age of overstorey trees are shown.

	Forest attribute	Min.	1st quartile	Median	3rd quartile	Max.	Mean	SD
Spessart beech-dominated (n = 2010)	*N* (trees ha^{-1})	19	182	385	906	4313	687	759
	G (m^2 ha^{-1})	1	20	27	35	91	28	11
	QMD (cm)	8	20	31	42	94	32	15
	V (m^3 ha^{-1})	2	196	288	393	1228	304	158
	H_L (m)	4	22	28	32	45	27	7
	Age (years)	12	52	106	150	378	108	59
Franken-wald spruce-dominated (n = 801)	*N* (trees ha^{-1})	20	225	404	765	2997	587	550
	G (m^2 ha^{-1})	2	18	30	39	86	29	15
	QMD (cm)	8	21	31	40	68	31	12
	V (m^3 ha^{-1})	1	147	296	409	846	288	174
	H_L (m)	3	21	27	30	41	24	8
	Age (years)	8	49	63	81	157	65	26

images, respectively. We used the panchromatic (PAN) images, with 12 bit radiometric resolution and a ground sampling distance of 0.20 m. The interior and exterior orientation parameters were provided by the vendor.

Moreover, we used the most recent ALS-based terrain models available – 1 m spatial resolution DTMs derived from topographic mapping surveys conducted by the Bavarian Administration for Surveying. These surveys were carried out in 2007 (last return point density: 2.83 m^{-2}) in the Spessart area and in 2009 (1.81 m^{-2}) in the Frankenwald area.

3 Methods

The main processing steps of our analysis described in the section that follows are:

- Computation of canopy height models (CHMs)
- Calculation of predictor variables based on the CHMs calculated in step one.
- Area-based modelling of forest inventory attributes using random forest with built-in recursive feature elimination.

3.1 *Computation of Canopy Height Models*

For dense image matching of the PAN-images, we used the SGM approach, as implemented in the Remote Sensing Software Package Graz (RSG, v. 7.46; Joanneum Research 2014). Within SGM, the dissimilarity between corresponding pixels in two epipolar images – the base and match image – is measured by matching costs, i.e., the aggregation of the costs calculated along each 45° 1D search path from the respective base image pixel (Hirschmüller 2008). For each base image pixel, the disparity that corresponds to the minimum aggregated costs is selected, and a disparity map for the stereo pair is computed. In RSG, disparities are computed twice for each stereo pair, by switching the role of base and match image. Using a threshold for maximum disparity differences, consistency of the matching can be checked and mismatches can be eliminated (Gehrke et al. 2010). According to the recommendations of the software developers of RSG with regard to the imagery available, we set the parameters for both test sites as follows: the maximum back-matching threshold was defined as 1.5 pixels, the number of image pyramid levels was set to 4, and

the matching step-size at the final pyramid level was set to 1 pixel. All stereo pairs from the along-track overlap (min. 60%) were used; across-track stereo pairs were not considered due to the small area of across-track overlap between the aerial images acquired. Based on the resulting point clouds, DSMs (1 m spatial resolution) were derived using the point triangulation method as implemented in the las2dem tool from LAStools (v. 141218; Rapidlasso GmbH 2015). Finally, to derive canopy heights above ground, the surface heights were normalized by subtracting the height values from the existing ALS-based DTMs described above from the heights of the DSMs.

3.2 *Calculation of Predictor Variables based on the CHMs*

To derive predictor variables from the CHMs, we developed a routine based on the machine vision software HALCON (v. 12.0.1; MVTec Software GmbH 2015). Following the recommendations of White et al. (2013b) for ALS data, we calculated the following 14 predictors related to forest height, canopy cover and variability in height for each 500 m² inventory plot region:

- Six height metrics: minimum h_{min}, first quartile h_{25}, mean h_m, median h_{50}, third quartile h_{75}, and maximum h_{max}.
- Six canopy cover (*cc*) metrics as indicators for vegetation density: cc_0, cc_1, … , cc_6. Crown regions *cr* were extracted based on six different height thresholds (2 m, 5 m, 10 m, 15 m, 20 m, and 25 m) and related to the total plot area: $cc\ (\%) = area(cr)/area(plot) \times 100$.
- Two canopy height variability metrics: standard deviation h_{sd} and coefficient of variation h_{cv}.

3.3 *Area based Forest Attribute Modelling*

We used the open-source statistical software R (v. 3.2.2; R Core Team 2015) for the development of the modelling procedure. The prediction models were implemented using the R packages *randomForest* (Liaw & Wiener 2002) and *caret* (Kuhn 2015). Random forest was used as modelling approach, since it was successfully applied in several other studies dealing with the estimation of forest attributes using remotely sensed data (e.g. Pitt et al. 2014, White et al. 2015, Immitzer et al. 2016). The main characteristics of random forest, as developed by Breiman (2001), are:

- Multiple base learners – the decision trees – are trained based on bootstrap-sampled versions of the training data. Generating bootstraps, i.e., random subsets of the entire set of training data, introduces a first random component in the tree-building process (Kuhn & Johnson 2013). To obtain the prediction for new samples, the predictions of the individual decision trees are averaged.
- During the decision tree construction process, at each split, a random subset of predictor variables to choose from is selected. This second term of randomness helps decorrelate the individual decision trees, thus improving the overall performance of the estimator (Hastie et al. 2009).

As suggested by Kuhn & Johnson (2013), we set the parameter $n_{tree} = 1000$, i.e., an ensemble of 1000 trees was used to build the respective forests. The number of variables randomly selected at each split was set to one-third of the number of available predictors ($m_{try} = p/3$), as recommended by Breiman (2001). Besides the coefficient of determination (R^2), we computed the root-mean-squared error (*RMSE*) and the *bias* as quantitative measures for model performance. In order to achieve reliable estimates for these measures, we applied a 10-fold cross-validation repeated five times (Kuhn & Johnson 2013). Thus, 50 different held-out sets (from here on referred to as folds, *f*) were used to assess the model outcomes for each of the five forest inventory attributes at each of the two test sites. For each fold, we computed the $RMSE_f$ and $bias_f$, (6) and (7). As per Stepper et al. (2015), these $RMSE_f$ and $bias_f$ values were averaged over the 50 folds to generate overall measures for *RMSE* and *bias*, (8) and (9). In the same way, overall R^2 measures were derived as the average of the R^2_f values from the 50 folds (10), where each R^2_f value corresponded to the squared Pearson's correlation coefficient between the preditcted and observed values in the respective fold *f*.

$$RMSE_f = \sqrt{\frac{\sum_{i=1}^{n}\left(y_i - \hat{y}_i\right)^2}{n}} \quad (6)$$

$$bias_f = \frac{\sum_{i=1}^{n}(y_i - \hat{y}_i)}{n} \quad (7)$$

$$RMSE = \frac{\sum_{j=1}^{k} RMSE_{f,j}}{k} \quad (8)$$

$$bias = \frac{\sum_{j=1}^{k} bias_{f,j}}{k} \quad (9)$$

$$R^2 = \frac{\sum_{j=1}^{k} R^2_{f,j}}{k} \quad (10)$$

In (6) to (10), y_i refers to the observed value, $\hat{y}_i$ is the predicted value of the i^{th} of n sampled observations in one of the k folds f.

Predictors derived from image-based CHMs can be highly prone to multi-collinearity (White et al. 2015). Despite the ability of random forest to handle high-dimensional and highly correlated predictor datasets, Immitzer et al. (2016) demonstrated that an additional step implementing feature selection resulted in improved model performance when estimating timber volume based on WorldView-2 stereo satellite data. Accordingly, we applied recursive feature elimination (RFE) as implemented in the *caret* package. This search algorithm utilizes the feature importance of random forest – as computed for the full model including all 14 predictors – to sequentially remove each predictor based on its importance. For each new predictor subset created by removing the next sequential predictor, new models are trained and the respective *RMSEs* are stored. Finally, the best performing subset is determined by the lowest *RMSE*. Comprehensive explanations regarding RFE and its implementation in *caret* are provided in Kuhn & Johnson (2013) and Kuhn (2015).

4 Results

For each of the forest inventory attributes considered here (*N, G, QMD, V,* and H_L), we generated individual random forest models separately for each of the two test sites – Spessart and Frankenwald. The RFE implemented in the *caret* package selected different numbers of predictors for the individual random forest models ranging from 5 to 14. For eight of the developed models the RFE selected a combination of height, canopy cover and canopy height variability metrics. For all models, a height metric achieved the highest importance score. In both test sites, h_{50} was ranked as the most important predictor for *V*. Moreover, h_{max} was ranked as the most influential predictor for *N*, *QMD* and H_L in both sites.

The cross-validated estimates for R^2, *RMSE* and *bias* are summarized in Tab. 3. As is common practice, the absolute *RMSE* and *bias* values were 'normalized' by dividing by the mean of the observations, hereafter referred to as $RMSE_{mean}$ (%) and $bias_{mean}$ (%). Moreover, we used the median for 'normalization' (see Tab. 2), referred to as $RMSE_{median}$ (%) and $bias_{median}$ (%).

Overall, the R^2 values of the models for the different forest attributes in both test sites varied in the range from 0.26 to 0.84. For the attributes *G, QMD, V,* and H_L, higher R^2 values were obtained for the spruce-dominated Frankenwald, whereas for *N* the model for the beech-dominated Spessart resulted in a higher R^2. As expected, highest R^2 values were achieved for H_L in both test sites. The *G* model developed for the beech-dominated forest yielded the lowest R^2.

For all models, the resulting *RMSEs* were consistently smaller than the corresponding standard deviations of the observations (Tab. 2). For H_L, the $RMSE_{mean}$ (%) values for the spruce- and the beech-dominated test sites were identical, and the $RMSE_{median}$ (%) values were very close. Furthermore, with respect to the $RMSE_{mean}$ (%), the predictions were similar for *N* and *G* in the two test sites. For *V* and *QMD*, lower *RMSEs* were obtained for the spruce-dominated forest, with more evident differences for the *QMD*.

Within the test sites, both options for normalization (i.e., $RMSE_{mean}$ (%) and $RMSE_{median}$ (%)) resulted in similar relative *RMSEs* for the attributes *G, QMD, V* and H_L, whereas major differences occurred for *N*. Due to the heavily right-skewed distributions of the observed

field data for *N* (see Tab. 2), using the median for normalization resulted in much higher numbers compared to the normalization by the mean.

Bias was small for all random forest models generated. Minor systematic overpredictions were only observed for the models describing stem density *N*.

The scatter of predicted vs. observed values for all attributes is shown by hexagonal binning plots in Fig. 1. Additionally, the distributions of model residuals, i.e., differences of observed minus predicted values, were computed for distinct age classes which are commonly used in forest management practice in Germany (I = 1–20 years, II = 21–40, III = 41–60, … , X = 181–200; Kramer & Akça 2008). The residual distributions are displayed in Fig. 2 and the following main observations can be made:

- For *N*, a large scatter of residuals is visible for the younger age classes (especially for the classes I to III), which is similar for both test sites. Nonetheless, the medians are close to zero.
- For *G* and *V*, the boxplots indicate a slight overprediction for the youngest age class I, whereas the models tended to underpredict in the oldest class, i.e., >X for Spessart and >VI for Frankenwald.
- For *QMD*, the distribution of the residuals widens with increasing age in both test sites. Moreover, the models obviously overpredicted *QMDs* at inventory plots with age class I. Furthermore, the *QMD* model for the Spessart test site showed a tendency to underpredict *QMDs* in older age classes (especially in the classes IX, X and >X).
- For H_L, the models overpredicted the observed values in age class I in both test sites. In addition, the boxplots for the Spessart test site indicate that H_L was obviously underpredicted in the oldest age class >X.

5 Discussion

The R^2 values for *G, QMD, V* and H_L achieved for the spruce-dominated Frankenwald revealed a better model fit (R^2: 0.54, 0.61, 0.70, 0.84) compared to those for the beech-dominated Spessart (R^2: 0.26, 0.52, 0.47, 0.79). Moreover, with respect to the $RMSE_{mean}$ (%) values, a slightly higher level of accuracy was observed for the prediction of *QMD* for the spruce-dominated forest type. According to Niklas (1994) and Pretzsch et al. (2013) this observation might be partially attributed to the allometric difference in the height-diameter-relationships of conifers and broad-leaved tree species. Moreover, it has to be

Tab. 3: Cross-validated measures of model performance (R^2, *RMSE*, *bias*) of the random forest models for stem density *N*, basal area *G*, quadratic mean diameter *QMD*, volume *V*, and Lorey's mean height H_L, calculated separately for the two test sites/forest types Spessart and Frankenwald; the absolute *RMSE* and *bias* values were 'normalized' with the mean and the median of the observations.

	Forest attribute	R^2	*RMSE*	$RMSE_{mean}$ (%)	$RMSE_{median}$ (%)	*bias*	$bias_{mean}$ (%)	$bias_{median}$ (%)
Spessart, beech-dominated (n = 2010)	N (trees ha^{-1})	0.60	483	70.3	125.4	-4	-0.6	-1.1
	G (m^2 ha^{-1})	0.26	9.9	36.0	36.7	-0.1	-0.2	-0.2
	QMD (cm)	0.52	10.4	32.3	33.7	-0.2	-0.5	-0.5
	V (m^3 ha^{-1})	0.47	114.9	37.8	39.9	-0.9	-0.3	-0.3
	H_L (m)	0.79	3.3	12.4	11.9	0.0	-0.1	-0.1
Frankenwald, spruce-dominated (n = 801)	N (trees ha^{-1})	0.37	440	74.9	108.8	-8	-1.3	-1.9
	G (m^2 ha^{-1})	0.54	10.3	35.2	34.4	0.0	0.0	0.0
	QMD (cm)	0.61	7.6	24.9	24.3	0.0	-0.1	-0.1
	V (m^3 ha^{-1})	0.70	96.1	33.3	32.5	-0.3	-0.1	-0.1
	H_L (m)	0.84	3.0	12.4	11.3	0.0	0.1	0.1

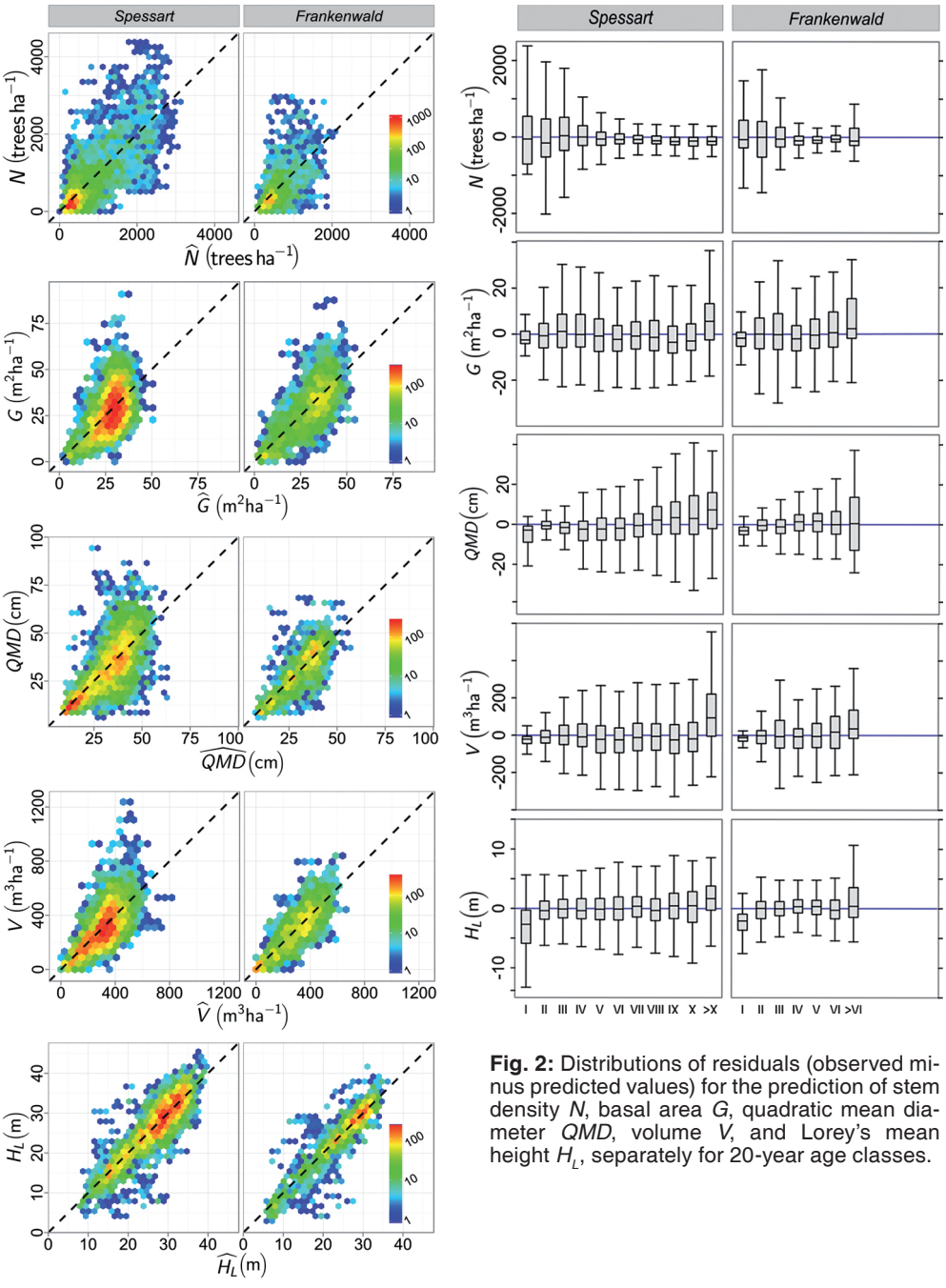

Fig. 2: Distributions of residuals (observed minus predicted values) for the prediction of stem density *N*, basal area *G*, quadratic mean diameter *QMD*, volume *V*, and Lorey's mean height H_L, separately for 20-year age classes.

Fig. 1: Predicted (x-axis) vs. observed (y-axis) values for stem density *N*, basal area *G*, quadratic mean diameter *QMD*, volume *V*, and Lorey's mean height H_L, shown as hexagonal binning plots (xy-plane tessellated by a regular grid of hexagons; hexagons are coloured according to the number of points falling into each hexagon; Lewin-Koh 2011).

considered that the CHMs from DAP mainly characterize the overstorey and do not include information about the understorey structure, which is not visible in the aerial photographs. Thus, it must be expected that reference trees growing in the understorey add some additional scatter to predictive models. We assume that this influence can vary for spruce- and beech-dominated forests, due to differences in stand structures. For assessing the understorey, ALS technology is advantageous as it penetrates through small gaps in the canopy and may provide additional returns from underlying vegetation layers (White et al. 2013a).

The plot-level $RMSE_{mean}$ (%) values obtained for *V* and *G* in the present study were similar to those values reported by Straub et al. (2013) for a mixed managed forest in southern Bavaria (37.9% for *V* and 35.3% for *G*). Frequently, better accuracies were reported for managed conifer-dominated boreal test sites which are most probably due to more homogeneous forest structures in contrast to the more diverse central European forest conditions. As an example, Nurminen et al. (2013) applied random forest for a test site in Finland and achieved normalized *RMSEs* of 6.8% for mean height, 12.0% for mean diameter and 22.6% for volume based on UltraCamD images with a forward overlap of 80%. Moreover, Vastaranta et al. (2013), who applied random forest within a nearest neighbour search for a test site in Finland, reported *RMSEs* of 11.2% for mean height, 21.7% for mean diameter, 23.6% for basal area, and 24.5% for volume when using UltraCamXp data with a forward overlap of 70%.

As in the study of Woods et al. (2011), who used ALS data for an operational forest inventory in boreal Ontario, we obtained poorest model accuracies, i.e., largest *RMSEs*, for *N* in comparison to the other tested attributes. As mentioned above, trees in the understorey cannot be captured by DAP. Most likely, this fact contributed to the large *RMSEs* for *N*. Moreover, it was shown for *N*, with a heavily skewed distribution of the observed values that the two variants for normalizing the absolute *RMSEs* resulted in very different values in the two test sites. Thus, for this type of data, we suggest that the *RMSEs* normalized by the median give a more robust estimate of the relative *RMSE*.

For several attributes, e.g. for *G* and *V* in both test sites, the models overpredicted the ground measured values at inventory plots from the youngest age class, and vice-versa underpredicted in the oldest age classes. This may be partly explained by the fact that random forest tends to overpredict low values and to underpredict high ones which was stated in several publications, e.g. Baccini et al. (2004), Vanselow & Samimi (2014), or Immitzer et al. (2016). This is also reflected by the scatterplots shown in Fig. 1. Moreover, the underpredictions in the oldest age classes seem plausible, since the functional relationship between canopy height and the actual stocking (*G* or *V*) will be weaker for older forest stands with a decreasing vertical growth. Additionally, as we observed for our data, the distribution of residuals is related to the variability of the observations within the respective age classes. For example, for both test sites, a larger scattering of residuals was revealed for *N* in the young age classes, which is associated with the expected larger variability and range of stem densities for these classes compared to the lower variabilities in older classes.

We applied random forest regression within R and our results confirmed the suitability of this modelling approach. In previous studies, Penner et al. (2013) and Stepper et al. (2015) showed that random forest produced accuracies comparable to parametric models. Random forest has several advantages for operational applications, e.g.: a priori assumptions about the relationship between response and predictor variables are not required, multicollinearity among predictors can be handled, and large numbers of predictors can be considered without overfitting (Pitt et al. 2014, Immitzer et al. 2016). Still, disadvantages of the random forest regression, that are frequently considered, are the 'black-box' nature of the algorithm (White et al. 2013b) as well as the inability – common to all non-parametric approaches – to extrapolate beyond the range of the training data (Stepper et al. 2015). Thus, in order to train prediction models that are valid for the entire population, samples that cover the complete range of existing values are necessary. Since many sample plots were distributed on a dense grid in both test sites of this study, we assume that a good coverage is

guaranteed. Besides the representativeness of the sample, the size and the georeferencing accuracy of the field plots will have an influence on the predictive power of the models (White et al. 2013b). Thus, we attribute a part of the shown scatter between observed and predicted values to the reported 3 m – 5 m GPS offsets of the plot positions. As described in section 2.2, each field plot consists of three concentric sampling circles. This plot design is commonly used for the forest management inventories in the state forests of Bavaria as well as in other federal states in Germany. According to Lawrence et al. (2010), the fundamental advantage of concentric circles is that the more frequent small trees are measured within small circles and the less frequent large trees are measured in large circles. This practice reduces the overall costs of the field survey with just little loss in precision. However, the use of concentric circles as training data might have some impact on the area-based modelling, if the sample for the small trees is not representative for the largest circle which is commonly used as the reference area to extract remote sensing features.

As mentioned in the introduction, ALS was already integrated successfully into operational forest management inventories in some countries using the area-based approach. In principle, area-based predictions enable the production of wall-to-wall maps displaying the estimated spatial distribution of forest inventory attributes at a spatial resolution which relates to the size of the field plots used to train the model (White et al. 2013b), i.e., 500 m^2 for our data. Using height information generated from dense image matching for the spatial prediction of forest attributes is the subject of ongoing research. Recently, we conducted a first pilot study together with forest inventory experts of the BaySF to assess the benefit of CHMs from DAP and derived wall-to-wall timber volume maps to support forest management tasks. The inventory experts determined several applications for these remote sensing products as a supplement to the existing terrestrial data. For example, CHMs were found to be useful to support and validate the manual delineation of management units, i.e., forest stand regions. Moreover, the inventory experts saw potential to derive aggregated volume estimates for stand regions based on the wall-to-wall timber volume maps, which currently cannot be deduced from the field data. This information might be useful to determine the harvest volume more exactly. In future, additional studies and investigations have to be conducted together with the end-users to further evaluate the potential and the limitations of DAP for practical forestry applications.

6 Conclusion

Following other studies, which have used DAP to model forest inventory attributes, we investigated the prediction of mean and total plot-level attributes. These predictions were compared for a beech- and a spruce-dominated central European test site. With respect to relative *RMSEs*, i.e., divided by the observation means, most distinct differences were observed for the prediction of *QMD* with a slightly better accuracy for the spruce-dominated forest, whereas similar outcomes were obtained for the other tested attributes. To better understand the influence of tree species on model performances, future research may focus on the assessment of species-specific models, e.g., to predict the plot-level volume of the main species for a selected test region using both height and spectral information from the aerial photographs.

We conclude that the proposed workflow can provide predictions for forest areas where terrestrial inventory data are available to train predictive models, such as the state forests of Bavaria. Conversely, for many small-parcelled private forest properties in Bavaria, no such terrestrial inventories are conducted. To additionally provide information for the forest management in these estates, further research might investigate the transferability of prediction models generated in state forests to other forest areas.

Acknowledgements

The authors are grateful to the Bavarian State Forest Enterprise (BaySF) for supplying the inventory data and to the Bavarian Admin-

istration for Surveying for providing the remote sensing data used in this research. We also thank Prof. Dr. Mathias Schardt and Dr. Karlheinz Gutjahr from JOANNEUM RESEARCH for assistance with and permission to use the RSG software, Laura Carlson for language editing and Rudolf Seitz for helpful comments on earlier drafts of this paper. We owe special thanks to the reviewers for thorough and excellent reviews which improved the manuscript. Funding of this research was granted by the Bavarian State Ministry of Food, Agriculture and Forestry.

References

Adler, P. & Koch, B., 1999: Digital photogrammetry for forest ecosystem monitoring. – Conference Proceedings 'Remote Sensing and Forest Monitoring', Rogów, Poland.

Baccini, A., Friedl, M.A., Woodcock, C.E. & Warbington, R., 2004: Forest biomass estimation over regional scales using multisource data. – Geophysical Research Letters **31**: L10501.

BaySF, 2015: Statistikband 2015, Bayerische Staatsforsten. – http://www.baysf.de/de/publikationen.html (7.3.2016).

Breiman, L., 2001: Random forests. – Machine learning **45** (1): 5–32.

Gehrke, S., Morin, K., Downey, M., Boehrer, N. & Fuchs, T., 2010: Semi-global matching: An alternative to LIDAR for DSM generation? – The International Archives of the Photogrammetry, Remote Sensing and Spatial Information Sciences **XXXVIII**, Part 1.

Ginzler, C. & Hobi, M., 2015: Countrywide stereo-image matching for updating digital surface models in the framework of the Swiss National Forest Inventory. – Remote Sensing **7** (4): 4343–4370.

Gobakken, T., Bollandsås, O.M. & Næsset, E., 2015: Comparing biophysical forest characteristics estimated from photogrammetric matching of aerial images and airborne laser scanning data. – Scandinavian Journal of Forest Research **30** (1): 73–86.

Haala, N. & Rothermel, M., 2012: Dense Multi-Stereo Matching for High Quality Digital Elevation Models. – PFG – Photogrammetrie, Fernerkundung, Geoinformation **2012** (4): 331–343.

Hastie, T., Tibshirani, R. & Friedman, J.H., 2009: The elements of statistical learning. – Second edition, Springer, New York, NY, USA.

Hirschmüller, H., 2008: Stereo processing by semiglobal matching and mutual information. – IEEE Transactions on Pattern Analysis and Machine Intelligence **30** (2): 328–341.

Immitzer, M., Stepper, C., Böck, S., Straub, C. & Atzberger, C., 2016: Use of WorldView-2 stereo imagery and National Forest Inventory data for wall-to-wall mapping of growing stock. – Forest Ecology and Management **359**: 232–246.

Joanneum Research, 2014: Remote Sensing Software Package Graz. – http://www.remotesensing.at/en/remote-sensing-software.html (7.3.2016).

Kätsch, C. & Stöcker, M., 2000: Untersuchungen zur automatischen Ermittlung von Bestandeshöhen auf Luftbildern mit Hilfe der Digitalen Photogrammetrie. – Allgemeine Forst- und Jagdzeitung **171**: 74–80.

Korpela, I. & Anttila, P., 2004: Appraisal of the mean height of trees by means of image matching of digitised aerial photographs. – The Photogrammetric Journal of Finland **19** (1): 23–36.

Kramer, H. & Akça, A., 2008: Leitfaden zur Waldmesslehre. – J.D. Sauerländer's Verlag, Frankfurt am Main.

Kuhn, M. & Johnson, K., 2013: Applied Predictive Modeling. – Springer, New York, NY, USA.

Kuhn, M., 2015: Package 'caret'. – https://cran.r-project.org/web/packages/caret/caret.pdf (7.3.2016).

Lawrence, M., McRoberts, R.E., Tomppo, E., Gschwantner, T. & Gabler, K., 2010: Comparisons of National Forest Inventories. – Tomppo, E., Gschwantner T., Lawrence, M. & McRoberts, R.E. (eds.): National Forest Inventories. – Springer, 19–32.

LDBV, 2015a: Digitale Geländemodelle (DGM). Product information leaflet. – http://vermessung.bayern.de/file/pdf/1614/download_faltblatt-dgm09.pdf (7.3.2016).

LDBV, 2015b: Luftbildprodukte. Product information leaflet. – http://vermessung.bayern.de/file/pdf/1039/download_faltblatt-luftbilder08.pdf (7.3.2016).

Lewin-Koh, N., 2011: Hexagon Binning: an Overview. – https://cran.r-project.org/web/packages/hexbin/vignettes/hexagon_binning.pdf. (7.3.2016).

Liaw, A. & Wiener, M., 2002: Classification and Regression by randomForest. – R news **2** (3): 18–22.

Maltamo, M. & Packalen, P., 2014: Species-specific management inventory in Finland. – Maltamo, M., Næsset, E. & Vauhkonen, J. (eds.): Forestry Applications of Airborne Laser Scanning. – Springer, 241–252, Dordrecht, Netherlands.

Means, J.E., Acker, S.A., Fitt, B.J., Renslow, M., Emerson, L. & Hendrix, C.J., 2000: Predicting

forest stand characteristics with airborne scanning LiDAR. – Photogrammetric Engineering & Remote Sensing **66** (11): 1367–1371.

MVTec Software GmbH 2015: HALCON. – http://www.halcon.com/ (7.3.2016).

Næsset, E., 2002a: Predicting forest stand characteristics with airborne scanning laser using a practical two-stage procedure and field data. – Remote Sensing of Environment **80** (1): 88–99.

Næsset, E., 2002b: Determination of mean tree height of forest stands by digital photogrammetry. – Scandinavian Journal of Forest Research **17** (5): 446–459.

Næsset, E., 2014: Area-based inventory in Norway – from innovation to an operational reality. – Maltamo, M., Næsset, E. & Vauhkonen, J. (eds.): Forestry Applications of Airborne Laser Scanning. – Springer, 215–240, Dordrecht, Netherlands.

Neufanger, M., 2011: Richtlinie für die mittel- und langfristige Forstbetriebsplanung in den Bayerischen Staatsforsten. – Forsteinrichtungsrichtlinie – FER 2011.

Niklas, K.J., 1994: Plant allometry. – University of Chicago Press, Chicago, IL, USA.

Nurminen, K., Karjalainen, M., Yu, X., Hyyppä, J. & Honkavaara, E., 2013: Performance of dense digital surface models based on image matching in the estimation of plot-level forest variables. – ISPRS Journal of Photogrammetry and Remote Sensing **83**: 104–115.

Packalen, P. & Maltamo, M., 2007: The k-MSN method in the prediction of species specific stand attributes using airborne laser scanning and aerial photographs. – Remote Sensing of Environment **109** (3):328–341.

Penner, M., Pitt, D.G. & Woods, M.E., 2013: Parametric vs. nonparametric LiDAR models for operational forest inventory in boreal Ontario. – Canadian Journal of Remote Sensing **39** (5): 426–443.

Pitt, D.G., Woods, M. & Penner, M., 2014: A Comparison of point clouds derived from stereo imagery and airborne laser scanning for the area-based estimation of forest inventory attributes in boreal Ontario. – Canadian Journal of Remote Sensing **40** (3): 214–232.

Pretzsch, H., Dauber, E. & Biber, P., 2013: Species-specific and ontogeny-related stem allometry of European forest trees: evidence from extensive stem analyses. – Forest Science **59** (3): 290–302.

R Core Team, 2015: The R project for statistical computing. – https://www.r-project.org/(7.3.2016).

Rahlf, J., Breidenbach, J., Solberg, S., Næsset, E. & Astrup, R., 2014: Comparison of four types of 3D data for timber volume estimation. – Remote Sensing of Environment **155**: 325–333.

Rapidlasso GmbH 2015: LAStools. – http://rapidlasso.com/lastools/ (7.3.2016).

Stepper, C., Straub, C. & Pretzsch, H., 2015: Using semi-global matching point clouds to estimate growing stock at the plot and stand levels: application for a broadleaf-dominated forest in central Europe. – Canadian Journal of Forest Research **45** (1): 111–123.

St-Onge, B., Jumelet, J., Cobello, M. & Vega, C., 2004: Measuring individual tree height using a combination of stereophotogrammetry and lidar. – Canadian Journal of Forest Research **34** (10): 2122–2130.

St-Onge, B., Vega, C., Fournier, R.A. & Hu, Y., 2008: Mapping canopy height using a combination of digital stereo-photogrammetry and lidar. – International Journal of Remote Sensing **29** (11): 3343–3364.

Straub, C., Stepper, C., Seitz, R. & Waser, L.T., 2013: Potential of UltraCamX stereo images for estimating timber volume and basal area at the plot level in mixed European forests. – Canadian Journal of Forest Research **43** (8): 731–741.

Straub, C. & Seitz, R., 2014: Verwendungspotential von Fernerkundungsdaten in der Forsteinrichtung. – Vortrag bei der Tagung der Arbeitsgemeinschaft Forsteinrichtung am 22.10.2014 in Weimar.

Thünen-Institut, 2015: Dritte Bundeswaldinventur (2012). – https://bwi.info. (7.3.2016).

Van Laar, A. & Akça, A., 2007: Forest Mensuration. – Springer, Dordrecht, Netherlands.

Vanselow, K.A. & Samimi, C., 2014: Predictive mapping of dwarf shrub vegetation in an arid high mountain ecosystem using remote sensing and Random Forests. – Remote Sensing 6: 6709–6726.

Vastaranta, M., Wulder, M.A., White, J.C., Pekkarinen, A., Tuominen, S., Ginzler, C., Kankare, V., Holopainen, M., Hyyppä, J. & Hyyppä, H., 2013: Airborne laser scanning and digital stereo imagery measures of forest structure: comparative results and implications to forest mapping and inventory update. – Canadian Journal of Remote Sensing **39** (05): 382–395.

White, J.C., Wulder, M.A., Vastaranta, M., Coops, N.C., Pitt, D. & Woods, M., 2013a: The utility of image-based point clouds for forest inventory: A comparison with airborne laser scanning. – Forests **4** (3): 518–536.

White, J.C., Wulder, M.A., Varhola, A., Vastaranta, M., Coops, N.C., Cook, B.D., Pitt, D. & Woods, M., 2013b: A best practices guide for generating forest inventory attributes from airborne laser scanning data using an area-based

approach. – Canadian Wood Fibre Centre, Victoria, BC, Canada. – http://cfs.nrcan.gc.ca/publications?id=34887 (7.3.2016).

White, J., Stepper, C., Tompalski, P., Coops, N. & Wulder, M., 2015: Comparing ALS and image-based point cloud metrics and modelled forest inventory attributes in a complex coastal forest environment. – Forests **6** (10): 3704–3732.

Woods, M., Pitt, D., Penner, M., Lim, K., Nesbitt, D., Etheridge, D. & Treitz, P., 2011: Operational implementation of a LiDAR inventory in Boreal Ontario. – The Forestry Chronicle **87** (4): 512–528.

Yu, X., Hyyppä, J., Holopainen, M. & Vastaranta, M., 2010: Comparison of area-based and individual tree-based methods for predicting plot-level forest attributes. – Remote Sensing **2** (6): 1481–1495.

Address of the Authors:

Dr. Christoph Straub & M.Sc. Christoph Stepper, Bavarian State Institute of Forestry (LWF), Department of Information Technology, Hans-Carl-von-Carlowitz-Platz 1, D-85354 Freising, Tel: +49(0)8161-71-5875, Fax: +49(0)8161-71-4971, e-mail: {christoph.straub}, {christoph.stepper}@lwf.bayern.de

Manuskript eingereicht: Dezember 2015
Angenommen: April 2016

PFG 2016 / 3, 125–140
Stuttgart, Juni 2016

Article

Tri-Stereo Model Orientation of High-Resolution Satellite Imagery Combining Ground Control Points and Lines

Jinshan Cao, Xiuxiao Yuan & Yi Fang, Wuhan, China

Keywords: orientation, tri-stereo model, high-resolution satellite imagery, ground control lines, rational function model

Summary: An effective tri-stereo model orientation approach for high-resolution satellite imagery (HRSI) combining ground control points (GCPs) and ground control lines (GCLs) is presented. For the presented approach, both the point-based and the line-based orientation models employ the rational function model rather than the physical sensor model as the geometric imaging model of HRSI. As the parameters of a rational model are frequently distributed with HRSI data, our model is more convenient and practicable for users. The experimental results of two ZiYuan-3 (ZY-3) datasets have shown that in images where it is difficult to identify sufficient and well-distributed GCPs, GCLs can be employed to substitute for the absent GCPs. More specifically, an accuracy better than the ground sample distance (GSD) can be achieved after the tri-stereo model orientation combining three GCPs and one GCL, two GCPs and two GCLs, or one GCP and five GCLs. Additionally, if only GCLs are taken as the control information in the HRSI orientation, a satisfactory accuracy of better than 1 GSD can also be achieved using eight GCLs of appropriate orientations near the image boundaries.

Zusammenfassung: *Tri-Stereo Modellorientierung von hochaufgelösten Satellitenszenen mit einem kombinierten Passpunkt- und Passlinienverfahren.* In diesem Beitrag wird ein effektiver Ansatz zur Modellorientierung von Tripeln von überlappenden hoch aufgelösten Satellitenbildern vorgestellt, welcher Passpunkte (PP) mit Passlinien (PL) kombiniert. Dabei beruhen weder die punkt- noch die linienbasierten Orientierung auf einem physikalischen Sensormodell, sondern auf einem Modell auf der Basis von rationalen Funktionen. Da die Parameter eines Modells auf Basis von rationalen Funktionen häufig mit den Satellitendaten mitgeliefert werden, ist dieses Modell für Anwender einfacher zu nutzen. Die Ergebnisse von Experimenten mit zwei Bildtripeln, die vom Satelliten ZiYuan-3 (ZY-3) aus aufgenommen wurden, haben gezeigt, dass in Bildern, in denen es schwierig ist, eine ausreichende Anzahl von PP mit einer guten räumlichen Verteilung zu identifizieren, PL ein guter Ersatz für PP sein können. Insbesondere wird gezeigt, dass eine Genauigkeit, die besser als die Bodenauflösung (Ground Sampling Distance, GSD) der Bilder ist, erreicht werden kann, wenn drei PP mit einer PL, zwei PP mit zwei PL oder ein PP mit fünf PL kombiniert werden. Selbst wenn keine PP zur Verfügung steht, kann die Orientierung eines Bildtripels mit einer Genauigkeit besser als 1 GSD erfolgen, wenn mindestens acht PL in der Nähe der Bildränder mit geeigneter Verteilung vorliegen.

1 Introduction

Precise orientation is a prerequisite for many applications of high-resolution satellite imagery (HRSI). The orientation accuracy determines the geometric quality of the products derived from HRSI, such as digital elevation models (DEM) and digital orthophoto maps (DOM). At present, HRSI orientation usually takes ground control points (GCPs) as the control information to relate image space and object space (Grodecki & Dial 2003, Fraser & Hanley 2005, Fraser et al. 2006). The GCPs are mainly surveyed in the field or extracted from the reference DOM and DEM. However, due to the lack of clear point features in the

 www.schweizerbart.de
DOI: 10.1127/pfg/2016/0293 1432-8364/16/0293 $ 4.25

field or the large time interval between the acquisition of the HRSI and the reference DOM and DEM, it may be very difficult to identify sufficient, evenly distributed and highly accurate GCPs in the areas covered by an image. In these cases, the image orientation using both GCPs and ground control lines (GCLs) can offer an alternative solution for precise orientation.

The use of linear features is not a recent advancement in photogrammetry. Masry (1981) already presented the original idea in 1981. Compared with point features, linear features are preferred in photogrammetry mainly due to the following reasons (Habib et al. 2004, Schenk 2004, Karjalainen et al. 2006): (1) Control information in object space is more readily available in the form of linear features for the purpose of the image orientation. (2) Linear features can be easily identified in the image. (3) Information from linear features can be used even without a complete match between image and object linear features. (4) Linear features form a good basis for the automation of photogrammetric processes.

With respect to the HRSI orientation using only GCPs, a lot of research has been done, such as Grodecki & Dial (2003), Fraser & Hanley (2005), Fraser et al. (2006) and Zhang et al. (2009). This is also true for applications of linear features in photogrammetry. In aerial photogrammetry, linear features were used successfully in the relative orientation, exterior orientation and aerial triangulation (Zhang et al. 2011, Karjalainen et al. 2006, Habib et al. 2003, Schenk, 2004). In space photogrammetry, Shi & Shaker (2006) established a line-based transformation model, whose structure is similar to some point-based transformation models, for image-to-image registration. Habib & Alruzouq (2004) used linear features as the registration primitives to perform automatic image registration of multi-source satellite images. The approach was shown to be feasible and robust even without a complete correspondence between the registration primitives in the reference and input images. Zhang et al. (2004) performed an automatic exterior orientation of SPOT-3 images using GCLs and achieved an orientation accuracy of about 1.5 pixels. Tommaselli & Medeiros (2010) presented an experimental assessment of both the line-coplanarity model and the adapted equivalent planes model for the indirect orientation of CBERS-2 images using GCLs. The experimental results showed that an accuracy of about twice the ground sample distance (GSD) at independent check points (ICPs) can be achieved. Tommaselli & Marcato Junior (2012) and Marcato Junior & Tommaselli (2013) combined GCPs, GCLs, and orbital data to perform the block adjustment of CBERS-2B images. It was observed that the combination of GCPs and GCLs could provide better results than the conventional bundle block adjustment using only GCPs.

For the orientation of remote sensing imagery using GCLs, as in aerial or space photogrammetry, the most important thing is to establish a mathematical model relating image space and object space. The present line-based models for HRSI orientation can be mainly divided into two categories: the collinearity model and the coplanarity model, the latter being preferred in space photogrammetry (Tommaselli & Medeiros 2010). In order to establish the coplanarity model, the satellite's position and attitude observations and sensor parameters are indispensable. However, many HRSI satellites, such as IKONOS, GeoEye-1, and ZiYuan-3 (ZY-3), only provide the users with rational polynomial coefficients (RPCs; Fraser et al. 2006) rather than the satellite's position and attitude observations and sensor parameters. In other words, users can only establish the rational functional model (RFM) according to the RPCs, and it is very difficult and even impossible for them to perform HRSI orientation using GCLs based on the coplanarity model. Therefore, a line-based orientation model for the RFM is established and a tri-stereo model orientation approach for HRSI combining GCPs and GCLs is presented in this paper. For the presented approach, only the RPCs rather than the satellite's position and attitude observations and sensor parameters are necessary, so that it is more convenient and practicable for HRSI users. The paper is organised in four sections. In the next section, both the point-based and line-based orientation models are established, and the solutions for the unknowns are introduced briefly. In the following section, the experiments with two ZY-3 datasets are performed to val-

idate the feasibility and effectiveness of the tri-stereo model orientation both using GCLs only and combining GCPs and GCLs. Finally, conclusions are provided.

2 Orientation Models and Solutions

When performing the RFM-based tri-stereo model orientation combining GCPs and GCLs, both GCPs and GCLs are employed as the control information and tie points are used to supply internal geometric constraints between the adjacent satellite images. Hence, the mathematical models of image orientation can be classified into two categories: the point-based orientation model and the line-based orientation model.

2.1 Point-based Orientation Model

For HRSI orientation using point features, the RFM with additional affine transformation parameters (ATPs) is usually employed as the mathematical model. In the RFM, the image point coordinates (r, c) are expressed as the ratios of polynomials of the reduced object point coordinates (X_n, Y_n, Z_n):

$$\begin{cases} r_n = \dfrac{P_1(X_n, Y_n, Z_n)}{P_2(X_n, Y_n, Z_n)} \\ c_n = \dfrac{P_3(X_n, Y_n, Z_n)}{P_4(X_n, Y_n, Z_n)} \end{cases} \tag{1}$$

where (r_n, c_n) are the normalized values of the image point coordinates (r, c), whereas the normalised object coordinates are determined from the original object point coordinates (X, Y, Z). The normalization of the coordinates is carried out in the way described in Tao & Hu (2001). $P_i(X_n, Y_n, Z_n)(i = 1,2,3,4)$ are the third-order polynomials with X_n, Y_n and Z_n as the independent variables.

Research has shown that using the RFM to fit the physical sensor model (PSM) with the terrain-independent scenario can achieve a very high accuracy and the fitting errors can be ignored (Tao & Hu 2001, Yuan & Lin 2008, Nagasubramanian et al. 2007). Using the RFM instead of the PSM to perform image orientation, feature extraction, orthorectification and three-dimensional reconstruction is entirely feasible (Fraser et al. 2002, Tao et al. 2004). However, in order to achieve the best orientation results, the absolute orientation has to be improved. Therefore, the point-based orientation model is actually the bias corrected RPC-solution with two-dimensional affine transformation as follows:

$$\begin{cases} r + e_0 + e_1 r + e_2 c = \dfrac{P_1(X_n, Y_n, Z_n)}{P_2(X_n, Y_n, Z_n)} r_s + r_o \\ c + f_0 + f_1 r + f_2 c = \dfrac{P_3(X_n, Y_n, Z_n)}{P_4(X_n, Y_n, Z_n)} c_s + c_o \end{cases} \tag{2}$$

where (r_o, c_o) and (r_s, c_s) are, respectively, the offset values and scaling values of the image point coordinates; (e_0, e_1, e_2,f_0,f_1,f_2) are the ATPs and ($e_0 + e_1 r + e_2 c, f_0 + f_1 r + f_2 c$) can be considered as the error correction values of the image point coordinates.

2.2 Line-based Orientation Model

As shown in Fig. 1, a straight line L in object space is determined by two points P_1 and P_2, whose object coordinates are known. The straight line l_T in image space corresponds to L, and the point t is an arbitrary point on the line l_T. A straight line l_P in image space is determined by the image points p_1 and p_2, which can be obtained by projecting the points P_1 and P_2 into the image according to (1). In this paper, the line l_T is called the "observed line" and the line l_P is called the "projected line".

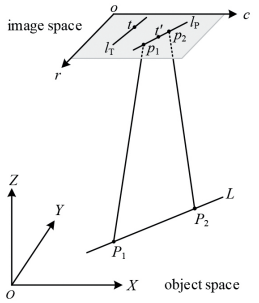

Fig. 1: Relation between linear features in object space and in HRSI.

If the RPCs do not contain systematic errors, the observed line l_T and the projected line l_p are bound to coincide, that is, the point t is bound to lie on the line l_p. In reality, however, the point t will deviate from the line l_p, resulting from the influence of the systematic errors in the RPCs. Therefore, the ATPs according to (2) should be determined so that after the correction of its image coordinates the geometric constraint that the point t lies on the line l_p is satisfied.

Suppose that the point t' in Fig. 1 is obtained by correcting the systematic errors of the point t, and then the point t' should lie on the line l_p. Additionally, the image coordinates of the points t and t' satisfy the two-dimensional affine transformation as follows:

$$\begin{cases} r_{t'} = r_t + e_0 + e_1 r_t + e_2 c_t \\ c_{t'} = c_t + f_0 + f_1 r_t + f_2 c_t \end{cases} \tag{3}$$

where (r_t, c_t) and $(r_{t'}, c_{t'})$ are, respectively, the image coordinates of the points t and t' and the coefficients e_j, f_j are the ATPs also defined in (2).

A straight line in image space has several mathematical expressions, such as slope-intercept form, point-slope form and two-point form. In this paper, the slope-intercept form is employed to express the line l_p, so as to establish the line-based orientation model conveniently. Meanwhile, taking into account the influence of the line slope on the image orientation, the lines in image space are divided into two types according to the angle θ between the line and the c-axis of the image coordinate system o-rc, as shown in Fig. 2. If the angle θ satisfies the condition $-45° \le \theta \le 45°$, (4) is employed to express line l_p; otherwise, (5) is used:

$$r = kc + b \tag{4}$$

$$c = kr + b \tag{5}$$

In (4) and (5), k and b are the slope and the intercept, respectively, of the line l_p, which can be obtained from the image coordinates of the points p_1 and p_2.

According to the geometric constraint that the point t' lies on the line l_p, the image coordinates of the point t' should satisfy (4) or (5), so (6) and (7) can be obtained:

$$r_{t'} = kc_{t'} + b \tag{6}$$

$$c_{t'} = kr_{t'} + b \tag{7}$$

Substituting (3) into (6) and (7), respectively, the line-based orientation model can be established as shown in (8) and (9):

$$r_t = -e_0 - r_t e_1 - c_t e_2 + kf_0 + kr_t f_1 + kc_t f_2 + kc_t + b \tag{8}$$

$$c_t = ke_0 + kr_t e_1 + kc_t e_2 - f_0 - r_t f_1 - c_t f_2 + kr_t + b \tag{9}$$

The point t in image space is an arbitrary point on the observed line l_T rather than the corresponding point of one of the object points P_1 or P_2. Therefore, when establishing the line-based orientation model, the point on the image line does not have to correspond with a specific point on the object line, but only the correspondence between the image line and the object line is necessary. Consequently, linear features are preferable to point features in areas where GCPs are difficult to be identified.

2.3 Simultaneous Adjustment

From (8) and (9), it can be seen that no additional unknowns are introduced when establishing the line-based orientation model using GCLs. Therefore, when performing the tri-stereo model orientation combining GCPs and GCLs, the unknowns are still the ATPs of each image and the object coordinates of each tie point. In theory, one observation equation, either (8) or (9), can be established for each image point on an observed line l_T. In this paper, only two image points t_1 and t_2 per line l_T are used in the tri-stereo model orientation, since any observed line can be determined by two image points. The general procedure of solving the unknowns is as follows:

(1) For each GCL in each image, the image points p_1 and p_2 are, respectively, obtained by projecting the points P_1 and P_2 observed on the object line L into the image according to (1) and then the slope k and the intercept b of the projected line l_p are computed using the image coordinates of the resultant points p_1 and p_2. After that, according

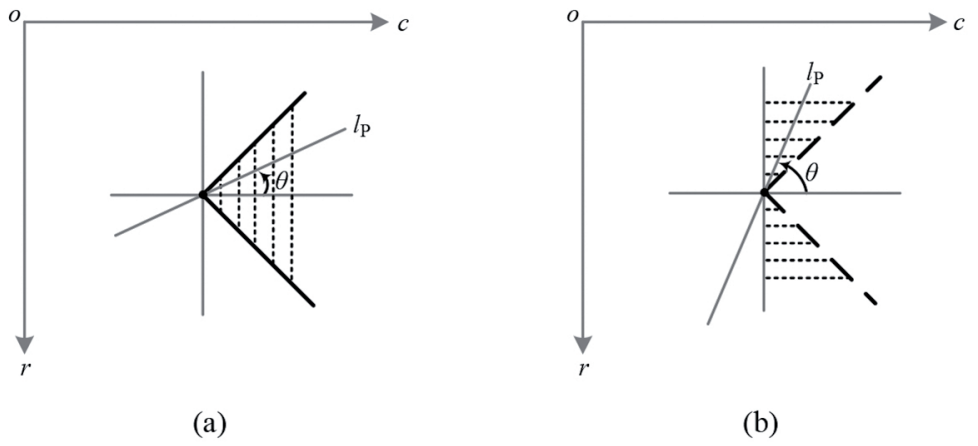

Fig. 2: Two types of straight lines in image space: (a) $-45° \leq \theta \leq 45°$, (b) $45° < \theta < 90°$ and $-90° \leq \theta < -45°$.

to (8) or (9), two error equations are established using the image coordinates of the observed points t_1 and t_2 on the observed line l_T. That is, each of the two points contributes one error equation.

(2) For each GCP in each image, according to (2), two error equations are established using the observed image and object coordinates of the GCP.

(3) For each tie point in each image, according to (2), two error equations are established using the observed image coordinates of the tie point.

(4) Combining the error equations relating to GCLs, GCPs and tie points, the ATPs and the object coordinates of tie points are solved simultaneously by least-squares adjustment.

3 Experimental Results and Analysis

3.1 Experimental Datasets

In this study, two sets of ZY-3 three-line camera (TLC) images were tested. The general characteristics of the datasets are depicted in Tab. 1. Both datasets have three images in the forward (FWD), nadir (NAD) and backward (BWD) views, respectively. The GSD of the FWD, NAD and BWD images is about 3.5 m, 2.1 m and 3.5 m, respectively. The swath width of the FWD, NAD and BWD cameras is about 51 km. The FWD and BWD cameras are tilted by +22° and -22° from the NAD camera, respectively, and form a base-to-height ratio of 0.87 with Earth curvature considered. The object coordinates of the GCLs and GCPs in both datasets were measured manually from the reference DOM and DEM. The GSD of the DOM is 0.2 m and the planimetric accuracy is about 1.0 m. The point spacing of the DEM is 1.0 m and the height accuracy is about 2.0 m. The image coordinates of the GCLs and GCPs in every ZY-3 image were also measured manually and the measurement accuracy is about 0.4 pixel. The tie points were extracted and matched automatically in the FWD, NAD and BWD images using the matching algorithm presented in Yuan & Liu (2009). In the following experiments, the FWD, NAD and BWD images in each dataset formed a tri-stereo model, and the tri-stereo model orientation was performed according to the procedure in section 2.3. In the experiments described in sections 3.2 to 3.4, only the GCLs and tie points were used; in section 3.2, results for GCLs and GCPs are compared. In the experiments reported in section 3.5, the GCPs, GCLs and tie points were used.

As shown in Fig. 3, the GCPs, GCLs and tie points are distributed evenly in the areas depicted in the images. The GCLs are mainly road edges and river edges in this paper. When

Tab. 1: General characteristics of the datasets.

Characteristics	Dataset 1	Dataset 2
Geographic area of images	Wuhan, China	Wuhan, China
Number of images	3	3
Acquisition date	20th June 2012	22nd April 2012
Terrain relief	18 to 252 m	16 to 107 m
Number of GCLs	39	39
Number of GCPs	54	47
Number of tie points	41	38

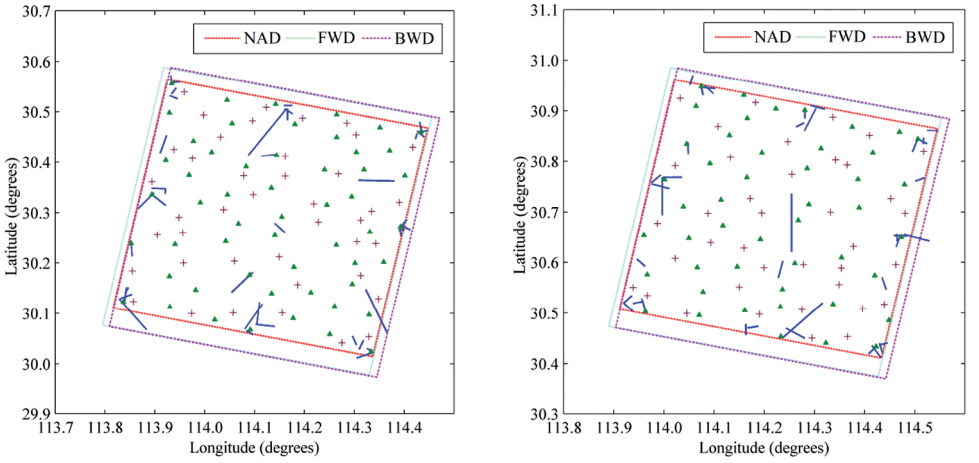

Fig. 3: Distributions of the GCPs and GCLs in the: (a) dataset 1, (b) dataset 2. Note that ▲ denotes GCPs, — denotes GCLs, + denotes tie points. For better readability, the lengths of the GCLs were scaled by a factor five.

measuring the GCLs, the object coordinates of the points P_1 and P_2 on a straight line L were determined based on the reference DOM and DEM, and then the image coordinates of the points t_1 and t_2 on the corresponding image line l_T were measured. Note that the two points on the image line need not (and in general do not) correspond with the ones on the line in the reference DOM and DEM.

3.2 *Effects of the Number and Distribution of GCLs on the Tri-Stereo Model Orientation Using GCLs*

For the tri-stereo model orientation of ZY-3 images, each GCP delivers two observations and each point on a GCL delivers one observation. Therefore, no less than three GCPs or three GCLs are theoretically required to determine the ATPs. However, when using GCLs, one has to take care that the directions of the lines allow for a solution of the resultant normal equation system; the lengths of the line segments also have an impact on the determinability of the parameters. Furthermore, more observations may be required for obtaining an accurate and numerically stable solution. In this section, in order to firstly analyse the effects of the number and distribution of GCLs on the tri-stereo model orientation, one GCP layout scenario and five different GCL layout scenarios were designed. The layouts are as follows:

(1) *Layout P4*. Four GCPs in the image corners, as shown in Fig. 4a;
(2) *Layout L4*. Four GCLs in the image corners, as shown in Fig. 4b;
(3) *Layout L6*. Six GCLs along the along-track image boundary, as shown in Fig. 4c;
(4) *Layout L8*. Eight GCLs near the image boundary, as shown in Fig. 4d; and
(5) *Layout L15*. Eight GCLs near the image boundary and seven GCLs distributed evenly in the image, as shown in Fig. 4e.

For each dataset in Fig. 3, the satisfactory GCPs and GCLs were selected according to the above layout scenarios, and the remaining GCPs were considered as the ICPs. Note that the angles θ of the selected GCLs are distributed evenly in the four angle ranges [-90º, -45º], [-45º, 0º], [0º, 45º] and (45º, 90º), as listed in Tabs. 2 and 3, and the effects of the directions and the lengths of GCLs on the tri-stereo model orientation will be analysed in the following sections. After the tri-stereo model orientation according to the procedure in section 2.3, the root-mean-square errors (RMSE) of the object coordinates at the ICPs were calculated. They are listed in Tabs. 2 and 3.

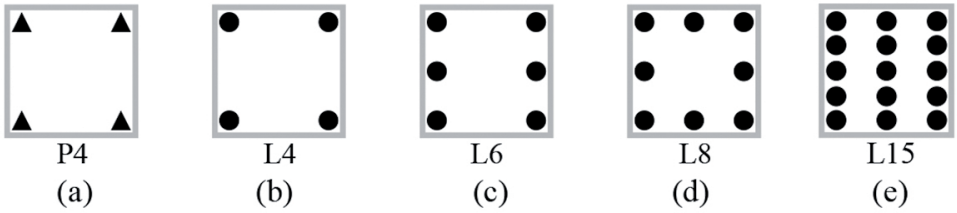

Fig. 4: GCP and GCL layout scenarios: (a) four GCPs, (b) four GCLs, (c) six GCLs, (d) eight GCLs, (e) fifteen GCLs. Note that ▲ denotes GCPs and ● denotes GCLs.

Tab. 2: Tri-stereo model orientation results using the GCPs and GCLs in the dataset 1.

Layout	Angles of GCLs in the NAD image (º)	Number of ICPs	RMSE (m)			
			North	East	Planimetry	Height
P4	/	50	1.916	2.035	2.795	2.116
L4	-86, -35, 23, 73	54	107.184	60.760	123.208	84.097
L6	-86, -35, 18, 23, 73, 79	54	3.642	3.258	4.887	5.450
L8	-86, -66, -35, -5, 18, 23, 73, 79	54	2.089	2.009	2.899	2.202
L15	-86, -84, -66, -59, -35, -20, -11, -5, 18, 23, 34, 55, 73, 74, 79	54	2.215	1.779	2.841	2.099

Tab. 3: Tri-stereo model orientation results using the GCPs and GCLs in the dataset 2.

Layout	Angles of GCLs in the NAD image (º)	Number of ICPs	RMSE (m)			
			North	East	Planimetry	Height
P4	/	43	2.205	1.790	2.840	2.065
L4	-57, -27, 35, 81	47	75.257	56.173	93.909	77.615
L6	-86, -57, -27, 5, 35, 81	47	6.300	2.153	6.658	7.129
L8	-86, -57, -42, -27, 5, 19, 35, 81	47	1.904	1.978	2.745	2.083
L15	-89, -86, -57, -57, -42, -35, -27, 5, 19, 33, 35, 61, 77, 78, 81	47	1.582	2.210	2.718	2.090

From the results in Tabs. 2 and 3, the following four conclusions can be drawn. First, the orientation accuracy achieved using four GCLs in the layout L4 is much worse than the one achieved using four GCPs, even if the angles of the GCLs are distributed evenly in the four angle ranges. In our experiments, the control information provided by four GCLs is insufficient for an accurate tri-stereo model orientation, but this may also be affected by the specific configuration of GCLs with the given directions in the images and with given lengths. The normal equation matrix of the least-squares adjustment is ill-conditioned, and the solved ATPs and the object coordinates of the tie points deviate from their true values. Take the dataset 1 for an example. The standard deviations (SDs) of the solved ATPs of the NAD image even reach values as large as about 80 pixels, as listed in Tab. 4. As a result, the solved ATPs cannot effectively compensate the systematic errors in the RPCs at all. The residual errors of the ICPs are still very large, as shown in Fig. 5a, which is also consistent with the SDs of the tie points in Fig. 6a. Note that the SDs of both, the solved ATPs and the tie points, were derived from the SD of the unit weight and the co-factor matrix after least-squares adjustment.

Second, when using six GCLs in the layout L6 to perform the tri-stereo model orientation, the solved ATPs deviate from the values achieved when using points, as listed in Tab. 4. The orientation accuracies of both datasets are worse than 1 GSD (3.5 m in this paper). The reason is again to be found in the specific arrangement of GCLs in these examples. It is demonstrated that it is very difficult to achieve the best orientation accuracy using the layout L6, even if the directions of the selected GCLs are distributed evenly.

When eight GCLs are employed as control information (in the layout L8), the deviation of the solved ATPs from the point-based solution can be further reduced and a satisfactory orientation accuracy can be achieved. Again, take the dataset 1 for an example. The SDs of the parameters e_0 and f_0 of the NAD image are better than 0.4 pixel, and the SDs of the other ATPs are better than 1.8E-5. Accordingly, the residual errors of the ICPs are further reduced, as shown in Fig. 5b, which is also consistent with the SDs of the tie points in Fig. 6b. The orientation accuracy is improved to 2.9 m in planimetry and 2.2 m in height, which is almost the same as the one achieved with the layout P4. It is demonstrated that in order to achieve a good orientation result, at least eight GCLs near the boundary of the areas are necessary, but this result heavily depends on the distribution of the GCL directions.

Finally, the orientation accuracy cannot be improved significantly any more with the number of GCLs increased from eight in the layout L8 to fifteen in the layout L15. For both datasets, the difference between the accuracies achieved with the layouts L8 and L15 is smaller than 0.1 m in planimetry and 0.2 m in height. It means that using more GCLs one can hardly expect large improvements of the orientation accuracy, even if the GCLs are distributed evenly in the areas covered by the images.

Tab. 4: The solved ATPs of the NAD image in the dataset 1.

Layout	e_0 (pixels) (SD)	e_1 (SD)	e_2 (SD)	f_0 (pixels) (SD)	f_1 (SD)	f_2 (SD)
P4	9.519E+0 (2.463E-1)	-9.224E-5 (1.177E-5)	7.626E-6 (1.125E-5)	-8.825E+0 (2.389E-1)	4.280E-5 (1.144E-5)	-1.258E-5 (1.094E-5)
L4	1.505E+1 (7.968E+1)	2.762E-3 (3.335E-3)	-4.642E-3 (1.488E-3)	-5.199E+0 (2.470E+1)	-4.426E-3 (1.779E-3)	4.306E-4 (1.166E-3)
L6	1.444E+1 (8.538E-1)	-2.101E-4 (2.701E-5)	-1.533E-4 (2.665E-5)	-5.751E+0 (3.755E-1)	-2.104E-4 (3.042E-5)	-8.235E-5 (1.675E-5)
L8	9.349E+0 (3.899E-1)	-3.862E-5 (1.314E-5)	-1.210E-5 (1.645E-5)	-7.988E+0 (1.919E-1)	-4.427E-5 (1.787E-5)	1.061E-5 (1.148E-5)
L15	8.627E+0 (2.224E-1)	-2.205E-5 (9.347E-6)	9.420E-6 (9.620E-6)	-7.810E+0 (1.314E-1)	-1.886E-5 (8.561E-6)	-3.965E-6 (7.651E-6)

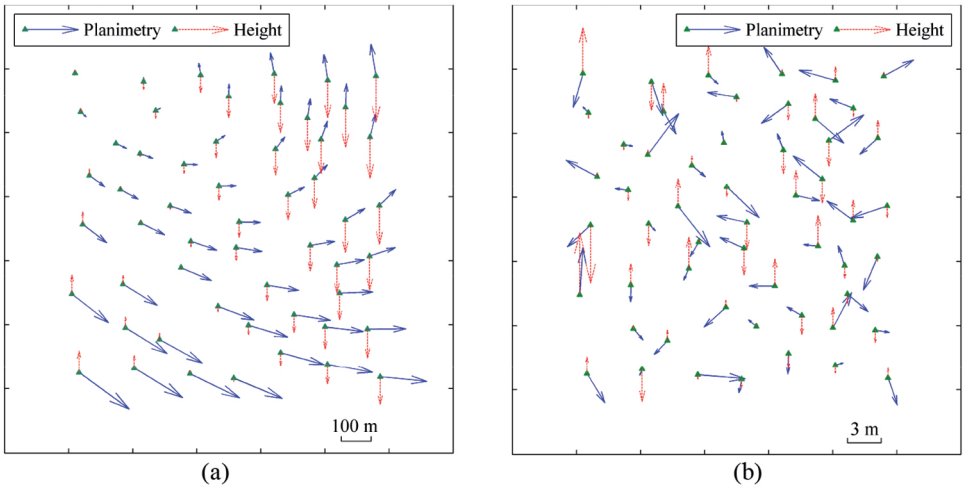

Fig. 5: Residual error distributions of the ICPs after the tri-stereo model orientation with: (a) layout L4, (b) layout L8 in the dataset 1.

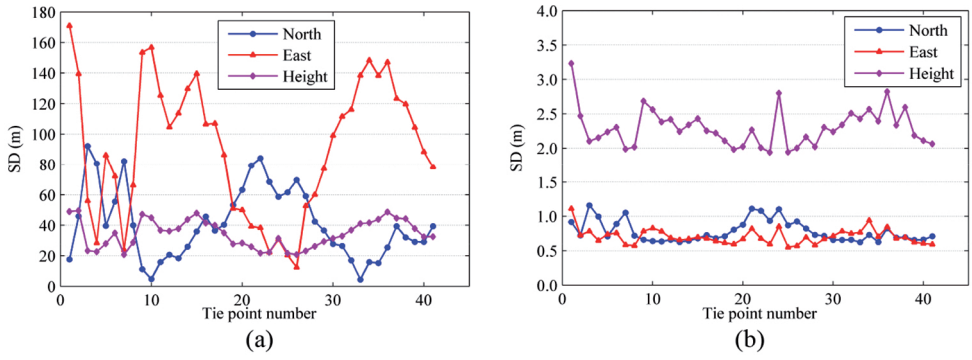

Fig. 6: SDs of the tie points after the tri-stereo model orientation with: (a) layout L4, (b) layout L8 in the dataset 1.

From the above experiments, it can be concluded that performing the tri-stereo model orientation using GCLs is feasible and effective. With eight GCLs near the image boundary, the orientation can achieve an accuracy of better than 1 GSD, which is almost the same as the one achieved using GCPs. Therefore, in the areas where it is difficult to identify highly accurate GCPs, using GCLs to perform the image orientation can offer an alternative solution for the precise HRSI orientation. Especially, if the control information is extracted from the existing topographical maps, GCLs will be preferable to GCPs. The existing topographical maps have much more linear features than point features and a complete match between the line in the satellite image and the one in the topographical maps is unnecessary, so it will be feasible to extract GCLs and not to extract GCPs.

3.3 *Effects of the Directions of GCLs on the Tri-Stereo Model Orientation Using GCLs*

Different from GCPs, the directions of GCLs is another important factor that might affect the tri-stereo model orientation. In order to analyse the effects of the directions of GCLs, the angle θ of GCLs in image space is divided into four ranges: [-90º, -45º), [-45º, 0º), [0º, 45º] and

[45º, 90º]. The layout L8 in section 3.2 continued to be used, but ten groups of eight GCLs with different angles, as listed in Tab. 5, were tested. The RMSE of the ICPs was listed in Tabs. 6 and 7. It is noted that in Tabs. 6 and 7, the angles of the used GCLs in only the NAD images were listed and the angles in the FWD and BWD images are almost the same as those in the NAD images.

In Tabs. 6 and 7, with the groups G1, G2, G3 and G4, for both datasets the best orientation accuracy achieved is about 1 GSD and the worst accuracy is about 3 GSD. In fact, when the angles of eight GCLs all lie in only one angle range [-90º, -45º], [-45º, 0º], [0º, 45º] or [45º, 90º], that is, when the difference between the angles is small, the offset and scaling of the affine transformation model (ATM) may be poorly defined, and as a result, the orientation accuracy is unstable. When the angles of eight GCLs are distributed evenly in two or three angle ranges, the offset and scaling of the ATM can be restrained and the orientation accuracy can be improved to a satisfactory level. For both datasets, the orientation accuracies achieved with the groups G12, G13, G14, G123, G124 and G134 are all better than 1 GSD. Hence, in order to achieve a satisfactory orientation accuracy, it is recommended that the angles of eight GCLs in the layout L8 should be distributed evenly in at least two out of the four angle ranges.

3.4 Effects of the Lengths of GCLs on the Tri-Stereo Model Orientation Using GCLs

Similarly, in order to analyse the effects of the lengths of GCLs on the tri-stereo model orientation, eight GCLs in the layout L8 in section 3.2 are used, but the lengths of the eight GCLs were changed into [40, 60], [80, 100], [120, 140], [160, 180] and [200, 220] m, respectively.

Tab. 5: Ten groups of eight GCLs with different angles.

Group	Number of GCLs in [-90º, -45º]	Number of GCLs in [-45º, 0º]	Number of GCLs in [0º, 45º]	Number of GCLs in [45º, 90º]
G1	8	0	0	0
G2	0	8	0	0
G3	0	0	8	0
G4	0	0	0	8
G12	4	4	0	0
G13	4	0	4	0
G14	4	0	0	4
G123	2	3	3	0
G124	2	3	0	3
G134	2	0	3	3

Tab. 6: Tri-stereo model orientation results using the GCLs in the dataset 1.

Group	Angles of GCLs in the NAD image (º)	Number of ICPs	RMSE (m)			
			North	East	Planimetry	Height
G1	-86, -80, -78, -74, -69, -66, -65, -61	54	2.258	2.507	3.374	3.391
G2	-35, -33, -25, -20, -17, -11, -11, -5	54	6.159	4.014	7.351	2.137
G3	13, 18, 23, 23, 24, 30, 33, 40	54	5.261	1.782	5.555	1.954
G4	57, 67, 70, 73, 78, 79, 84, 86	54	4.216	8.802	9.760	11.195
G12	-78, -66, -65, -61; -35, -25, -17, -5	54	2.205	2.055	3.014	2.238
G13	-78, -66, -65, -61; 13, 23, 33, 40	54	2.333	1.864	2.986	2.283
G14	-78, -66, -65, -61; 67, 73, 84, 86	54	2.375	2.256	3.276	2.125
G123	-78, -65; -35, -17, -5; 24, 30, 33	54	2.062	1.926	2.822	2.246
G124	-78, -65; -35, -17, -5; 67, 78, 79	54	2.054	2.168	2.986	2.381
G134	-78, -65; 13, 23, 40; 67, 78, 79	54	2.206	2.210	3.122	2.302

Tab. 7: Tri-stereo model orientation results using the GCLs in the dataset 2.

Group	Angles of GCLs in the NAD image (°)	Number of ICPs	RMSE (m)			
			North	East	Planimetry	Height
G1	-86, -85, -82, -78, -60, -57, -57, -56	47	2.504	5·978	6.481	9.212
G2	-42, -27, -26, -22, -12, -10, -10, -6	47	4.569	2.616	5.265	1.971
G3	4, 5, 6, 18, 19, 33, 35, 44	47	3.038	1.508	3.392	2.384
G4	63, 65, 69, 76, 78, 78, 78, 81	47	3.673	5.682	6.766	6.393
G12	-85, -82, -57, -56; -42, -27, -26, -10	47	1.664	2.600	3.087	2.442
G13	-85, -82, -57, -56; 4, 6, 33, 44	47	1.635	2.529	3.011	2.177
G14	-85, -82, -57, -56; 65, 69, 76, 78	47	2.157	1.902	2.876	2.434
G123	-85, -56; -10, -27, -42; 18, 27, 33	47	1.342	2.432	2.778	2.034
G124	-85, -56; -10, -27, -42; 65, 78, 81	47	2.108	1.968	2.884	2.251
G134	-85, -56; 4, 6, 44; 65, 78, 81	47	2.162	1.855	2.848	2.414

After the tri-stereo model orientation, the RMSE of the ICPs was listed in Tabs. 8 and 9. In Tabs. 8 and 9, the orientation accuracy changes slightly when the lengths of the GCLs increase. For both datasets, the difference between the accuracy achieved with the GCLs in [40, 60] m and that achieved with the GCLs in [200, 220] m is smaller than 0.1 m in both planimetry and height. It can be concluded that the lengths of GCLs have almost no effect on the tri-stereo model orientation when eight GCLs with a good distribution of directions are used, so the orientation using GCLs can be performed conveniently for users. In real imagery, however, it may be difficult to find very long features, e.g. road or river edges,

Tab. 8: Tri-stereo model orientation results using the GCLs in the dataset 1.

Layout	Lengths of GCLs in object space (m)	Number of ICPs	RMSE (m)			
			North	East	Planimetry	Height
L8	[40, 60]	54	1.987	1.974	2.801	2.088
L8	[80, 100]	54	1.868	2.059	2.780	2.156
L8	[120, 140]	54	1.974	1.981	2.797	2.087
L8	[160, 180]	54	2.027	2.029	2.868	2.164
L8	[200, 220]	54	2.131	1.956	2.893	2.023

Tab. 9: Tri-stereo model orientation results using the GCLs in the dataset 2.

Layout	Lengths of GCLs in object space (m)	Number of ICPs	RMSE (m)			
			North	East	Planimetry	Height
L8	[40, 60]	47	1.553	2.188	2.683	2.155
L8	[80, 100]	47	1.729	2.099	2.719	2.107
L8	[120, 140]	47	1.821	2.122	2.796	2.167
L8	[160, 180]	47	1.939	1.993	2.780	2.123
L8	[200, 220]	47	1.773	2.134	2.775	2.154

that are strictly linear and, thus, can be used as GCLs. Our results show that using relatively short GCPs of a length of about 15–20 pixels are sufficient to obtain a good orientation accuracy.

3.5 Accuracy Analysis of the Tri-Stereo Model Orientation Combining GCPs and GCLs

The experiments described in the previous sections have already shown that four GCPs in the image corners or eight GCLs near the image boundary whose angles are distributed evenly in at least two out of the four angle ranges are sufficient for tri-stereo model orientation. However, it may be difficult to employ only GCPs or GCLs for the orientation in some cases. In comparison, performing the tri-stereo model orientation combining GCPs and GCLs may be a much better solution. Theoretically, no less than three GCPs, two GCPs and one GCLs, or one GCP and two GCLs are required in the tri-stereo model orientation of ZY-3 images, but more observations are required for a stable solution. Based on these considerations, seven layout scenarios were designed to evaluate the feasibility of the orientation combining GCPs and GCLs:

(1) *Layout P3L1*. Three GCPs in three image corners and one GCL in the fourth image corner, as shown in Fig. 7a;
(2) *Layout P3L15*. Three GCPs in three image corners and fifteen GCLs distributed evenly in the image;
(3) *Layout P2L2*. Two GCPs in two image corners and two GCLs in the other two image corners, as shown in Fig. 7b;
(4) *Layout P2L15*. Two GCPs in two image corners and fifteen GCLs distributed evenly in the image;
(5) *Layout P1L3*. One GCP in one image corner and three GCLs in the other three image corners, as shown in Fig. 7c;
(6) *Layout P1L5*. One GCP in one image corner, three GCLs in the other three image corners and two GCLs near the image boundary, as shown in Fig. 7d; and
(7) *Layout P1L15*. One GCP in one image corner and fifteen GCLs distributed evenly in the image.

Combining GCPs and GCLs, one can theoretically determine the offset of the ATM effectively, but cannot always restrain the scaling of the ATM. For example, the scaling may happen in the column direction in Fig. 8a and in the row direction in Fig. 8b, so the normal equation matrix of the least-squares adjustment will be ill-conditioned. Even if the normal equations can be solved because the lines are not exactly parallel, the ATPs thus determined and the object coordinates of tie points will be very uncertain. In order to obtain a stable orientation accuracy, the directions of GCLs should differ enough to restrain the scaling of the ATM.

Based on the analysis of the previous paragraph, for both datasets in Fig. 3, the GCPs and GCLs were selected according to the above layout scenarios and the remaining GCPs were also considered as the ICPs. In each layout, the selected GCLs have different angles, as listed in Tabs. 10 and 11, so that the effects of the directions of GCLs can also be demonstrated conveniently. After the tri-stereo model orientation according to the procedure in section 2.3, the RMSE of the ICPs was calculated and listed in Tabs. 10 and 11.

From the results in Tabs. 10 and 11, the fol-

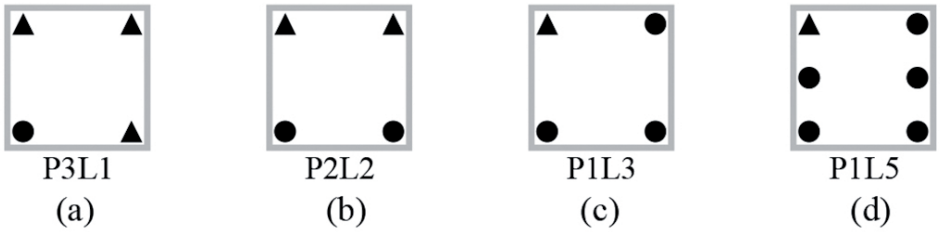

Fig. 7: GCP and GCL layout scenarios: (a) three GCPs and one GCL, (b) two GCPs and two GCLs, (c) one GCP and three GCLs, (d) one GCP and five GCLs. Note that ▲ denotes GCPs and ● denotes GCLs.

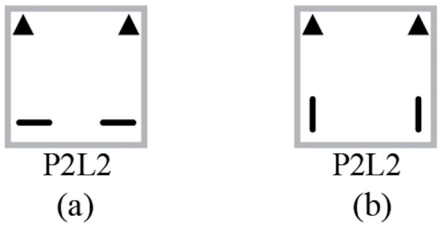

Fig. 8: GCP and GCL layout scenarios: (a) two GCPs and two GCLs, (b) two GCPs and two GCLs. Note that ▲ denotes GCPs and — denotes GCLs.

lowing three conclusions can be drawn. First, combining three GCPs and one GCL in the layout P3L1, or two GCPs and two GCLs in the layout P2L2 can achieve an orientation accuracy of better than 1 GSD, which is almost the same as the one achieved using four GCPs. Moreover, the accuracy is also not improved noticeably when the number of GCLs is increased. Of course, it should be pointed out that for the layout P3L1, the angle of one GCL can be in any of the four angle ranges, but in this case the GCL only gives redundant information, because the ATPs can already be determined from the GCPs. For the layout P2L2, however, the angles of two GCLs should lie in two different angle ranges. When the difference between the angles of the GCLs is too small, the offset and scaling of the ATM may be determined poorly. Consequently, the ATPs and the object space coordinates of the tie points will be very uncertain, indicated by large SDs. Overall, it is feasible and effective to substitute GCLs for the absent GCPs when performing tri-stereo model orientation if GCPs can only be identified in one or two out of the four image corners.

Second, a satisfactory orientation accuracy cannot be achieved combining one GCP and three GCLs in the layout P1L3, even if the angles of three GCLs are distributed evenly in three angle ranges. Taking dataset 1 as an example, the orientation accuracy achieved with the layout P1L3 is as large as 81.2 m in planimetry and 81.5 m in height. The reason is that the control information provided by one GCP and three GCLs is insufficient for a stable tri-stereo model orientation. Accordingly, the offset of the ATM can be restrained effectively by the GCP, but the scaling of the ATM still exists, which can be shown by Tab. 12 and Fig. 9a. The SDs of the shift parameters e_0 and f_0 are better than 1.0 pixel. The SDs of the other ATPs reach only about 1.0E-3, which is much worse than that achieved with the layout P4. Meanwhile, the largest SD of the tie points reaches about 100 m.

Tab. 10: Tri-stereo model orientation results combining the GCPs and GCLs in the dataset 1.

Layout	Angles of GCLs in the NAD image (°)	Number of ICPs	RMSE (m)			
			North	East	Planimetry	Height
P3L1	-78	51	1.808	1.933	2.647	2.132
P3L1	-33	51	1.811	1.943	2.657	2.171
P3L15	-86, -84, -78, -66, -65, -59; -20, -11, -5; 30, 40; 55, 73, 74	51	2.286	1.757	2.883	1.991
P2L2	23, 40	52	5.171	2.038	5.558	6.663
P2L2	-78; 40	52	1.916	1.920	2.712	2.236
P2L2	-78; -35	52	1.849	2.017	2.736	2.116
P2L15	-86, -84, -78, -66, -65, -59; -20, -11, -5; 30, 40; 55, 73, 74	52	2.251	1.735	2.842	2.016
P1L3	-78; -35; 33	53	56.672	58.123	81.179	81.515
P1L5	-86, -78, -74, -65, -61	53	2.349	3.277	4.032	2.724
P1L5*	-86, -78, -65; -35, -11	53	2.061	2.450	3.202	2.247
P1L5	-86, -78, -65; 30, 40	53	2.035	1.755	2.687	2.366
P1L15	-86, -84, -78, -66, -65, -59; -20, -11, -5; 30, 40; 55, 73, 74	53	2.300	1.753	2.892	2.002

Tab. 11: Tri-stereo model orientation results combining the GCPs and GCLs in the dataset 2.

Layout	Angles of GCLs in the NAD image (°)	Number of ICPs	RMSE (m)			
			North	East	Planimetry	Height
P3L1	81	44	1.787	2.094	2.753	2.131
P3L1	18	44	1.803	1.773	2.528	2.025
P3L15	-89, -57; -42, -35, -27, -12, -10, -6; 19, 33; 61, 65, 77, 78, 81	44	1.309	1.576	2.049	2.021
P2L2	69; 81	45	3.187	4.014	5.125	13.506
P2L2	16; 81	45	2.701	1.528	3.103	2.089
P2L2	-6; 81	45	2.022	2.124	2.933	2.668
P2L15	-89, -57; -42, -35, -27, -12, -10, -6; 19, 33; 61, 65, 77, 78, 81	45	1.518	1.668	2.256	2.010
P1L3	-26; 16; 81	46	14.641	7.166	16.300	10.714
P1L5	65, 69, 76, 78, 81	46	2.218	2.925	3.670	6.084
P1L5	-6, -10, -12; 65, 81	46	1.437	2.378	2.778	2.316
P1L5	5, 16, 30; 65, 81	46	2.256	1.734	2.846	2.128
P1L15	-89, -57; -42, -35, -27, -12, -10, -6; 19, 33; 61, 65, 77, 78, 81	46	1.494	1.819	2.354	1.992

Tab. 12: The solved ATPs of the NAD image in the dataset 1.

Layout	e_0 (pixels) (SD)	e_1 (SD)	e_2 (SD)	f_0 (pixels) (SD)	f_1 (SD)	f_2 (SD)
P4	9.519E+0 (2.463E-1)	-9.224E-5 (1.177E-5)	7.626E-6 (1.125E-5)	-8.825E+0 (2.389E-1)	4.280E-5 (1.144E-5)	-1.258E-5 (1.094E-5)
P1L3	8.005E+0 (7.871E-1)	-2.023E-3 (1.068E-3)	-1.384E-3 (7.527E-4)	-8.041E+0 (2.892E-1)	3.002E-3 (1.549E-3)	-2.376E-3 (1.215E-3)
P1L5*	8.900E+0 (2.521E-1)	-7.715E-5 (2.005E-5)	7.797E-5 (2.842E-5)	-8.207E+0 (2.648E-1)	-4.268E-5 (1.306E-5)	1.835E-5 (1.477E-5)
P1L15	9.184E+0 (1.805E-1)	-3.938E-6 (9.232E-6)	-7.969E-5 (9.307E-6)	-7.686E+0 (1.208E-1)	-3.021E-6 (7.386E-6)	-1.960E-5 (6.694E-6)

Note: The layout P1L5* corresponds with the layout P1L5* in Tab. 10.

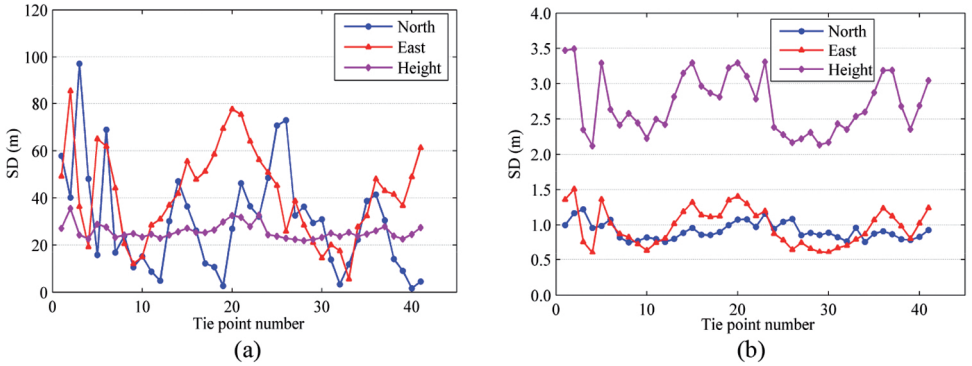

Fig. 9: SDs of the tie points after the tri-stereo model orientation with: (a) layout P1L3, (b) layout P1L5 in the dataset 1.

The offset and scaling of the ATM can be determined effectively in a tri-stereo model orientation combining one GCP and five GCLs, as shown in Tab. 12. The orientation can achieve a satisfactory accuracy of better than 1 GSD, which is consistent with the SDs of the tie points, as shown in Fig. 9b. The angles of five GCLs should also be distributed evenly in at least two out of the four angle ranges. Moreover, the accuracy is not improved noticeably any more as the number of GCLs increases from five to fifteen. Therefore, if only one GCP is available in the image corners, no less than five GCLs near the image boundary are necessary in order to obtain a satisfactory orientation accuracy.

From the above results, it can be concluded that in the image-covered areas where sufficient GCPs in the image corners are unavailable, GCLs can be considered as a substitute for the absent GCPs and a satisfactory orientation accuracy of better than 1 GSD, almost the same as the one achieved using GCPs, can be achieved.

4 Conclusions

In this paper, using the geometric constraint that an observed line and a projected line in image space are bound to coincide, a line-based orientation model of HRSI is established. On the basis of the point-based and line-based models, a feasible and effective tri-stereo model orientation approach combining GCPs and GCLs is presented. Compared to the line-based orientation models established based on the PSM, the model proposed in this paper is based on the RFM. This means that only the RPCs rather than the satellite's position and attitude observations and sensor parameters are needed for the presented approach. Hence, the presented approach is more convenient and practicable for HRSI users to perform the tri-stereo model orientation combining GCPs and GCLs.

Compared with point features, the control information from linear features can be used even without a complete match between image and object features. That is to say, only the image line needs to correspond with the object line whilst the correspondence between the points on the two lines is not necessary. The experimental results achieved for two ZY-3 datasets have shown that if it is difficult to identify four GCPs in the image corners, GCLs can be employed to substitute for the absent GCPs in the tri-stereo model orientation; more specially, a satisfactory orientation accuracy can be achieved combining three GCPs and one GCL, two GCPs and two GCLs, or one GCP and five GCLs. Additionally, if the control information is obtained from existing topographical maps, it will be feasible to extract GCLs and not to extract GCPs due to the abundant linear features in the topographical maps. In this case, it is possible just to use GCLs as control information for the tri-stereo model orientation, and a satisfactory accuracy can be achieved using eight GCLs evenly distributed near the image boundaries. With respect to the directions of GCLs, in order to restrain the offset and scaling of the ATM effectively and to determine the ATPs and the object coordinates of the tie points precisely, the angles of GCLs should be distributed evenly in at least two out of the four angle ranges, independently of whether the tri-stereo model orientation is performed using only GCLs or combining GCPs and GCLs.

Due to the restriction of HRSI datasets, only two ZY-3 datasets were tested in this paper. The feasibility and effectiveness of the presented orientation approach combining GCPs and GCLs still needs to be validated further using very high resolution satellite images from the newest generation. Besides, the image and object coordinates of the GCPs and GCLs are all measured manually in this paper, which is very time-consuming. Hence, the automation of the presented approach, which can be based on automated point and/or line extraction in both, an existing DOM and the HRSI, followed by a matching stage, needs to be studied further.

Acknowledgement

This work was supported by the national basic research program of China (973 program) (Grant No. 2012CB719902).

References

Fraser, C.S., Hanley, H.B. & Yamakawa, T., 2002: Three-dimensional geopositioning accuracy of IKONOS imagery. – Photogrammetric Record **17** (99): 465–479.

Fraser, C.S. & Hanley, H.B., 2005: Bias-compensated RPCs for sensor orientation of high-resolution satellite imagery. – Photogrammetric Engineering & Remote Sensing **71** (8): 909–915.

Fraser, C.S., Dial, G. & Grodecki, J., 2006: Sensor orientation via RPCs. – ISPRS Journal of Photogrammetry and Remote Sensing **60** (3): 182–194.

Grodecki, J. & Dial, G., 2003: Block adjustment of high-resolution satellite images described by rational polynomials. – Photogrammetric Engineering & Remote Sensing **69** (1): 59–68.

Habib, A.F., Lin, H.T. & Morgan, M.F., 2003: Autonomous space resection using point- and line-based representation of free-form control linear features. – Photogrammetric Record **18** (103): 244–258.

Habib, A.F. & Alruzouq, R.I., 2004: Line-based modified iterated hough transform for automatic registration of multi-source imagery. – Photogrammetric Record **19** (105): 5–21.

Habib, A.F., Morgan, M.F., Kim, E.M. & Cheng, R., 2004: Linear features in photogrammetric activities. – International Archives of Photogrammetry, Remote Sensing and Spatial Information Sciences **35** (B2): 610–615.

Karjalainen, M., Hyyppä, J. & Kuittinen, R., 2006: Determination of exterior orientation using linear features from vector maps. – Photogrammetric Record **21** (116): 329–341.

Marcato Junior, J. & Tommaselli, A.M.G., 2013: Exterior orientation of CBERS-2B imagery using multi-feature control and orbital data. – ISPRS Journal of Photogrammetry and Remote Sensing **79**: 219–225.

Masry, S.E., 1981: Digital mapping using entities: a new concept. – Photogrammetric Engineering & Remote Sensing **47** (11): 1561–1565.

Nagasubramanian, V., Radhadevi, P.V., Ramachandran, R. & Krishnan, R., 2007: Rational function model for sensor orientation of IRS-P6 LISS-4 imagery. – Photogrammetric Record **22** (120): 309–320.

Schenk, T., 2004: From point-based to feature-based aerial triangulation. – ISPRS Journal of Photogrammetric and Remote Sensing **58** (5): 315–329.

Shi, W. & Shaker, A., 2006: The line-based transformation model (LBTM) for image-to-image registration of high-resolution satellite image data. – International Journal of Remote Sensing **27** (14): 3001–3012.

Tao, C.V. & Hu, Y., 2001: A comprehensive study of the rational function model for photogrammetric processing. – Photogrammetric Engineering & Remote Sensing **67** (12): 1347–1357.

Tao, C.V., Hu, Y. & Jiang, W., 2004: Photogrammetric exploitation of IKONOS imagery for mapping applications. – International Journal of Remote Sensing **25** (14): 2833–2853.

Tommaselli, A.M.G. & Medeiros, N.G., 2010: Determination of the indirect orientation of orbital pushbroom images using control straight lines. – Photogrammetric Record **25** (130): 159–179.

Tommaselli, A.M.G. & Marcato Junior, J., 2012: Bundle block adjustment of CBERS-2B HRC imagery combining control points and lines. – PFG – Photogrammetrie, Fernerkundung, Geoinformation **2**: 129–139.

Yuan, X. & Lin, X., 2008: A method for solving rational polynomial coefficients based on ridge estimation. – Geomatics and Information Science of Wuhan University **33** (11): 1130–1133.

Yuan, X. & Liu, X., 2009: A novel matching method for high resolution satellite imagery based on rational function model. – Geomatics and Information Science of Wuhan University **34** (6): 671–674.

Zhang, J., Zhang, H. & Zhang, Z., 2004: Exterior orientation for remote sensing image with high resolution by linear feature. – International Archives of Photogrammetry and Remote Sensing **35** (B3): 76–79.

Zhang, L., Zhang, J., Chen, X. & An, H., 2009: Block-adjustment with SPOT-5 imagery and sparse GCPs based on RFM. – Acta Geodaetica et Cartographica Sinica **38** (4): 302–310.

Zhang, Y., Hu, B. & Zhang, J., 2011: Relative orientation based on multiple conjugate features. – ISPRS Journal of Photogrammetric and Remote Sensing **66** (5): 700–707.

Address of the authors:

Dr. Jinshan Cao, Collaborative Innovation Center of Geospatial Technology, 129 Luoyu Road, Wuhan, China, CN-430079, Tel: +86-27-68771228, Fax: +86-27-68771228, e-mail: caojs@whu.edu.cn

Prof. Dr. Xiuxiao Yuan, School of Remote Sensing and Information Engineering, Wuhan University, 129 Luoyu Road, Wuhan, China, CN-430079, Tel: +86-27-68771228, Fax: +86-27-68771228, e-mail: yuanxx@whu.edu.cn

Dr. Yi Fang, School of Remote Sensing and Information Engineering, Wuhan University, 129 Luoyu Road, Wuhan, China, CN-430079, Tel: +86-27-68771228, Fax: +86-27-68771228, e-mail: fywhu@qq.com

Manuskript eingereicht: Dezember 2015
Angenommen: April 2016

PFG 2016 / 3, 141 – 152
Stuttgart, xxx 2016

Article

Image Quality Assessment of Pléiades-1A Triplet Bundle and Pan-sharpened Images

Karsten Jacobsen, Hannover, Hüseyin Topan, Ali Cam, Mustafa Özendi & Murat Oruc, Zonguldak, Turkey

Keywords: image quality, edge analysis, signal-to-noise ratio, blur coefficient, Pléiades, pan-sharpening

Summary: The image quality of Pléiades-1A panchromatic and multispectral as well as pan-sharpened images has been analyzed. The original images are available with 12 bit radiometric resolution, but for mapping purposes often this is reduced to 8 bit, corresponding to the grey value resolution of the computer screens. Therefore, original images as well as the 8 bit images were investigated. Pléiades images are distributed with 50 cm ground sampling distance (GSD) in spite of the original resolution with 70 cm GSD. For this the effective image quality was determined by edge analysis. The edge analysis can be influenced by image sharpening. An image sharpening usually enlarges the image noise, which however can be reduced by filtering. This can influence the presentation of small image details, so in addition to edge and noise analysis image details in the Pléiades images were compared with the details visible in satellite images taken by other sensors having similar ground resolution. A blur analysis did not improve the information about image quality. In the Zonguldak test site (Turkey) Pléiades images are compared with WorldView-1-, QuickBird- and IKONOS-images. The zooming from 70 cm to 50 cm GSD could not be identified by the investigation of the Pléiades image quality. It leads to an even better quality than of the WorldView-1- and QuickBird images with an originally higher resolution.

Zusammenfassung: *Bildqualität von Triplet Bundle und Pan-sharpened Bildern des Systems Pléiades-1A*. Die Bildqualität von panchromatischen, multispektralen und pan-geschärften Pléiades-1A Bildern wurde untersucht. Die Originalbilder haben eine radiometrische Auflösung von 12 bit, für die Kartenerstellung werden sie jedoch häufig auf 8 bit reduziert, weswegen sowohl die Originalbilder als auch 8-bit-Bilder analysiert wurden. Pléiades-Bilder werden mit 50 cm Objektpixelgröße ausgeliefert, obwohl die geometrische Auflösung nur 70 cm beträgt. Aus diesem Grund war eine Untersuchung der Bildqualität mittels Kantenanalyse erforderlich. Die Kantenanalyse kann durch Bildschärfung beeinflusst werden. Dieses erhöht normalerweise das Bildrauschen. Das Bildrauschen lässt sich durch Filterung reduzieren, was wiederum die Erkennbarkeit kleiner Bilddetails verschlechtern kann. Aus diesem Grund wurde auch das Bildrauschen untersucht. Eine blur-Untersuchung verbesserte die Information über die Bildqualität nicht. Von dem Testgebiet Zonguldak, Türkei, sind auch WorldView-1-, QuickBird- und IKONOS-Bilder vorhanden, die einen Vergleich von Bilddetails ermöglichen. Die Vergrößerung der Pléiades-Bilder von 70 cm auf 50 cm Objektpixelgröße konnte nicht durch eine reduzierte Bildqualität nachgewiesen werden. Vielmehr waren die Pléiades-Bilder sogar qualitativ besser als die WorldView-1- und die QuickBird-Bilder, die eine höhere geometrische Auflösung besitzen.

1 Introduction

Optical satellite images are commonly used for photogrammetric application. Based on experience with images from some optical satellites it is necessary to analyze the image quality because it may not correspond to the image specification as it is the case especially for systems equipped with staggered CCD-lines for example OrbView-3 images (Topan et al. 2009). Pléiades images are distributed with 50 cm ground sampling distance (GSD) in spite of the geometric resolution with 70 cm GSD in nadir images. Such a zooming effect

www.schweizerbart.de
DOI: 10.1127/pfg/2016/0291
1432-8364/16/0291 $ 3.25

should be seen by edge analysis, but edges can be influenced by image sharpening. The image sharpening should enlarge the image noise, but this again can be influenced by filtering. Airbus DS announces that Pléiades images are enhanced by de-convolution and denoised, so the effective image resolution as well as the signal-to-noise ratio (SNR) may be influenced. This procedure may reduce the imaging of small details, requiring a comparison with satellite images of similar resolution.

Topographic mapping, today realized by data acquisition for GIS (Geographic Information Systems), is usually based on digitizing colour images. Very high resolution satellite colour images use the fusion of lower resolution multispectral with higher resolution panchromatic images by pan-sharpening. This complicates the image quality, so also pansharpened images were investigated.

This publication contributes to the investigation of effective image quality, being important for mapping. The influence of the Pléiades image enlargement from 70 cm geometric resolution to the distributed 50 cm GSD is analysed. Therefore, edge and blur analysis supported by noise analysis and a comparison of satellite images with similar ground resolution is conducted. Such complete investigation of Pléiades image products is missing up to now.

2 Related Investigations

The modulation transfer function (MTF) is frequently used to estimate the spatial quality of imaging systems. It can be based on artificial targets or clear edges. First operational investigations of image quality have been done by Koelbl (Koelbl & Hawawini 1986, Koelbl 2005). The Federation of American Scientists (FAS) developed the National Image Interpretability Rating Scales (NIIRS), at first for military reconnaissance, but with the Civil NIIRS Reference Guide (NIIRS 1996) also for civilian applications. The NIIRS values can be determined by interpretation of image analysts to quantify images into 10 steps from NIIRS 0 (over 9.0 m GSD) up to NIIRS 9 (less than 0.10 m GSD) (Leachtenauer 1996). The level NIIRS 6 corresponds to 0.40 m up to 0.75 m GSD. The NIIRS values can be determined visually by image analysts, which is not very accurate and by the given rules not usable outside the United States, but as an alternative it can be based on a general image quality equation. The formula as a function of the GSD, an edge analysis and the signal-to-noise ratio have a clear background. Nevertheless, the NIIRS values are an artificial quality scale. Furthermore, they are mixing the results of the edge analysis with the noise and the nominal GSD.

Kim & Kim (2011) are using the Ground Resolvable Distance (GRD) for the description of the image quality. GRD is the minimal distance between two objects to be identified as separate, corresponding to the classical bar code targets used for analog images. They started with the analysis of bar code targets, but they adapted it to edges using the same definition of the effective ground resolution described below. Nevertheless, there is a discrepancy between the original definition of the GRD and the GRD based on the line spread function.

Based on the investigation of Koelbl (2005), Jacobsen (2008) and Passini & Jacobsen (2008) introduced for digital images the standard deviation of edge spread functions of clear image edges is a factor for effective resolution. Such edges are visible in the images e.g. at building roofs, parking places or straight streets. The factor for effective resolution multiplied with the nominal GSD leads to the effective GSD describing the image quality in a simple manner having a real meaning. The effective resolution is determined by edges with a satisfying length of approximately 20 to 100 pixels. The average grey value profile of all profiles perpendicular to the edge in every pixel distance is used for the analysis for reducing the influence of noise and the influence of the sampling step width. The Gaussian curve is adjusted into a differentiated grey value profile for the determination of the standard deviation of the Gaussian function being the factor for effective resolution (Fig. 3). The factor for effective resolution multiplied with the GSD is the effective GSD. The factor for effective GSD is invariant against orientation of the edges. Under usual condition the factor for effective resolution should be close to 1.0. This is not the case for images from staggered

sensors. Staggered sensors have two CCD-lines shifted half a pixel against each other and thus improving the nominal ground resolution with factor two by mixing the images of the two CCD-lines. Topan et al. (2009) and Jacobsen (2011) determined the factor for effective resolution for staggered sensors in the range of approximately 1.1 up to 1.25, what is still better as the factor 2.0 for the original size of the individual pixels, but clearly above 1.0 for images with a pixel size of half the staggered width.

In computer vision another method of radiometric quality assessment is proposed by Crété-Roffet et al. (2007). They compared the original image with the image smoothed by an average filter separately applied in horizontal and in vertical direction. By comparison of the normalized grey value differences of neighboured pixels a blur coefficient is computed. For example Alsadik et al. (2015) used it for the identification of images with satisfying quality.

3 Dataset

A triplet of Pléiades images has been taken from the same orbit at April 24th, 2013 over the area around the city of Zonguldak, Turkey (Tab. 1). The test area includes the city which is situated partly in a mountainous location and its surrounding area with mountainous forest and a small percentage of agriculture.

Distributed Pléiades images are resampled from 70 cm to 50 cm for panchromatic band, and from 2.8 m to 2 m for multispectral bands. The original radiometric resolution is 12 bit. The images are de-convoluted for enhancing the image sharpness and de-noised. As mentioned above, the effects of this process should be visible by edge and noise analysis.

According to the Pléiades Imagery User Guide (2012) Pléiades images are improved by "inter-detector equalization: with correction of differences in sensitivity between the detectors (on board correction), aberrant detectors correction (if any), panchromatic band is restored and de-noised, and improved by pixel sampling at Shannon optimizing image quality for downstream value-added processing with spline kernel resampling into the primary geometry, zoomed to the factor 7/5 (equivalent resolution of 0.5 m respectively 2 m in nadir condition)".

The signal-to-noise ratio depends upon the size of the signal, represented by the histogram. Even if the images shall have 12 bit resolution, corresponding to 4096 grey values, in none of the used channel more as 0.01% of the grey values are exceeding the value 2047 and, with the exception of the near infrared (NIR) band, only up to 3% of the grey values are exceeding the digital number 1024 (Fig. 2). The histograms of the multispectral bands are similar for all used images, only the panchromatic band shows larger variations.

Tab. 1: Pléiades image specification.

Image ID	284	269	283
Viewing angles			
Across track	4.2°	4.5°	4.8°
Along track	10.1°	4.5°	-1.2°
Incidence angle	12.3°	7.2°	5.5°
Average original GSD	72 cm	71 cm	70 cm

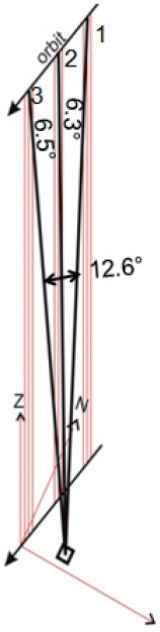

Fig. 1: Imaging configuration of Pléiades triplet in Zonguldak test area.

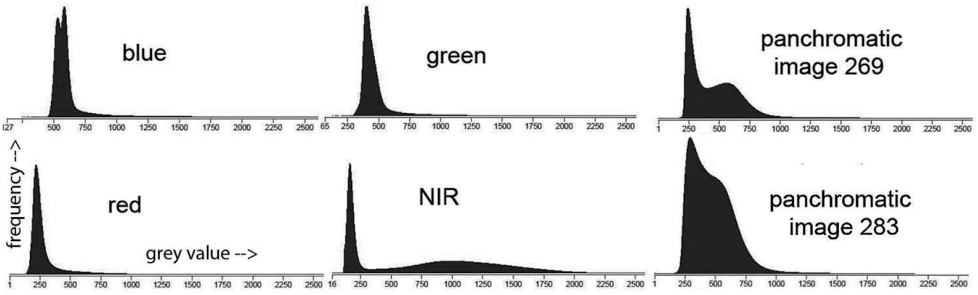

Fig. 2: Typical histograms of Pléiades 16 bit image in test field Zonguldak for grey values up to 2600.

4 Radiometric Quality Assessment

4.1 Edge Analysis

The image acquired by optical sensors never present the recorded radiation perfectly. The wave structure of the light causes some limitations especially by the fact that the small angle satellite images are not far away from diaphragm limited resolution. Details are blurred which can be characterized by the Point Spread Function (*PSF*) (Koelbl 2005). The total *PSF* contains sub-types as the optical *PSF* (PSF_{opt}), image motion *PSF* (PSF_{im}), detector *PSF* (PSF_{det}) and electronics *PSF* (PSF_{el}). PSF_{opt} is an expected phenomenon because of the wave structure of the light. In pushbroom systems, the integration time causes in-track blurring. The PSF_{im} is expressed by the following equation:

$$PSF_{im}(x,y) = rect\left(\frac{y}{S}\right) \quad (1)$$

where x, y are the row and column coordinates respectively in image space, $S = platform\ velocity$ imaging time and *rect* refers to rectangular function.

The imaging time has to respect the influence of time delay and integration (TDI) sensors, shifting the charge from one CCD-line to the neighboured corresponding to the image motion, influencing the effective imaging time, but there is also an influence caused by the TDI (PSF_{tdi}). If the sensor has a non-zero spatial area of each detector, this causes a spatial blurring called PSF_{det}. PSF_{el} is a result of electronical filtering the detector signal to reduce the noise. The effect of this filtering on cross-track images is very smooth (Schowengerdt 1997). The *PSF* with respect to the atmosphere should also be considered (PSF_{atm}) (Javan et al. 2013). As a sum of all *PSFs*, the total *PSF* is denoted as following (2):

The similar phenomenon can occur at line-based objects as Line Spread Function (LSF). In other words, a sharp line in object space is shown spreading into a few adjacent lines. Fig. 3 illustrates the relation between an edge in the image, the grey value profile at an edge and the corresponding LSF. The edge in object space is sharp, while the grey value profile in the image shows a continuous change from dark to bright (Fig. 3, centre right). A differentiation of the grey value profile results in the LSF – see Fig. 3, right. It is worthwhile to mention that the analysis of optical images using LSF is operational, while the use of the PSF for real images is more theoretical (Javan et al. 2013).

The factor for effective GSD can be estimated based on LSF. This value is estimated via satisfying long and sharp line features in object space as edges of roofs or shadows (Fig. 3, left) resulting in image space as shown in Fig. 3, 2nd from left. All grey value profiles perpendicular to the edge, from start to end, in one pixel distance are averaged to reduce the influence of noise and the influence of sampling. The length of the profiles has to be satisfying for the determination of the LSF, but it should not be too long to avoid a nega-

$$PSF = PSF_{opt} \cdot PSF_{im} \cdot PSF_{det} \cdot PSF_{el} \cdot PSF_{atm} \cdot PSF_{tdi} \quad (2)$$

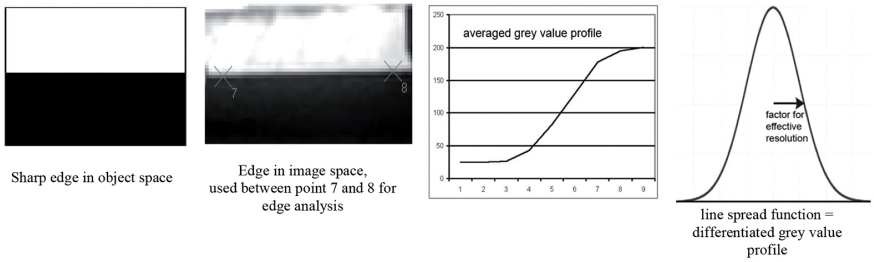

Fig. 3: Estimation of factor for effective resolution.

tive influence by changing grey values across edge direction. Fig. 3, 3rd from left, shows an averaged grey value profile of an edge over 9 pixels, being satisfying for the investigation. The differentiation of the averaged grey value profile leads to the Gaussian-shaped LSF. In the used program the Gaussian shape is adjusted into the differentiated averaged grey value profile. The width of the Gaussian function (Fig. 3, right), corresponding to 1σ is the factor for the effective resolution. This factor multiplied with the nominal GSD leads to the effective GSD.

For most of the very high resolution space images the factor for effective resolution is close to 1.0, meaning that the effective GSD is nearly the same as the nominal GSD. This is not the case for images from staggered sensors. For SPOT 5 Supermode for instance the factor is 1.18, corresponding to an effective GSD of 2.5 m × 1.18 = 3.0 m instead of the nominal 2.5 m GSD and the geometric 5.0 m GSD. For IRS-1C, OrbView-3, Resourcesat and Cartosat 1 the factor for effective resolution is between 1.12 and 1.2 (Jacobsen 2011).

The effective GSD of original and pan-sharpened Pléiades images were determined. To avoid the effect of directional position of edges, edges in different directions have been analysed. No correlation between the size of the factor for effective resolution and the edge direction as well as the edge location could be seen.

The investigated pan-sharpened images were generated by modified Brovey-transformation (3,4) (Jacobsen 2011). The transformation accounts for the misfit of the spectral range of red, green and blue bands in relation to the panchromatic band, which includes also parts of NIR, by subtracting NIR-grey values partially from the panchromatic band (formulas 3 and 4). The colour pixels have been interpolated bilinearly to avoid staircase edges.

DN_b, DN_g, DN_r, DN_{nir}, and DN_{pan} are digital numbers of grey values for the different bands with F as a free factor for respecting the influence of NIR to the panchromatic band and MF as a correction factor for the brightness, F and MF may be different for any of the output colour bands.

The modified Brovey-transformation has the advantage of enabling optimal conditions for mapping. This is not the same as keeping the radiometric behaviour of the colour bands.

Even though Pléiades images with 50 cm, respectively 200 cm GSD, instead of the original 70 cm, respectively 280 cm GSD, have been used for the determination of the factors for the effective resolution, only for the average of the NIR-bands the factor for ef-

$$DN_{fused} = \frac{DN_b \cdot 3}{DN_b + DN_g + DN_r} \cdot DN_{pan} \cdot MF \qquad \text{(3) Brovey-transformation}$$

$$DN_{fused} = \frac{DN_b \cdot 3}{DN_b + DN_g + DN_r} \cdot \frac{DN_{pan} - F \cdot \frac{DN_{nir}}{3}}{1 - F/3} \cdot MF \qquad \text{(4) Modified Brovey-transformation}$$

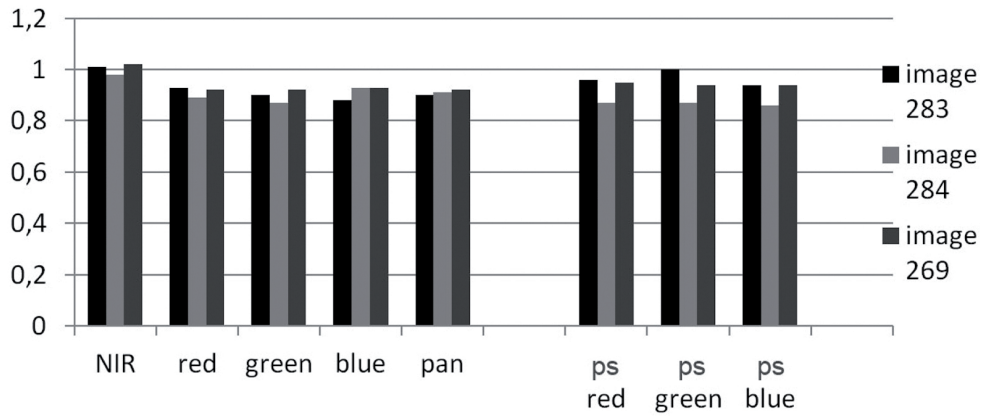

Fig. 4: Factors for effective resolution of Pléiades triplet images of the Zonguldak test area.

fective resolution is 1.00. For the other bands it is smaller corresponding to an even higher effective resolution as 50 cm respectively 200 cm GSD (Fig. 4).

By simple theory the factors for the effective resolution should be 70 cm / 50 cm = 1.4, but as mentioned by Airbus DS (Pléiades Imagery User Guide 2012) the images are enhanced by de-convolution, influencing directly the LSF. Image sharpening reduces the grey values just in front of the edge in the dark part (in Fig. 5, lower left, shown by the dark line in the strongly sharpened image) and enlarges the grey values at the bright part. The grey value profile of an original Pléiades image in Fig. 5 shows a small reduction of the grey values in the darker part. For a demonstration of this effect a stronger image sharpening was applied (Fig. 5, right) and the grey values of the profile have been overlaid to the profile of the original image. The grey value profile in Fig. 5 right shows also the changed steepness of the profile by sharpening. The steepness of the profile determines the width of the LSF and so the factor for effective image resolution.

4.2 *Blur Coefficient*

Crété-Roffet et al. (2007) developed another method of radiometric quality assessment. By comparing the original image with the image smoothed by an average filter in horizontal

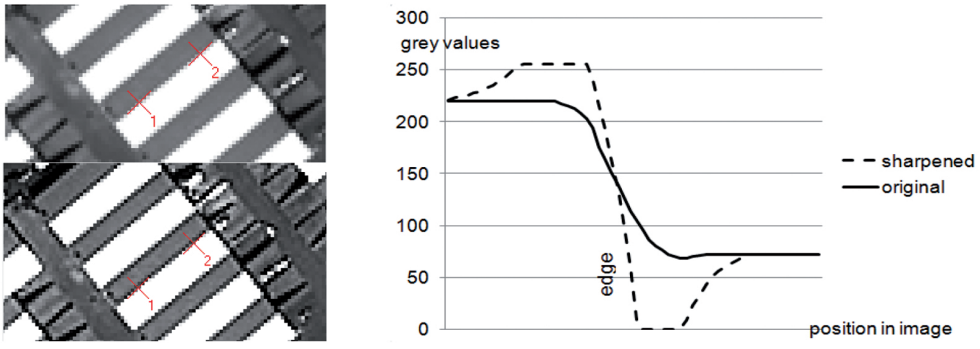

Fig. 5: Effect of strong image sharpening at edge. Selected edge – from 1 to 2. Upper left: original Pléiades image; Lower left: strongly sharpened image; Right: averaged grey value profiles perpendicular to edge 1 to 2.

and separately in vertical direction. By comparison of normalized grey value differences of neighboured pixels a blur coefficient is computed. As common, a filter length of 9 pixels was used. Original sharp images shall have larger blur coefficients as not sharp images. Some space images, analog aerial images, and small digital camera images mounted on a remotely piloted airborne system (RPAS) (same as UAV or UAS) were used for the comparison of image quality parameters. Fig. 6 shows the factor for effective resolution, determined by edge analysis, in ascending sequence together with the blur coefficient and also the SNR. The factor for effective resolution has been shown as a reasonable tool for the determination of the image quality (Jacobsen 2011), confirmed by visual check, and has a real meaning. For the panchromatic channel of the Pléiades triplet blur coefficients of 0.46, 0.39, and 0.41 have been achieved for a filter length of 9 pixels, indicating a satisfying image quality. The blur coefficients as shown in Fig. 6 have no correlation with the effective resolution and the visual image quality. With a value of 0.31, the blur coefficients have regarding some poor images from an RPAS camera correctly a smaller value as for most of the listed space images, but good for IKONOS and WorldView-2 images with a factor because the effective resolution of 0.8 and smaller has even smaller blur coefficients. That means, that the blur coefficient propagated in computer vision is not a reliable figure for the quality of space and aerial images.

4.3 *Signal-to-Noise Ratio*

The image sharpening can enlarge the image noise, so the analysis for the images was completed by the determination of the image noise or better the signal-to-noise ratio (SNR). The SNR depends upon the size of the signal, so it should be and was determined separately for groups of grey values. The weighted averages in Figs. 7 and 8 are weighted for the number of grey values where the individual values appear. The colour bands have been analysed with the available GSD of 2 m, all the other images with 50 cm GSD.

The colour bands with the exception of NIR have a smaller, nevertheless satisfying SNR. For the panchromatic band the SNR has the highest values and for the pan-sharpened bands it is between the values for colour and panchromatic bands.

The SNR is not indicating a higher noise as in other comparable space images such as Kompsat-1, IKONOS, QuickBird, OrbView-3, Resourcesat, WorldView-1, and GeoEye-1 (Jacobsen 2011) which may be caused by the de-noising of Pléiades images. The noise for 8 bit images for the panchromatic band is in the range of 1.2 grey values, for colour bands in the range of 2.3, for 16 bit images for the

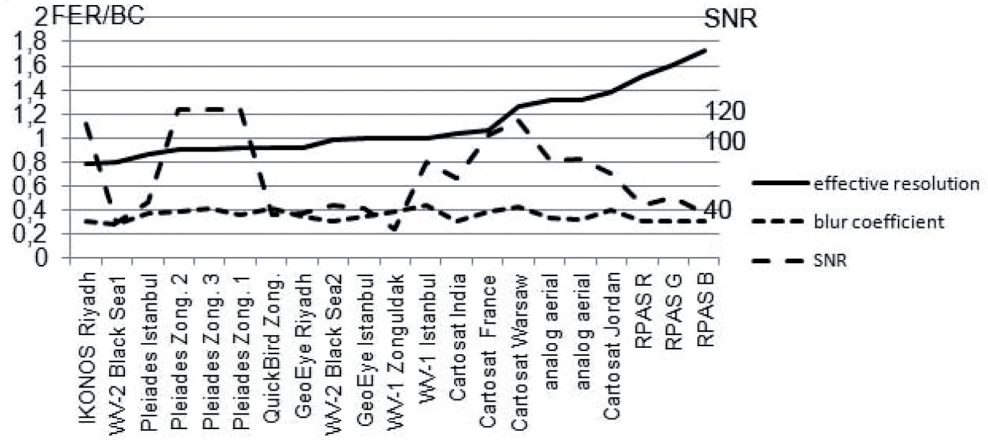

Fig. 6: Factor for effective resolution (FER), blur coefficient (BC), signal-to-noise ratio of some space and aerial images; with exception of RPAS images for the panchromatic channel.

panchromatic band in the range of 5, and for the colour bands between 8 and 11 grey values. These are not critical values and they appear in similar quantities in other space images (Fig. 6).

5 Comparison with other Space Images

Pléiades images are de-noised, improving the SNR, but this may eliminate small image details. For assessing such effects a comparison with other space images having similar ground resolution was conducted. In the test area Zonguldak also images from WorldView-1, QuickBird and IKONOS are available (Tab. 2). As it can be seen in Tab. 2, the sun elevation of imaging differs, but it is between 49.7° and 67.2° being not too different. Differences are caused by the incidence angle – the nadir angle from ground to satellite – enlarging the average GSD of the WorldView-1-image from 48 cm at nadir view to 56 cm in the used image.

In Fig. 10 sub-areas of pan-sharpened images are shown. For better visualization of the images in the publication, the sub-images are shown brighter as for photogrammetric applications. In addition the images have been sharpened to improve the identification of small details in the publication important for

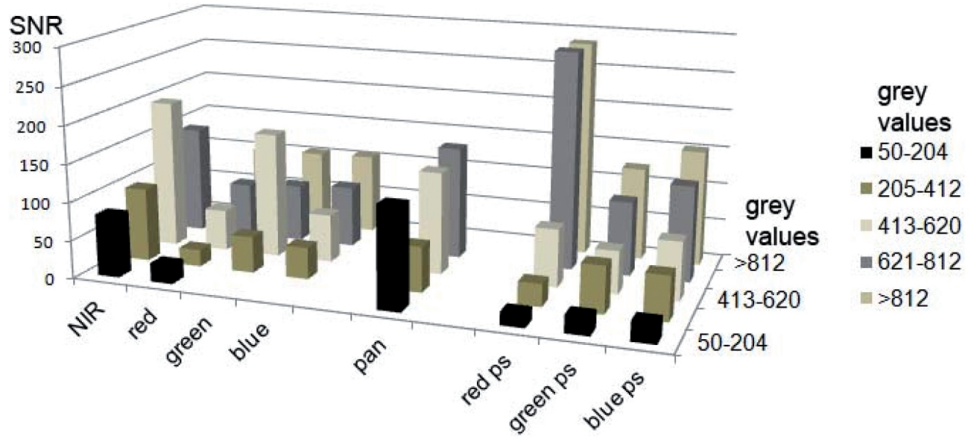

Fig. 7: Signal-to-noise ratio for 16 bit Pléiades images separately for different grey value groups (average of 3 images) in test area Zonguldak, ps = pan-sharpened.

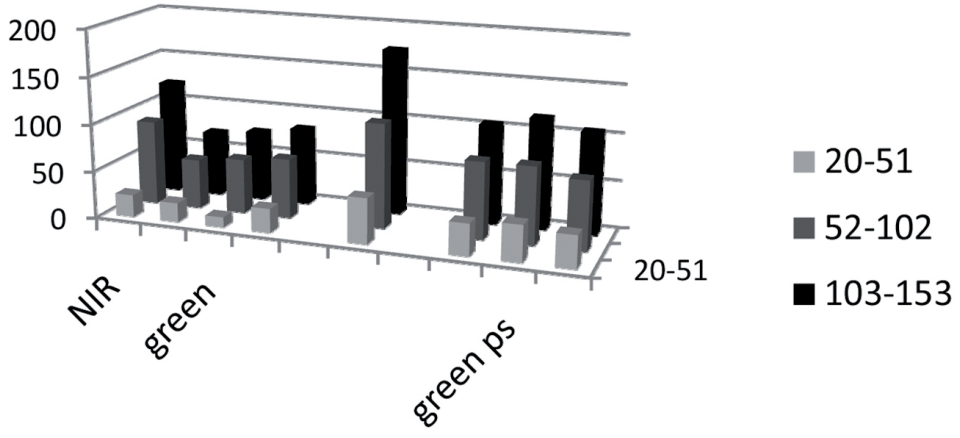

Fig. 8: Signal-to-noise ratio for 8 bit Pléiades images separately for different grey value groups (average of 3 images) in test area Zonguldak, ps = pan-sharpened.

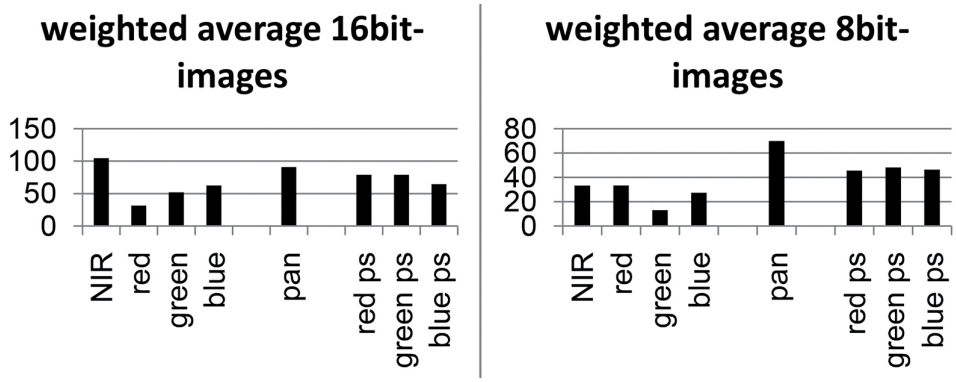

Fig. 9: Weighted average of SNR for 16 bit- and 8 bit-Pléiades images in test area Zonguldak, ps = pan-sharpened.

a better comparison by the reader. All images have been improved in same manner. Nevertheless, the sharpening was not required for the Pléiades image.

As usual, all investigated images have few blooming effects caused by direct reflection of sun light e.g. by glass roofs, but this typical effect of all digital images is not disturbing too much.

With the exception of Pléiades, the factors for the effective resolution (Tab. 3) are nearly 1.0, meaning that the effective resolution is identical to the nominal resolution. For Pléiades, however, the lower factor corresponds to an effective GSD of 50 cm x 0.91 = 46 cm, clearly below the geometric resolution of 70 cm. As mentioned before, Pléiades images have been enhanced by de-convolution and de-noised by Airbus DS. These results achieved in the test area Zonguldak are typical for the used space images. They agree with the factors for effective resolution published in Jacobsen (2011) and are also an average of several images, and, in addition, unpublished investigations of the author. Also for other satellite image types the root-mean-square variation of the factors is in the range of 0.05.

The SNR for the important panchromatic band (Tab. 4) for Pléiades and IKONOS is on a similar level, whilst WorldView-1 and QuickBird have a slightly lower quality. For the colour bands (Tab. 5) it is a little mixed – in general, the red band is not as good, while the other bands for all three colour images are not too diverse. But the noise in the colour bands is not as important. Finally, no disadvantages of the Pléiades images caused by image sharpening through Airbus DS can be seen. This may be caused by the de-noising of the Pléiades images. Thus, the last step has to be the comparison of image details since de-noising may cause a low-pass filtering leading to a loss of details.

Especially, the identification of small details was checked by a comparison of the images in the test area Zonguldak (Fig. 10). The comparison of Pléiades with WorldView-1 images has to respect the missing colour information of WorldView-1. Nevertheless, the details can be better identified in the Pléiades images even if it is based on the original 70 cm GSD. Also, the QuickBird image has disadvantages against Pléiades. IKONOS has also a very good radiometric quality as Pléiades, but with 100 cm GSD the resolution is clearly below Pléiades, and this can be seen. The visual image quality of the images shown in Fig. 10 agrees with the same image types used in other investigations (Topan et al. 2009) and additional internal tests by the authors.

6 Conclusion

Pléiades-1A triplet bundle images over Zonguldak test area have been investigated with respect to the image quality. Pléiades images are distributed with 0.5 m respectively 2.0 m GSD even if the original resolution is only 0.7 m GSD for panchromatic images and 2.8 m

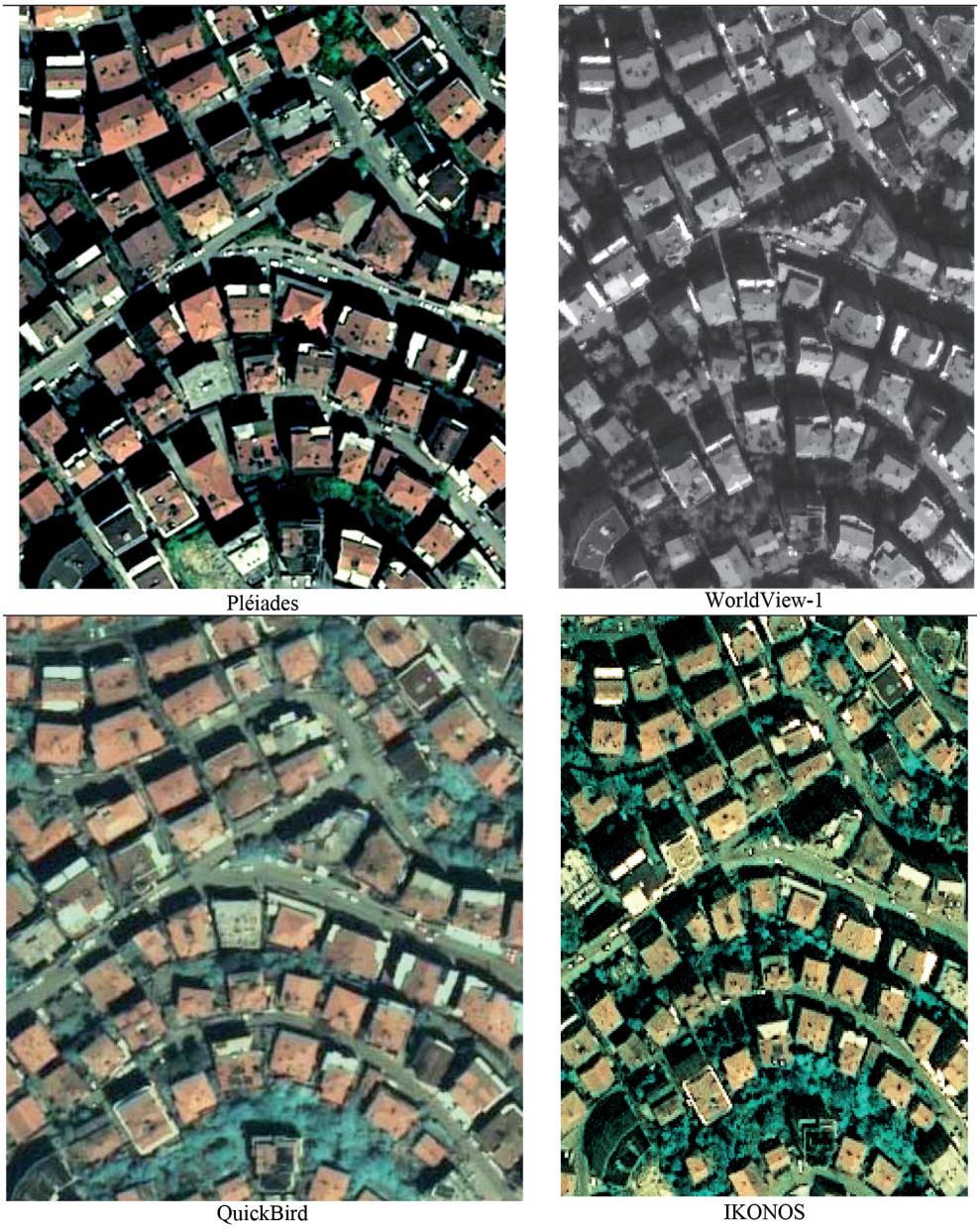

Fig. 10: Sub-areas of pan-sharpened images from Pléiades, WorldView-1, QuickBird, and IKONOS.

for the colour bands. Pléiades images are enhanced by de-convolution and are de-noised. For the enlarged images with 0.5 m GSD, this enhancement leads to satisfying factors for effective image resolution and also no-enlargement of the SNR can be seen. Also, a comparison with a WorldView-1-image having 56 cm GSD and a QuickBird-image with 62 cm GSD does not indicate the zooming from 70 cm to 50 cm GSD. The used Pléiades scenes have better image quality as compared images from WorldView-1 and QuickBird with higher orig-

Tab. 2: Compared satellite images in the test area Zonguldak.

Satellite	Imaging	Sun elevation	Incidence angle	GSD of delivered images	Geometric GSD
Pléiades 1A	2013-04-24	59.2°	12.3° / 7.2° / 5.8°	50 cm	70 cm
WorldView-1	2008-09-16	49.7°	28.6°	56 cm	56 cm
QuickBird	2004-05-23	64.7°	3.9°	62 cm	62 cm
IKONOS	2002-07-02	67.2°	20.3°	100 cm	89 cm

Tab. 3: Factors for effective resolution of panchromatic channels in the test area Zonguldak.

Pléiades 1A (average)	WorldView-1	QuickBird	IKONOS
0.91	1.02	1.01	1.02

Tab. 4: SNR of the panchromatic channels of the different satellite imagery in the test area Zonguldak.

SNR	Pléiades (average)	WorldView-1	QuickBird	IKONOS
16 bit	91	24	48	98
8 bit	70	36	32	30

Tab. 5: SNR of the colour channels of Pléiades, IKONOS and QuickBird imagery in test area Zonguldak.

SNR	Pléiades colour channels (average of 3 images)				QuickBird colour channels				IKONOS colour channels			
	blue	green	red	NIR	blue	green	red	NIR	blue	green	red	NIR
16 bit	62	52	31	105	72	98	50	50	109	70	43	111
8 bit	27	13	33	33	72	130	50	37	55	40	13	24

inal resolution, justifying the distribution of Pléiades images with 50 cm respectively 2.0 m GSD. This has been confirmed by other internal investigations. Of course a comparison with IKONOS shows clearly the influence of the lower resolution of IKONOS images. The SNR of Pléiades images is satisfying and even better as for most other investigated space images. The blur coefficient has not been shown as a reliable number for specifying the image quality.

Acknowledgements

The Pléiades-1A triplet bundle images was supported by the MyGIC program of Airbus Defence and Space, and this study was supported by the Scientific Research Projects of Bülent Ecevit University (Project ID: 2014-47912266-01) and TÜBİTAK (Project ID: 114Y380).

References

Alsadik, B., Gerke, M. & Vosselman, G., 2015: Efficient use of video for 3D modeling of culture heritage objects. – ISPRS Photogrammetric Image Analysis (PIA) 15 + High resolution earth imaging for geospatial information (HRIGI) 15 workshop Munich, International Annals of Photogrammetry, Remote Sensing and Spatial Information Science **II-3/W4,** 2015.

Crété-Roffet, F., Dolmiere, T., Ladret, P. & Nicolas, M., 2007: The Blur Effect: Perception and Estimation with a New No-Reference Perceptual Blur Metric. – SPIE Electronic Imaging Symposium, Human Vision and Electronic Imaging, San Jose, CA, USA.

Jacobsen, K., 2008: Sagt die Anzahl der Pixel im Bild alles? – DGPF annual meeting 2008, Oldenburg.

Jacobsen, K., 2011: Characteristics of very High Resolution Optical Satellites for Topographic Mapping. – ISPRS Hannover Workshop 2011, International Archives of Photogrammetry, Remote Sensing and Spatial Information Science **XXXVIII-4/W19:** 6 p.

Javan, F., Samadzadegan, F. & Reinartz, P., 2013: Spatial Quality Assessment of Pan-Sharpened High Resolution Satellite Imagery Based on an Automatically Estimated Edge Based Metric. – Remote Sensing 5: 6539–6559.

Kim, T. & Kim, J., 2011: Automated assessment of NIIRS and GRD of high resolution satellite images through edge profile analysis of natural tagets. – JACIE 2011 Commercial Imagery Workshop.

Koelbl, O. & Hawawini, J., 1986: Determination of the Modulation Transfer Function for Aerial Cameras under Flight Conditions. – International Symposium of ISPRS Commission I "Progress in Imaging Sensors", 565–572, Stuttgart.

Koelbl, O., 2005: Transfer Functions in Image Data Collection. – Photogrammetric Week 2005.

Leachtenauer, J.C., 1996: National Imagery Interpretability Rating Scales Overview and Product Description ASPRS/ACSM Annual Convention, 262–272.

Passini, R. & Jacobsen, K., 2008: Geometric and radiometric property of large size digital aerial frame cameras. – Civil Commercial Imagery Evaluation Workshop JACIE 2008, Fairfax, VA, USA.

Pléiades Imagery User Guide, 2012: V 2.0 ed., http://www.geo-airbusds.com/en/4572-Pléiades-technical-documents (18.3.2016).

Schowengerdt, R.A., 1997. Remote Sensing, Models and Methods for Image Processing. – Second edition, Academic Press, PA, USA.

Topan, H., Maktav, D., Jacobsen, K. & Buyuksalih, G., 2009: Information content of optical satellite images for topographic mapping. – International Journal of Remote Sensing **30:** 1819–1827.

Addresses of the Authors:

Dr.-Ing. Karsten Jacobsen, Leibniz Universität Hannover, Institut für Photogrammetrie und Geoinformation, D-30167 Hannover, Nienburger Str. 1, Tel.: +49-511-762-2485, Fax: +49-511-62-2483, e-mail: jacobsen@ipi.uni-hannover.de

Prof. Dr. Hüseyin Topan, Ali Cam, Mustafa Özendi & Murat Oruc, Department of Geomatics Engineering, Engineering Faculty, Bülent Ecevit University, 67100 Zonguldak, Turkey, email: topan@beun.edu.tr, alicam193@gmail.com, mozendi@gmail.com, orucm@hotmail.com

Manuskript eingereicht: Juli 2015
Angenommen: Februar 2016

PFG 2016 / 3, 153 – 165
Stuttgart, June 2016

Report

Survey Accuracy Analysis of a Hand-held Mobile LiDAR Device for Cultural Heritage Documentation

Ting On Chan, Derek D. Lichti, Calgary, Canada, David Belton, Bernhard Klingseisen & Petra Helmholz, Perth, Australia

Keywords: Zebedee, LiDAR, accuracy, fitting, geometric features

Summary: In this paper, the survey accuracy of a hand-held, GNSS-free mobile LiDAR device, the Zebedee, is studied by collecting measurements of several different geometric features in four different datasets. We use a new comprehensive accuracy assessment methodology based on geometric modelling which involves a geometric model of a prism/pyramid for square structure. The point cloud accuracies of the features (planes, cylinders, catenaries, prisms and pyramids) were compared to that of a conventional survey-grade LiDAR system, the Leica ScanStation C10. The results suggested that the Zebedee accuracy is very comparable to the C10. For instance, the mean RMS error of plane fittings for the Zebedee is approximately 1.1 cm versus 0.6 cm for the C10. The estimated cylinder radii between the Zebedee and the C10 has only 1.4% difference in average, while the radii difference in prism/pyramid fitting is only 0.8%. As a result, the Zebedee LiDAR device is suitable for heritage mapping not only because it has high operation flexibility but also desired high accuracy.

Zusammenfassung: *Genauigkeitsanalyse eines tragbaren Laserscanners für die archäologische Dokumentation*. Diese Veröffentlichung untersucht die Vermessungsgenauigkeit des tragbaren und ohne GNSS operierenden Laserscanners Zebedee unter Verwendung von geometrischen Objekten in vier verschiedenen Datensätzen. Die umfassende Bewertung der Genauigkeit basiert auf geometrischen Objekten, welche in der Punktwolke modelliert werden und Ebenen, Zylinder, gekrümmte Oberflächen, Prismen und Pyramiden einschließen. Die geometrischen Objekte werden mit Objekten verglichen, welche basierend auf Punktwolken von einem konventionellen vermessungsüblichen LiDAR System, der Leica ScanStation C10, modelliert wurden. Die Resultate zeigen, dass die Genauigkeit des Zebedee mit der des C10 vergleichbar ist. Zum Beispiel beträgt die kleinste Verbesserung für Ebenen (RMS) 1,1 cm gegenüber 0,6 cm vom C10. Die geschätzten Zylinderradien unterscheiden sich zwischen dem Zebedee und dem C10 im Durchschnitt nur um 1,4%. Der kleinste Radiusunterschied beim Prisma-/Pyramidenvergleich beträgt nur 0,8%. Daraus ist zu schließen, dass der Zebedee Laserscanner für die Dokumentation von denkmalgeschützten Gebäuden und Objekten geeignet ist, nicht nur basierend auf der höchst flexiblen Art der Anwendung, sondern auch von der Genauigkeitsbetrachtung her.

1 Introduction

Terrestrial mobile light detection and ranging (LiDAR) systems can be used to collect large point cloud datasets along with trajectories of the system (Kukko et al. 2012). Conventionally, the point clouds collected by the systems at every epoch are directly geo-referenced to a local mapping frame by using the spatial information obtained from the integration of a global navigation satellite system (GNSS) and an inertial navigation system (INS). In order to perform mobile mapping when GNSS signals are not available, or in harsh environments, GNSS-free scanning systems based on the principle of simultaneous localization and mapping (SLAM; Chow et al. 2014) were introduced in recent years, e.g. Bosse et al. (2012), Alismail et al. (2014), Vosselman (2014), Zhang & Singh (2014). Such systems

www.schweizerbart.de
DOI: 10.1127/pfg/2016/0294
1432-8364/16/0294 $ 3.25

are particularly useful for cultural heritage or archaeological documentation since they are independent of the GNSS signals and also mostly compact and light, so users can carry the system to scan areas inaccessible to large vehicles. However, other than the manufacturers' own reports for such systems, very few research papers, e.g. Thomson et al. (2013), focus on the evaluation of the resultant point cloud accuracy or the associated evaluation methods even though this is indeed often important for cultural heritage documentation. For instance, the captured point clouds often have to meet certain accuracy requirements that, depending on the type of object, can range from 5 mm to several centimetres. Where built structures with detailed ornamental features or surface textures are to be recorded, sub-centimetre accuracies are required. For features with a natural surface such as caves or stone walls, where it is important to record the overall dimensions rather than fine details, accuracies of up to 3 cm may be acceptable. In this paper, the point cloud accuracy of a hand-held spring-mounted mobile LiDAR system, the Zebedee (Bosse et al. 2012, Bosse & Zlot 2013) is assessed by a geometric modelling methodology. Rather than primarily using plane fitting accuracy as an indicator to evaluate the Zebedee system (Thomson et al. 2013), this work provides a more comprehensive study of the scanning accuracy through evaluating the fitting accuracy of geometric models of several common primitives including planes, cylinders, catenaries, and square prisms/pyramids. Using different geometric primitives for accuracy evaluation is advantageous over using artificial target points for several reasons: (1) higher data redundancy is obtained; (2) point intensity is not needed; (3) less labour cost is involved; (4) in situ accuracy evaluation is allowed. The accuracy obtained for the same features captured by a static terrestrial LiDAR is used as the reference. The accuracy of the Zebedee is studied as the device has been widely used for cultural heritage documentation (CSIRO 2015); it was used to scan the Leaning Tower of Pisa in Italy (Engineering & Technology 2013) and various caves in Australia (Zlot & Bosse 2014).

The paper is organized as follows. First, the design and working principle of the Zebedee are discussed in section 2, followed by the geometric models and methods used for assessing the accuracy in section 3. The experimental datasets are introduced in section 4. The paper concludes with the results and analysis in section 5.

2 Zebedee Scanner

The Zebedee was originally developed by the Autonomous Systems Laboratory at the Commonwealth Scientific and Industrial Research Organisation (CSIRO), based in Brisbane, Australia. It consists of a 2D scanner (Hokuyo UTM-30LX, horizontal field of view = 270°, maximum range = 30 m) mounted on a spring attached to a handle (Fig. 1). Scans are continuously captured with a swinging scanner head while the user is walking at a gentle speed. The user holds the handle and allows the scanner to swing back and forth along the walking direction (Fig. 2). An inertial measurement unit (IMU), MicroStation 3DM-GX2, is used to provide measurements of the scanner head motion at the initial stage and also during the scanning mission. A small laptop is integrated with the system for recording the data and is placed in a backpack.

The working principle of the Zebedee is based on SLAM in which the system trajectory is reconstructed by continuously estimating the six-degree-of-freedom (6-DOF) of the

Fig. 1: Zebedee scanner and its associated hardware.

Fig. 2: Scanner head's and the user's motion.

motion of the scanner head. This is done using the iterative closest point (ICP) method with input of surface patches identified from the scene. The 6-DOF between two subsequent epochs are estimated by the ICP which minimizes the distances between the conjugate surfaces patches, and also the deviation of IMU accelerations and rotation velocities (Bosse et al. 2012).

3 Methodology

3.1 *Reference Data*

In order to analyse the accuracy of the Zebedee, a set of objects of interest in cultural heritage recording was captured with a Leica ScanStation C10. The C10 data were collected from different stations ensuring that all sides of the objects of interest were visible from at least one scan setup. Several Leica High Definition Surveying (HDS) targets were placed in the field of view of the scanner that allowed the registration of the individual point clouds into a common system, which was refined using the ICP method embedded in the Leica Cyclone.

3.2 *Object Modelling*

The fitting accuracy of several common geometric features was used in the comparison and analysis, with primary focus on simple geometric primitives such as planes, cylinders, catenaries and square prisms/pyramids. The geometric model used for fitting the planar and cylindrical features into the point cloud can be found in Chan et al. (2015), and the geometric model of the 3D catenary curve in Chan et al. (2013). Instead of setting up a target field for evaluation, a square building itself can be used by modelling all four facades simultaneously as a square prism or pyramid. The geometric models for a square prism/pyramid are derived from the octagonal pyramid model (Chan & Lichti 2014). The fundamental concept is to express one side of the square (in the first quadrant, red in Fig. 3a) with a tangent function with argument equal to half of the interior angle (90° for square). Thanks to its symmetry, all other sides of the prism are easily represented by rotation around the Z-axis. The model is given by (1) and (2), with the number of sides set as $n = 4$ and the gradient factor $k = 0$ for a square prism; and with $n = 4$, $k \neq 0$ for a square pyramid.

$$f(\bar{x},\bar{l}) = [(R_0 - kZ') - X']\tan\left((1-\frac{2}{n})\cdot 90^\circ\right) - Y' = 0 \quad (1)$$

where

$$\begin{pmatrix} X' \\ Y' \\ Z' \end{pmatrix} = \mathbf{R}_3\left((q-1)\cdot\frac{360^\circ}{n} + \Psi \right)\mathbf{R}_2(\Phi)\mathbf{R}_1(\Omega)\begin{pmatrix} X - X_c \\ Y - Y_c \\ Z \end{pmatrix} \tag{2}$$

and (X_c, Y_c) is the prism/pyramid centre in the *XY*-plane; Ω, Φ and Ψ are the rotation angles for the rotation matrices $\mathbf{R}_1$, $\mathbf{R}_2$ and $\mathbf{R}_3$ about the *X*-axis, *Y*-axis and *Z*-axis, respectively. The rotational and translational parameters are depicted in Fig. 3b. The tetragonal radius (R_0) is defined at Z = 0, and q is defined as the quadrant number for each point with

$$q = \left\lceil \frac{\Theta n}{360^\circ} \right\rceil \tag{3}$$

where Θ ($0° < \Theta \leq 360°$) is the angle from the *X*-axis on the *XY*-plane in the normal position. q is calculated and updated during the fitting adjustment process and no pre-calculation is needed. The implementation of the fitting is based on the Gauss-Helmert adjustment model (Förstner & Wrobel 2004).

The quadrant number obtained from the fitting can be used to segment individual facades (planes) from the square prism/pyramid. The angle between two facades, θ, can be calculated by (4) and is used for the accuracy assessment

$$\theta = \cos^{-1}\left(\frac{\vec{p}_1 \cdot \vec{p}_2}{|\vec{p}_1||\vec{p}_2|} \right) \tag{4}$$

where "$\vec{p}_1$ Vektor" and "$\vec{p}_2$ Vektor" are the direction cosine vectors for the two facades obtained from the fitting.

4 Experiments

Four datasets (1 – 4) were collected from several locations in Western Australia (WA), all located in the Murchison Region. The objects of interest in each dataset contain different dominant features such as planes, cylinders, catenaries, prisms, and pyramids, so the sites are very suitable to assess different aspects of the accuracy of the Zebedee scanner.

Dataset 1 (Fig. 4a) was collected using only the Zebedee. An artificial plane (a 60 cm × 90 cm white flat board with 1 cm thickness mounted on a larger wooden board) was set in a vegetation rich area and scanned multiple times over a distance ranging from 1 m – 10 m, with an approximate interval of 0.5 m between scans. Only the white board was extracted based on its known dimension for the accuracy evaluation. The test was set out to determine if the accuracy of the trajectory reconstruction of the Zebedee depends on the variety of the object geometry in the field of

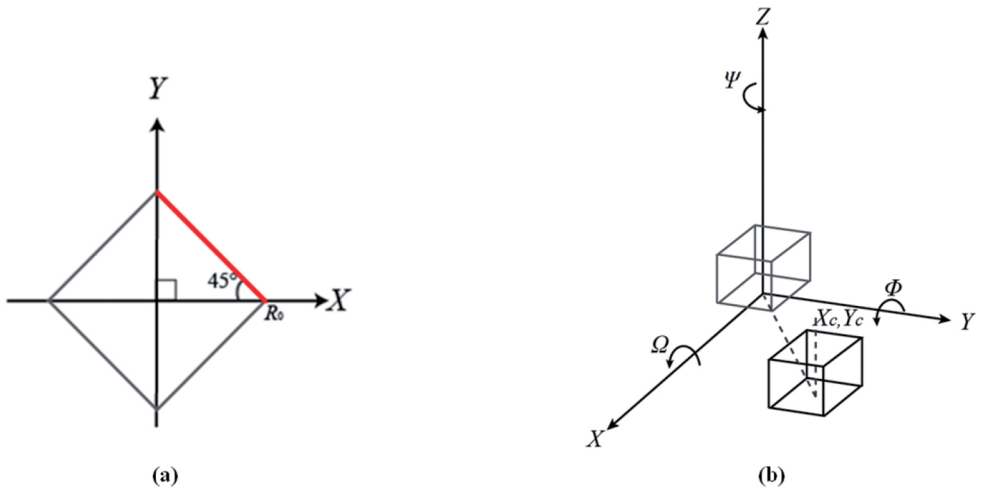

Fig. 3: Model parameters: (a) R_0 at the nominal position and (b) rotational and translational parameters.

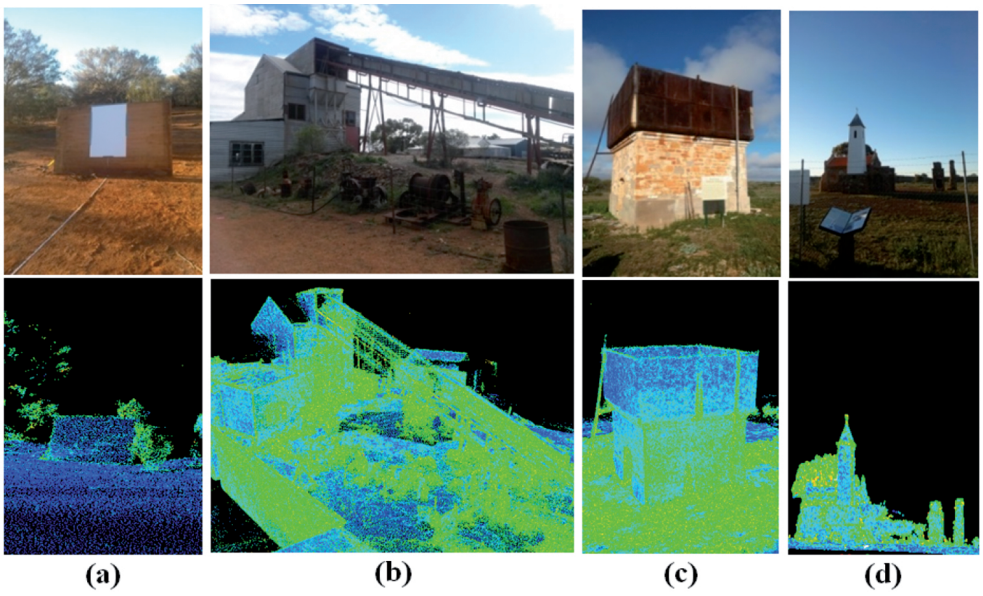

Fig. 4: Scenes and the Zebedee point clouds. (a) Dataset 1: an artificial plane with vegetation around (b) Dataset 2: gold battery (c) Dataset 3: water tank (d) Dataset 4: chapel.

view of the scanner. For all remaining datasets, the objects were captured using the Zebedee and the C10. Dataset 2 (Fig. 4b) was taken at the historical gold battery at Payne's Find. This dataset contains cylindrical and catenary features such as circular oil tanks and power cables. Eight vertical and two horizontal cylinders, as well as three catenaries were extracted from Dataset 2. Dataset 3 (Fig. 4c) is a square water tank within the Yalgoo Railway Station Precinct. The stone masonry base was suitable for fitting a prism model. Dataset 4 (Fig. 4d) is the former Dominican Convent Chapel of St Hyacinth in Yalgoo. This dataset contains a 5 m tall square pyramid tower.

The first test focused on the plane fitting accuracy as a function of the distance of the Zebedee scanner to a plane. For this test the ground surface was removed from the dataset for more effective histogram analysis. The normal vector and curvature information of the point cloud were computed using the CloudCompare software package v.2.6.1 for analysis. The implementation is based on the point cloud library (PCL; PCL 2015). Tests 2 – 4 required the detection and extraction of planes and the cylinders. This was done using a semi-automatic approach applying the random sample consensus (RANSAC) shape detection algorithm (Schnabel et al. 2007). This function was implemented as a plugin of the CloudCompare software package v.2.6.1. The catenaries were extracted manually using the same software. Some of the point clouds are shown in Fig. 5. A summary of the tests and used datasets is given in Tab. 1.

Tab. 1: Overview of the accuracy tests and the used data.

	Scans captured with		**Dataset**			
Accuracy tests	Zebedee	C10	1	2	3	4
1. Plane Fitting vs. Distance	×		×			
2. Cylinder and Catenary Fitting	×	×		×		
3. Square Prism Fitting	×	×			×	
4. Square Pyramid Fitting	×	×				×

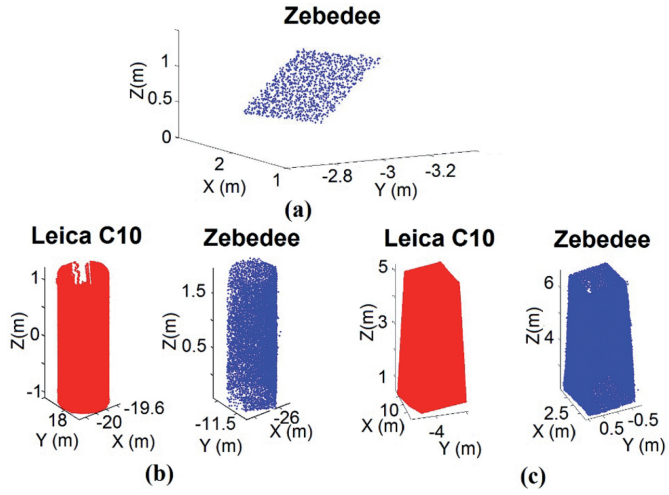

Fig. 5: Extracted point clouds: (a) Dataset 1: plane at 1 m, (b) Dataset 2: vertical cylinder, (c) Dataset 4: square pyramid.

5 Results and Analyses

5.1 *Plane Fitting Accuracy of the Zebedee Vs. Distance (Dataset 1)*

The root-mean-square (RMS) errors of the plane fitting versus the scanning distance are plotted in Fig. 6. The plane fit precision decreases from 1 m to 2 m scanning distance, and then gradually improves over the distance of 2 m – 10 m. Although this behaviour is counter-intuitive since LiDAR precision generally degrades as a function of distance, it can be explained with reference to the operational principles of the Zebedee system. As the scanning distance increased, more of the surrounding environment, including vegetation, was scanned by the LiDAR system. Therefore, both the number of measured points and the geometric variety (as indicated by the increasing curvature statistics in Tab. 2 increased. Both factors improve ICP estimation that reconstructs the system trajectory. Accordingly, the plane measurement quality, i.e. lower RMS, was improved when more vegetation was scanned. The mean curvature is the average of the principal curvatures which is a quantity measuring how large a small surface (in a spherical neighbourhood having a radius of 2.5 cm) bends relatively to the tangent and normal planes defined by the surface normal. Therefore, point clouds with higher mean curvature exhibit greater geometric variation. The Zebedee developer performed a scanning test (Bosse et al. 2012) on different environments containing different types of surfaces, e.g. hallway, courtyard, and grassland, and also found that lack of surfaces with high geometric variation during the scanning leads to less reliable trajectory reconstruction.

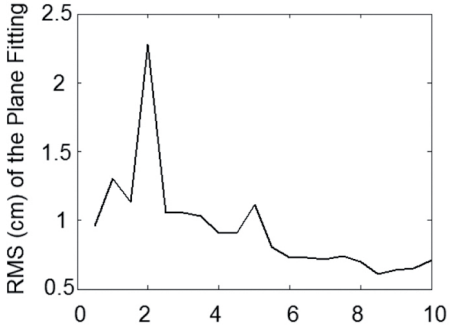

Fig. 6: RMS of plane fitting for the Zebedee point cloud versus scanning distance (top of each plot).

The mean RMS of the plane fitting for all the scanning distances is 9.4 mm, which represents approximately 30% of the mean error (32 mm) of the plane fitting reported in Thomson et al. (2013). They compared the plane

fitting accuracy after registering the overall Zebedee point cloud with the referenced point cloud (captured by Faro Focus^{3D}). This additional step may have degraded the results. In addition, their Zebedee scans were performed inside an indoor rectangular walking corridor where vertical walls and floors/ceilings are the main reference objects for the trajectory reconstruction. The geometric variation in this environment, which is lower than that of the scene studied herein, may also be a reason or the lower accuracy.

The histograms of the planar residuals (distances between points-to-the best fit plane) for scanning distances 1 to 10 m are shown in Fig. 7. It can be seen that all the histograms at all scanning distances except at 2 m are approximately Gaussian in shape, so the planar model is appropriate. At 2 m, the residuals are not Gaussian (Fig. 7), and large residuals are randomly distributed (Fig. 8a) as the scanner positions are not accurately reconstructed due to lack of scans with high geometric variation which is indicated by the distribution of the

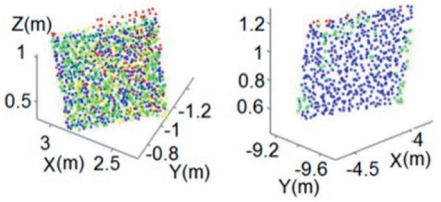

Fig. 8: Spatial distribution of the residuals of the plane fittings at (a) 2 m and (b) 10 m. Colour scale: blue = 0 cm – 1 cm, green = 1 cm – 2 cm, yellow = 2 cm – 3 cm, red > 3 cm.

curvature. Tab. 2 shows that the standard deviation at 2 m is the lowest while the mean of the fitted Gaussian of the curvature increases with the distances. The lowest standard deviation (σ) at 2 m implies the curvatures are the most homogenous so the scanner position cannot be accurately determined based on the SLAM. The mean of the fitted Gaussian increases with the scanning distance because in general more vegetation is scanned as the scanning distance increases.

Tab. 2: Statistics of the mean curvature histograms of the Zebedee point cloud (full scene) for Dataset 1. The mean curvature indicates the extent of the point cloud geometric variation.

Plane Scanning Distance (m)	No. of Points	Mean of Fitted Gaussian Distribution for the Curvature Histogram (m^{-1})	σ of the Fitted Gaussian Distribution for the Curvature Histogram (m^{-1})
1	184,870	0.1122	0.0646
2	192,550	0.1137	0.0627
4	216,232	0.1110	0.0677
7	240,968	0.1340	0.0788
10	361,289	0.1589	0.0840

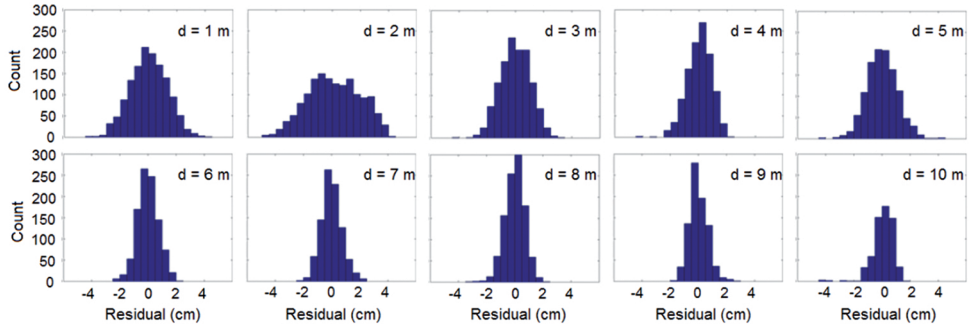

Fig. 7: Histograms of residual of the plane fittings at scanning distance (d) from 1 m to 10 m.

5.2 *Geometric Fitting Accuracy*

5.2.1 Cylinder and Catenary Fitting Accuracy (Dataset 2)

The RMS of the fitting residuals and the radii of the ten cylindrical objects scanned using both instruments are given in Tab. 3. While there is a significant difference in the RMS of the fitting between instruments partially due to the large differences in number of the observed points, the estimated radii are quite comparable. The smallest difference for the estimated radii is only 1 mm (Cylinder 4), while the mean relative difference of all radii is 1.4 %. The mean RMS error of the cylinder fitting for the C10 is approximately 5 mm while for the Zebedee it is 14 mm, so there is only approximately 8 mm difference. The F-test was carried for the cylinder fittings in which the empirical variances of the datasets are compared by computing the F-statistics. The F-tests are two tailed with 5% significance level, and the null hypothesis is $\sigma^2_{C10} = \sigma^2_{ZEB}$. Only two out of the ten cylinder fittings has the null hypothesis which are not rejected, so the difference between two sets of fitting are statistically significant even though the differences between the estimated radii of the two datasets for most of the fittings are on millimetre level.

The overall accuracy of cable-like objects modelled as catenary curves is lower (Tab. 4). Since the cable-like objects are very thin, the reflected laser energy was diminished due to the expanding beam width. The fitting accuracy of the Zebedee is approximately 24 mm lower than the one using the C10. The spatial distribution of the residuals for some of the features for C10 and Zebedee are shown in Figs. 9 – 11. It can be seen that the Zebedee form-fitting errors are randomly distributed. The majority of the errors fall in the range 0 cm – 1 cm. The Zebedee accuracy for catenary is not as high as for cylinder compared to the C10 but it can still be used for catenary survey if centimetre level of accuracy is desired.

Tab. 4: RMS of the catenary curve fitting.

RMS of the Catenary Fitting (m)		
Catenary	**Leica C10**	**Zebedee**
1	0.018	0.052
2	0.008	0.027
3	0.016	0.037
Mean	0.014	0.039

Tab. 3: RMS and estimated radii of the cylinder fitting (Cylinders 1 – 8 are vertical; Cylinders 9 – 10 are horizontal).

Cylinder	No. of points (Approx. scanning distance (m))		RMS of the fitting residuals		Estimated Radius, r		
	Leica C10	Zebedee	Leica C10 (m)	Zebedee (m)	Leica C10 (m)	Zebedee (m)	Difference (%)
1	88,608 (4)	8,753 (2)	0.003	0.012	0.383	0.371	2.9
2	16,418 (5)	2,725 (2)	0.005	0.017	0.288	0.290	0.5
3	263,159 (5)	6,980 (2)	0.006	0.011	1.272	1.279	0.6
4	23,386 (2)	2,499 (2)	0.007	0.015	0.253	0.254	0.4
5	5,688 (6)	610 (3)	0.004	0.015	0.287	0.278	3.2
6	2,415 (7)	441 (3)	0.005	0.014	0.281	0.276	1.8
7	8,103 (5)	1,406 (2)	0.006	0.015	0.289	0.293	1.3
8	9,694 (5)	1,188 (2)	0.005	0.012	0.287	0.285	0.8
9	8,327 (5)	1,055 (2)	0.002	0.009	0.255	0.261	2.5
10	6,619 (6)	374 (5)	0.008	0.021	0.378	0.376	0.5
Mean			0.005	0.014			

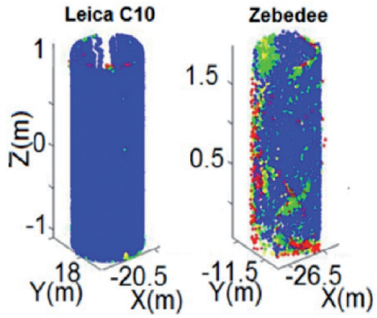

Fig. 9: Spatial distribution of the residuals (point-to-model distances) for Cylinder 1 (Vertical). Colour scale: blue = 0 cm – 1 cm, green = 1 cm – 2 cm, yellow = 2 cm – 3 cm, red > 3 cm.

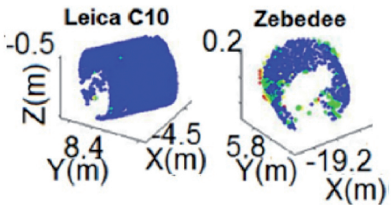

Fig. 10: Spatial distribution of the residuals (point-to-model distances) for Cylinder 9 (Horizontal). Colour scale: blue = 0 cm – 1 cm, green = 1 cm – 2 cm, yellow = 2 cm – 3 cm, red > 3 cm.

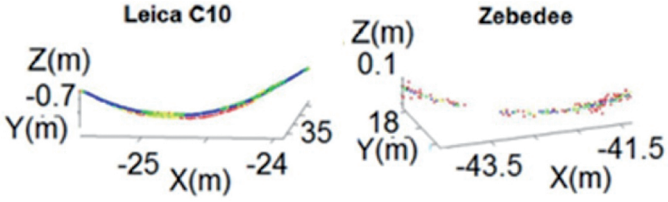

Fig. 11: Spatial distribution of the residuals (point-to-model distances) for Catenary 1. Colour scale: blue = 0 cm – 1 cm, green = 1 cm – 2 cm, yellow = 2 cm – 3 cm, red > 3 cm.

5.2.2 Square Prism Fitting Accuracy (Dataset 3)

Tab. 5 shows the RMS and the estimated radius (R_0) of the stone masonry base of the water tank obtained from fitting the square prism model ((1) and (2)). The residual statistics differ less than 7 mm and the estimated radii only differ by 0.8%. Tab. 6 shows the residuals for individual planes according to quadrant number (as each point is associated with a unique quadrant number) after the square prism fitting. The results are consistent with those of test 2 (cylinder fitting). The angles computed between adjacent walls are shown in Tab. 7. All angles of the square prism are close to 90°. The similarity of the derived angles suggests that the measurement accuracy of the Zebedee is comparable to that of the C10. However, Fig. 12 shows that one wall has a greater number of errors in the 1 cm – 2 cm range and errors > 3 cm concentrated near the edges. This lower accuracy of the wall measurement is likely attributed to relatively higher swinging/moving speed of the scanner (this condition is unique for Dataset 3). This indicates that the motion stability of the system is also a factor of the limited accuracy (Kaul et al. 2015), but would require further investigation to confirm. The results also suggest that the Zebedee tends to have lower accuracy at wall edges probably due to the edge effect (only relatively smaller part of laser energy is reflected at edges compared to flatter surfaces), but again further study is needed.

5.2.3 Square Pyramid Fitting Accuracy (Dataset 4)

The height of the extracted square pyramid of the Chapel tower is approximately 5 m. The estimated radii and gradient factor (position/orientation-independent parameters) between the Zebedee and the C10 tower differ by about 7% (Tab. 8). This discrepancy is much higher than the results in the previous test (note that k was not estimated for the previous test of the square prism). Since the tower was scanned the same way as the water tank in the previous test (the operator held the scanner and

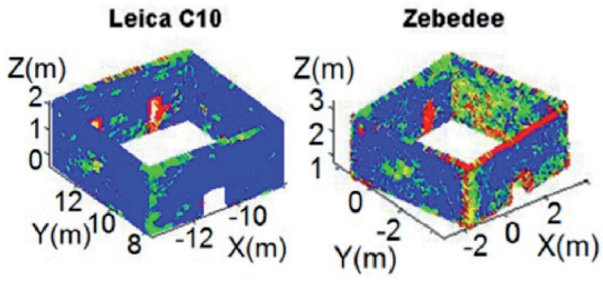

Fig. 12: Spatial distribution of the prism residuals (point-to-model distances). Colour scale: blue = 0 cm – 1 cm, green = 1 cm – 2 cm, yellow = 2 cm – 3 cm, red > 3 cm.

Tab. 5: RMS and estimated radii of the square prism fitting for Dataset 3.

	RMS	Estimated R_0			
	Leica C10 (m)	Zebedee (m)	Leica C10 (m)	Zebedee (m)	Diff. (%)
Water Tank	0.007	0.014	4.088	4.120	0.8

walked around the target in an open field), the reference objects for the ICP estimation were only the target itself and some sparse vegetation in both tests. Under similar scanning reference conditions, the scanning range of the tower (approximately 5 m – 8 m) is higher than that of the previous test (approximately 2 cm – 3 m). As a result, the measurement accuracy of the tower is lower. In addition, the scanning orientation was significantly different compared to the previous test because the object was 1 m – 5 m above the scanner. So, there are no horizontal reference objects available at the same height. Even though the estimated mo-del parameters for the prism/pyramid differed more, the plane fitting accuracies for the individual parts were consistent with previous test results (Tab. 9). However, the deviations between interior angles are slightly higher compared to previous tests (Tab. 10). This is likely due to the fact that the walls are much shorter in this case. The mean side length of the tower and the water tank are 0.95 m and 5.76 m, respectively. Therefore, errors in the perpendicular distances (Zebedee) for the tower and water tank corresponding to mean angular errors, 0.328° and 0.267°, are 5.43 mm and 2.68 mm, respectively. Fig. 13 shows that many points with the larger errors are distributed near the top for both the scanners and near the edges (similar to the water tank) in the Zebedee point cloud.

6 Conclusion

In this paper, the survey accuracy of the Zebedee scanner, a SLAM-based hand-held mobile mapping LiDAR device, was intensively studied. The accuracy was accessed using multiple types of geometric primitives with their models fitting to point clouds of objects at several cultural heritage sites in Australia. The primitive-based accuracy evaluation method has several merits over the point-based method for several reasons such as higher redundancy can be obtained and point intensity is not needed. The fitting accuracy was compared to that of a conventional high accuracy terrestrial LiDAR scanner, the Leica ScanStation C10. The results suggest that the availability and geometric variation of the surrounding reference objects are important for capturing more accurate Zebedee point cloud. For feature measurement, the Zebedee accuracy is very comparable to the C10, with centimetre-level dif-

Tab. 6: RMS of plane fitting.

	RMS of the Plane Fitting (m)	
	Leica C10	Zebedee
Wall 1	0.010	0.013
Wall 2	0.006	0.010
Wall 3	0.005	0.013
Wall 4	0.005	0.014
Mean	0.007	0.013

Tab. 7: Estimated angles between two walls for Dataset 3.

	Angle between two walls (°)	
	Leica C10	Zebedee
Wall 1 & 2	89.889	89.965
Wall 2 & 3	89.850	89.981
Wall 3 & 4	89.928	89.958
Wall 1 & 4	89.889	89.989

Tab. 8: RMS and estimated parameters of the square pyramid fitting for Dataset 4.

	RMS		Estimated R_0			Estimated k		
	Leica C10 (m)	Zebedee (m)	Leica C10 (m)	Zebedee (m)	Diff. (%)	Leica C10	Zebedee	Diff. (%)
Tower	0.007	0.012	1.178	1.257	6.7	0.0562	0.0522	7.1

Tab. 9: RMS of plane fitting.

	RMS of the Plane Fitting (m)	
	Leica C10	Zebedee
Wall 1	0.006	0.013
Wall 2	0.006	0.009
Wall 3	0.005	0.011
Wall 4	0.005	0.010
Mean	0.006	0.011

Tab. 10: Estimated angles between two walls for Dataset 4.

	Angle between two walls (°)	
	Leica C10	Zebedee
Wall 1 & 2	89.937	89.591
Wall 2 & 3	89.636	90.094
Wall 3 & 4	89.936	89.611
Wall 1 & 4	90.594	90.420

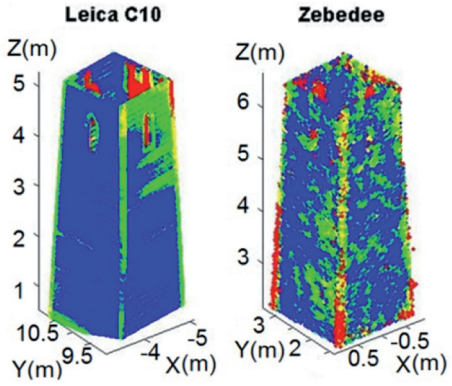

Fig. 13: Spatial distribution of the pyramid residuals (point-to-model distances). Colour scale: blue = 0 cm – 1 cm, green = 1 cm – 2 cm, yellow = 2 cm – 3 cm, red > 3 cm.

ferences in plane fitting. The mean RMS errors for plane, cylinder, catenary, prism and pyramid fitting for the Zebedee point clouds were all less than 1.5 cm. The estimated cylinder radii between the Zebedee and the C10 differed by only 1.4% difference on average, while the radii difference from the prism/pyramid fitting was 0.8%. Overall, the Zebedee scanner is suitable for heritage mapping, not only because of its ease of use (extensive training for the operation and data processing are not needed), but also because the desired centimetre-level accuracies can be achieved. In addition, due to its portability and compactness, the Zebedee can be operated in areas that may be inaccessible for conventional terrestrial scanners.

Acknowledgement

This research was partially supported by an Australian Endeavour Research Fellowship (2014) awarded to the first author by the Australian Government. The data were collected during the site survey for the Curtin University Survey Expedition 2014 sponsored by the following organizations: RM Surveys, Whelans, Land Surveys, Cottage & Engineering Surveys, McMullen Nolan Group, Silver Lake Resources, C.R. Kennedy, Haefeli-Lysnar, Landgate, State Heritage Office, SSSI, LSLB and WAIS. We want to thank CSIRO for providing the Zebedee for this research project and the associated training. The authors would also like to thank all the staff, volunteers and students who participated in the Survey Expedition.

References

Alismail, H., Baker, D. & Browning, B., 2014: Continuous trajectory estimation for 3D SLAM from Actuated LiDAR. – IEEE International Conference on Robotics & Automation (ICRA), Hong Kong, China.

Bosse, M., Zlot, R. & Flick, P., 2012: Zebedee: Design of a spring-mounted 3-D range sensor with application to mobile Mapping. – IEEE Transactions on Robotics **28** (5): 1–15.

Bosse, M. & Zlot, R., 2013: Place recognition using keypoint voting in large 3D Lidar datasets. – IEEE International Conference on Robotics and Automation, Karlsruhe, Germany.

Chan, T.O., Lichti, D.D. & Glennie, C., 2013: Multi-Feature based boresight self-calibration of a terrestrial mobile mapping system. – ISPRS Journal of Photogrammetry and Remote Sensing **82**: 112–124.

Chan, T.O. & Lichti, D.D., 2014: Geometric modelling of octagonal lamp poles. – International Archives of Photogrammetry, Remote Sensing and Spatial Information Sciences XL-5, ISPRS Technical Commission V Symposium, Riva del Garda, Italy.

Chan, T.O., Lichti, D.D. & Belton, D., 2015: A rigorous cylinder-based self-calibration approach

for terrestrial laser scanners. – ISPRS Journal of Photogrammetry and Remote Sensing **99**: 84–99.

Chow, J.C., Lichti, D.D., Hol, J.D., Bellusci, G. & Luinge, H., 2014: IMU and multiple RGB-D camera fusion for assisting indoor stop-and-go 3D terrestrial laser scanning. – Robotics **3**: 247–280.

CSIRO, 2015: Zebedee. – https://wiki.csiro.au/display/ASL/Zebedee (17.8.2015).

Engineering & Technology, 2013: Spring-mounted Zebedee maps Pisa Tower in 3D. – http://ieeexplore.ieee.org/stamp/stamp.jsp?arnumber=6676302 (17.8.2015).

Förstner, W. & Wrobel, B., 2004: Mathematical concepts in photogrammetry. – McGlone, J.C., Mikhail, E.M., Bethel, J. & Mullen, R. (eds.): Manual of Photogrammetry: 15–180, 5th ed., ASPRS, Bethesda, MD, USA.

Kaul, L., Zlot, R. & Bosse, M., 2015: Continuous-time three-dimensional mapping for micro aerial vehicles with a passively actuated rotating laser scanner. – Journal of Field Robotics: 1–30.

Kukko, A., Kaartinen, H., Hyyppä, J. & Chen, Y., 2012: Multiplatform mobile laser scanning: usability and performance. – Sensors **12** (9): 11712–11733.

PCL, 2015: Estimating surface normals in a point cloud. – Point Cloud Library; http://pointclouds.org/documentation/tutorials/normal_estimation.php (20.8.2015).

Schnabel, R., Wahl, R. & Klein, R., 2007: Efficient RANSAC for point-cloud shape detection. – Computer Graphics Forum **26** (2): 214–226.

Thomson, C., Apostolopoulos, G., Backes, D. & Boehm, J., 2013: Mobile laser scanning for indoor modelling. – ISPRS Annals of Photogrammetry, Remote Sensing and Spatial Information Sciences II (5/W2), ISPRS Laserscanning Workshop, Antalya, Turkey.

Vosselman, 2014: Design of an indoor mapping system using three 2D laser scanners and 6 DOF SLAM. – ISPRS Annals of the Photogrammetry, Remote Sensing and Spatial Information Sciences, II(3), ISPRS Technical Commission III Symposium, Zurich, Switzerland.

Zhang, J. & Singh, S., 2014: LOAM: Lidar odometry and mapping in real-time. – Robotics, Science and Systems Conference, Berkeley, CA, USA.

Zlot, R. & Bosse, M., 2014: Three-dimensional mobile mapping of caves. – Journal of Cave and Karst Studies **76** (3): 191–206.

Addresses of the Authors:

Ph.D. Ting On Chan & Prof. Ph.D. Derek D. Lichti, Department of Geomatics Engineering, Schulich School of Engineering, University of Calgary, 2500 University Dr NW, Calgary, Alberta, T2N1N4 Canada, Tel.: {+1-403-210-7140}{+1-403-210-9495}, Fax: +1-403-284-1980, e-mail: {ting.chan} {ddlichti} @ucalgary.ca

Ph.D. David Belton, Department of Spatial Sciences, Curtin University, GPO Box U1987, Perth, WA 6845, Australia, Tel.: +61-8-9266-2704, Fax: +61-8-9266-2703, e-mail: d.belton@curtin.edu.au

Dr. DI (FH). Bernhard Klingseisen, State Heritage Office, Bairds Building, Level 2, 491 Wellington Street, Perth WA 6000, Australia, Tel.: +61-8-6552-4060, Fax: +61-8-6552-4001, e-mail: bernhard.klingseisen@stateheritage.wa.gov.au

Dr.-Ing. Petra Helmholz, Department of Spatial Sciences, Curtin University, GPO Box U1987, Perth, WA 6845, Australia, Tel.: +61-8-9266-3369, Fax: +61-8-9266-2703, e-mail: petra.helmholz @curtin.edu.au

Manuskript eingereicht: September 2015
Angenommen: April 2016

Berichte von Veranstaltungen

15. Oldenburger 3D Tage, 3. und 4. Februar 2016, Oldenburg

Mit 223 Teilnehmern aus 7 Ländern erwiesen sich die 15. Oldenburger 3D-Tage wieder als jährlicher Anlaufpunkt für Wissenschaftler, Anwender und Hersteller für die vielfältigen Verfahren der dreidimensionalen optischen Messtechnik. Thomas Luhmann konstatierte auch nach 14 Jahren ein ungebrochenes Interesse an der bewährten Veranstaltung. In seinen Grußworten für die Stadt Oldenburg sprach der Oberbürgermeister Jürgen Krogmann der Jade Hochschule und insbesondere dem Institut für Angewandte Photogrammetrie und Geoinformatik ein Kompliment für die Entwicklungen in der optischen 3D-Messtechnik aus. Ferner stellte er die Zusammenarbeit zwischen der Hochschule und der Stadt in den vielfältigen Anwendungsgebieten der raumbezogenen Datenverarbeitung als Oldenburger Prädikat heraus. Der neue Präsident der Jade Hochschule, Manfred Weisensee, unterstrich den Reiz der Oldenburger 3D-Tage für junge Wissenschaftler. Er brachte seine Hoffnung zum Ausdruck, dass der zukünftige Fachbereich Bauwesen • Geoinformation • Gesundheitstechnologie weiterhin eine Keimzelle für neue Entwicklungen im Zuge der angewandten Forschung sein möge. Lena Halounová, Kongressdirektorin des nächsten ISPRS-Kongresses, sprach eine Einladung nach Prag vom 12. bis 19. Juli 2016 aus. Sie stellte im Überblick das interessante Kongressprogramm vor. Sie wünschte sich, dass sie viele Teilnehmer der 3D-Tage auch in Prag begrüßen kann.

Den Eröffnungsvortrag hielt in diesem Jahr Rainer Tutsch vom Institut für Produktionsmesstechnik der TU Brauschweig. Er stellte unter dem Titel „Das Triangulationsprinzip – der Kern der optischen 3D-Messtechnik“ zunächst die Grundlagen der bildbasierten Messverfahren in abstrakter Form dar. Anschließend spannte er den Bogen über aktive und passive Sensoren bis hin zu den Anwendungen. Dabei ging er insbesondere auf die Messung von reflektierenden und transmittierenden Oberflächen ein, welche in der Vergangenheit mit optischen Messsystemen nur eingeschränkt zu erfassen waren. Mit der Deflektrometrie stellte er hierzu neue Messverfahren einschließlich Ansätzen zur Abschätzung der Messunsicherheiten dieser Verfahren vor.

Die Fachvorträge wurden zum größten Teil in zwei parallel stattfindenden Blöcken präsentiert. Im ersten Block „Dynamische Prozesse I“ referierten zunächst die Autoren um Marcus Grosse, EnShape GmbH, über ein Experiment, bei dem Wasserwellen hochgenau mit Hilfe von Streifenlichtprojektions-Technologie vermessen werden. Christina Steiner, Audi AG, stellte ein Stereo-Endoskopsystem vor, das während eines Crashtests im Auto mitfährt und somit ermöglicht, den Innenraum dynamisch zu vermessen. Stereo-Endoskopie wurde auch von Niklas Conen, Jade HS, zur Oberflächenerfassung eingesetzt. Anwendung war in diesem Fall die Unterstützung bei chirurgischen Eingriffen. Thomas Luhmann berichtete über ein Verfahren zur Echtzeit-Messung von Kopfbewegungen, die hörgeschädigte Probanden während eines Tests vollziehen.

Der Vortragsblock „Aufnahme und Prozessierung von Laserscandaten“ hatte die Kopplung von TLS mit weiteren Sensoren sowie die Planung von TLS-Aufnahmen als Schwerpunkte. Frank Gielsdorf, technet GmbH, stellte methodische Ansätze und Genauigkeitsbetrachtungen zur Fusion von Punktwolken aus TLS- und Handheldscanner-Messungen vor. Diese ermöglichen die Vervollständigung von TLS-Punkten im Bereich von Scanschatten insbesondere bei der Bauwerksdokumentation. Unter dem Titel „Modellbasierte Standpunktplanung für terrestrische Laserscanner unter ingenieurgeodätischen Gesichtspunkten“ zeigte Daniel Wujanz, TU Berlin, aktuelle Forschungsergebnisse zur Optimierung der Standpunktanordnung für TLS-Aufnahmen mit stochastischen Ansätzen. Thomas Willemsen, HafenCity Universität Hamburg, stellte anschließend Untersuchungsergebnisse des inertialen Low-Cost-Sensors MEMS MPU-6050 vor und gab einen Ausblick zum Einsatz dieses Sensors in geodätischen Anwendun-

DOI: 10.1127/pfg/2016/0295 1432-8364/16/0295 $ 2.50

gen. Abschließend stellte Robin Rofallski, Jade Hochschule Oldenburg, Untersuchungen zur Synchronisation von TLS und AICON MoveInspect vor. Mit der Sensorfusion von TLS- und HighSpeed-Photogrammetrie sollen dynamische Prozesse, wie z.B. das Bewegungsverhalten von Windkraftanlagen, evaluiert werden.

Als erster Vortragender im Block „Kalibrierung und Messunsicherheit“ stellte Waldemar Mordwinzew, Hochschule Mainz, die Ergebnisse seiner Dissertation unter dem Titel „Analyse von Bildresiduen mit Machine Learning im Kontext von Kamerakalibrierungen“ vor. Die Zielsetzung dieser Arbeiten ist die Interpretation von Residuen und das Aufzeigen von nicht erfassten Restsystematiken bei Kamerakalibrierungen. Anschließend brachte Christian Mulsow, TU Dresden, dem Auditorium einen universellen Ansatz zur Mehrmedien-Bündeltriangulation näher. Dabei werden Verfahren des Ray-Tracings zur Modellierung des Strahlengangs bei der Durchdringung von Trennflächen genutzt. Michael Lösler, Frankfurt University of Applied Sciences, ging in seinem Vortrag „Verfahren zur Transformation von Parametern und Unsicherheiten bei nichtlinearen Zusammenhängen“ auf erweiterte Ausgleichungsmodelle und die Anwendung der unscented transformation zur Unsicherheitsabschätzung ein. Abschließend stellte Tanja Ekkel von der Jade Hochschule praktische Untersuchungen zum Einfluss von Maßstäben in photogrammetrischen Projekten großer Volumina vor. Ziel dieser Untersuchungen war eine Optimierung von Maßstabsanordnungen und -längen bei großvolumigen Objekten.

Der Vortragsblock „Modellierung“ wurde von Dorit Borrmann, JMU Würzburg eröffnet. Der Beitrag „Automatische Grundrisserstellung mittels Laserscandaten“ beschrieb einen Ansatz zur automatischen Kartierung von Räumen mit Hilfe eines autonomen Roboters. Anschließend demonstrierte Christian Tonn, Faro AG, eine Software zur interaktiven Gebäudemodellierung aus Punktwolken. Lennart Gruse, Jade HS, stellte die Ergebnisse seiner Bachelorarbeit vor, in der er kleine Strukturen an Brückenbauwerken mit Hilfe einer Kombination aus Laserscanning und Monoplotting erfasst hat. Im letzten Vortrag dieses Blocks hat Martin Meister, Fraunhofer AGP, ein im Schiffbau eingesetztes Verfahren zur as-is-Dokumentation der Innenausstattung basierend auf Laserscannerdaten vorgestellt.

Unter dem Titel des Blockes „Industrielle Anwendungen“ wurden Verfahren zur Überwachung von Produktionsanlagen sowie die Ausrichtung von Teilchenbeschleunigern subsumiert. Michael Kleinkes, Espace 2001, stellte unter dem Titel „Echtzeitpositionierung durch messwertgestützte Positionskorrektur“ den Prototyp eines Toolkit zur Korrektur des Bewegungsverhaltens von Fertigungsrobotern während des Produktionsprozesses vor. Anschließend berichtete Cornelia Eschelbach, Frankfurt University of Applied Sciences, über den Einsatz mobiler Koordinatenmesstechnik bei der Aufnahme von Strahlführungselementen eines Elektronenlinearbeschleunigers. Ansätze zur Ausnutzung des vollständigen Genauigkeitspotenzials dynamischer Fertigungsprozesse vermittelte Mirko Riedel, TU Dresden, in seinem Vortrag „Geometrisch-kinematische Kalibrierung von Hexapoden“. Mit „SMART Base Fit – ein neues Verfahren für die Roboter Base-Bestimmung“ stellte Markus Herrmann, SOLID 3D Engineering, einen weiteren Ansatz zur Genauigkeitssteigerung des Positionierungsverhaltens von Industrierobotern während des Produktionsprozesses vor.

Zum Abschluss des Tages kamen die meisten Besucher zum traditionellen Grünkohlessen in der Weser-Ems-Halle zusammen. Neben dem kulinarischen Höhepunkt wurde den Teilnehmern auch wieder ein kulturelles Highlight geboten. In diesem unterhielt die Gruppe "Wat Ihr Wollt" mit kreativem Improvisationstheater, bei dem die Schauspieler ihr spielerisches und auch ihr musikalisches Können unter Beweis gestellt haben.

Der erste Vortragsblock des zweiten Tages „Anwendungen“ hatte vornehmlich den Einsatz von TLS zum Schwerpunkt. Zunächst berichtete Thomas Kersten, HafenCity Universität Hamburg, über ein studentisches Projekt zur archäologischen Dokumentation unter dem Titel „Low-Cost vs. High-End Systeme im Vergleich – 3D-Aufnahme der Ringwallanlage Lembecksburg auf der Nordseeinsel Föhr“ in dem mit statischem und mobilem

Laserscanning sowie UAV-Aufnahmen die volle Bandbreite punktwolkengenerierender Messverfahren zum Einsatz kamen. Anschließend stellte Denys Gorkovchuk von der Kyiv National University of Construction and Architecture eine bunte Vielfalt von TLS-Projekten in der Ukraine vor. Jost Michael Broser, TH Köln, zeigte zum Abschluss des Vortragsblockes die Möglichkeiten und Grenzen der Dokumentation mit terrestrischem 3D-Laserscanning am Beispiel des Amphitheaters in Albano Laziale auf.

Im Block „Sensoren und Plattformen" wurden schwerpunktmäßig Vorträge zu UAV-bezogenen Themen gehalten. Markus Gerke, Universität Twente, zeigte die Ergebnisse von systematischen Qualitätsanalysen für Produkte, welche aus UAV-Aufnahmen abgeleitet wurden. Danach stellte Thomas Linkugel von der Universität Tübingen mit dem FireFly MAV-Framework eine Entwicklungsumgebung für UAV-Autopiloten, welche auf Simulationsrechnung basiert, vor. Michael Depping, Hanack und Partner Hamburg, präsentierte die Entwicklung einer Software zur automatisierten Flugplanung von UAVs, welche er im Rahmen seiner Bachelorarbeit an der HafenCity Universität Hamburg entwickelt hat. Als letzter Vortragender in diesem Block stellte Thomas Kraft, Deutsches Zentrum für Luft- und Raumfahrt, ein Verbundprojekt mit der Hochschule Bochum und der Universität Twente zum Thema „Photogrammetrisches Kamerasystems für UAV mit hochgenauer GNSS/INS Information für standardisierte Verarbeitungsverfahren" vor. Darin wird u.a. untersucht, wie das Genauigkeitspotenzial von UAV-Aufnahmen bei Standardanwendungen ausgenutzt werden kann.

Der erste Vortrag zu „Sensorik" wurde von Jörg Kunze, Basler AG, gehalten. Er stellte einen Ansatz zur Realisierung einer ToF-Kamera basierend auf CCD-Sensoren vor. Gegenüber den herkömmlichen PMD-Sensoren lassen sich mit CCDs unter bestimmten Bedingungen bessere Ergebnisse erzielen. Um Alternativen zu PMD-Sensoren ging es auch beim Vortrag von Marcel Kaufmann, HS Darmstadt. In dem Fall wurde ein System, das mit gepulster Laufzeitmessung arbeitet, getestet. Thomas Wiemann, Universität Osnabrück, berichtete über ein neues Verfahren zur Auswertung von RGB-D-Sensordaten, das sich insbesondere durch die online-Erstellung topologisch korrekter Dreiecksvermaschungen auszeichnet. In seinem Vortrag konzentrierte sich Hannes Sardemann, TU Dresden, auf Genauigkeitsuntersuchungen von Streckenmessungen, die mit fokussierten plenoptischen Kameras (Lichtfeldkameras) erzielt werden können. Insbesondere ging der Autor auf die Kalibrierung eines solchen Systems und auf Untersuchungen der Genauigkeit bei längeren Strecken ein. Die Unterstützung bei medizinischen Eingriffen stand im Fokus des Beitrags von Tomasz Bien, Fiagon AG. In dem vorgestellten Verfahren wird eine Instrumentenführung mit Hilfe eines photogrammetrischen Systems realisiert.

Im letzten Block zum Thema „Dynamische Prozesse" vermittelte zunächst Thomas Gaisecker, Riegl LMS GmbH, unter dem Titel „Laserscannersystem für statische und kinematische Datenerfassung mit Echtzeitdatenverarbeitung und Cloud-Anbindung" die Vorzüge eines neuen TLS-Sensorsystems. Danach stellte Lars Marschel, Leibniz Universität Hannover, ein aktuelles Forschungsvorhaben zu einem objektraumbasierten und durch Referenzmessungen gestützten Kalibrierprozess für ein k-TLS basiertes Multi-Sensor-System vor. Dabei wird angestrebt, die Genauigkeit des kinematischen Laserscannings für industrielle Anwendungen zu steigern. Anschließend stellte Christian Hesse, Dr. Hesse und Partner Ingenieure aus Hamburg, am Beispiel der hochpräzisen Bestandsdatenerfassung des A7-Elbtunnels ein interessantes Projekt mit Anwendung des kinematischen Laserscanning vor. Abschließend berichtete Felix Tschirschwitz, HafenCity Universität Hamburg, über die Anwendung des Terrestrischen Laserscannings für Deformationsmessungen. Dabei stellte er ein Entwicklungsprojekt zur TSL-gestützten Buhnenüberwachung in Wasserstraßen vor.

Auch die 15. Veranstaltung dieser Seminarreihe bot ein interessantes und ausgewogenes Programm, welches tiefe Einblicke in aktuelle Entwicklungen der optischen 3D-Messtechnik, der Photogrammetrie und des Terrestrischen Laserscannings ermöglichte. An dieser Stelle sei auf den in Kürze im Wichmann VDE Verlag erscheinende Tagungsband „Pho-

togrammetrie, Laserscanning, Optische 3D-Messtechnik“ verwiesen, in dem die Vortragsinhalte in ausführlicher Form nachzulesen sind. Ferner sind die Vortragsfolien online abrufbar unter https://www.conftool.net/oldenburger-3d-tage/sessions.php. Die nächsten Oldenburger 3D-Tage werden voraussichtlich am 1. und 2. Februar 2017 stattfinden.

Heinz Runne, Hochschule Anhalt, Dessau
Markus Gerke, Universiteit Twente/ITC, Enschede, Niederlande

Begleitende Firmenausstellung zu den Oldenburger 3D-Tagen 2016

Interexpo-GeoSiberia, 20. – 22. April 2016, Novosibirsk, Russia

The 12th Interexpo-Geo Siberia was organized from April 20 to 22, 2016, by the Siberian State University of Geosystems and Technology (SSUGT) in Novosibirsk, Russian Federation. The fair consisted of a geospatial industry exhibit and a scientific and technical forum. The event was well attended by Russian participants, mainly from Siberia, including SSUGT students. However, the usual large foreign participation was rather modest this year. There were 5 participants from Germany, 4 from Czech Republic, 3 from China, 2 from the Netherlands, 1 from Hungary, 1 from Romania, and 1 from Brazil. Responsible for this small international participation were most likely the global political differences. But those who came from abroad were happy to enjoy the cordial reception by our Russian and Siberian colleagues and even to receive letters of gratitude for coming to the event.

The opening of the Interexpo-GeoSiberia was made for the fair by the Governor of the Novosibirsk Region, Vladimir Gorodetsky, and Prof. Alexander P. Karpik, President of SSUGT. Statements were made by Prof. Guo Huadong, President of the International Society of Digital Earth (China), Prof. Laszlo Zentai, Secretary General of ICA (Hungary) and Axel Pohlmann, DVW President of the State of Saxony (Germany). This was followed by an official visit of the exhibits.

With the exception of Digital Globe, the DVW, and KIT Karlsruhe all other exhibitors came from the Russian Federation. Noteworthy was the exhibit of the Russian photogrammetric software company RACURS, which is

globally active. Also, there were several UAV producers from Russia in the exhibit.

The scientific and technical program was initiated by a Plenary Session. Gennady Pobedinsky, Director of the Federal Research and Development Center for Geodesy, Cartography and Spatial Data Infrastructure, Moscow, spoke on new laws to establish NSDI and on standards developed by Tsniigaik released for the Russian Federation. Laszlo Zentai described the NSDI development in Hungary modelled according to the European INSPIRE directive. SOVZOND, Moscow, reported on the industrial development in Russia to create a Russian equivalent to Google Earth and Google Maps. „Smart Cities" cannot be developed without first having geospatial information. Gottfried Konecny, Hannover, Germany, noted, that SSUGT together with MIIGAiK is one of the most important geospatial information technology educational centres in the world. Interexpo-GeoSiberia, the largest geospatial fair in Russia has successfully networked with NGO´s of the geospatial disciplines: FIG, ISPRS, ICA and others organizing successful international workshops with them. Igor A. Musikhin, Vice President of SSUGT, presented a well-documented study by SSUGT on the current trends in geoinformation technology, expressed by publications originating in different countries. Germany followed by China reached the highest number. The biggest markets are expected in remote sensing, real time sensor fusion and BIM. Regarding industrial developments not only scientific literature, but also grey literature, such as Geomatics journals should be included in surveys.

Volker Schwieger, FIG Commission President, Stuttgart, Germany, compared Precise Point Positioning (PPP) GNSS solutions with conventional GNSS technology. The Canadian CRRS-PPP system indeed offered the highest accuracy of +/- 0.02 m in position and +/- 0.05 m in height. PPP includes satellite orbit modelling, ionospheric and tropospheric correction capabilities. Günter Schmitt, KIT Karlsruhe, Germany spoke on dam deformation measurements by GNSS made in Brazil with +/- 0.4 mm accuracy. H.K. Yambaev, MIIGAiK reported about an automated deformation monitoring system using digital inclinometry and Leica tacheometres for the monitoring of locks. E.M. Mazurova, SSUGT, presented the potential improvements of accuracy by 2 orders of magnitude using relativistic geodesy. V.I. Obiedenko, SSUGT, explained the problems in establishing a common real estate cadastre database GSK 2011 in the Russian Federation, in which 30,000 local coordinate systems have to be transferred into a common coordinate system, for which Rosreestr is responsible. This will enable the establishment of an NSDI. Ben Gorte, TU Delft, Netherlands, presented the ongoing effort by TU Delft to build a 2 kg mass Cube satellite to orbit at 600 km height and to carry a hyperspectral scanner of 80 m GSD with a 10 nm spectral resolution hypercube, using onboard processing and data compresses transmission. For this, he suggested to replace pixels with voxels using the centre of the hyperbox for classification.

In the afternoon of April 20, on April 21 and on April 22 in the morning a number of workshops were scheduled:

- *Digital Earth´s Role in Sustainable Development under global climate change*, organized by the International Society of Digital Earth,
- *Early Warning in the Big Data Era*, organized by ICA,
- *Open Source GIS*, organized by SSUGT,
- *Real Estate Cadastral development*, organized by SSUGT with a contribution by Otmar Schuster, Mülheim, Germany, and
- *Global Geospatial Information and High Resolution Global Land Cove*r, organized by ISPRS.

The latter ISPRS workshop was chaired by Gottfried Konecny, with the following presentations:

The Status of Topographic Mapping in the World – a UNGGIM-ISPRS Project 2012-2014 by Gottfried Konecny: The study based on questionnaires distributed by UNGGIM and supplemented by other sources, established, that the land areas of the globe are covered by 33.5% at scale 1:25 000, 81.4% at scale 1:50 000. 67.5% at scale 1:100 000 and 98.4% at scale 1:250 000. The age of the map content is 22.4 to 37.0 years. These authoritative maps are supplemented by private attempts, such as Google Maps, Bingmaps, Here, and TomTom to extract selected features at more frequent

intervals. Locally, also OpenStreetMap provides such an opportunity.

Trends in National Mapping Development in the Russian Federation by Aleksander Prusakov: Topographic map coverage currently exists to 100% for the Russian Federation at scales 1:100 000 and 1:50 000. 35% of the Russian Federation is covered by 1:25 000 maps with an update cycle between 5 and 20 years. These maps are produced from digitized analogue maps. New cadastral real estate maps are being created by the Ministry of Economic Development with an update cycle of 5 to 7 years. These maps are the product of new aerial surveys. These maps are referenced to the new geodetic network and tied to space images.

Unresolved Issues of Map Updating by Gottfried Konecny: While map updates are possible by classical remapping at 5 to 20 year intervals, an update information is desirable at least every year. To achieve this new tools are required, such as high resolution satellite imaging on a global level and GNSS controlled mobile van and smartphone data acquisition on a local level. Obstacles are not only the data acquisition itself, but also the use of object-oriented databases in supplementation to the relational data base structure of GIS systems.

A 3D Raster GIS by Sissy Zlatanova, TU Delft: Pixel based raster systems have been used for data analysis in GIS systems since years. A 3D approach with voxels is the 3D equivalent. Voxels may be used for 3D scenes for digital terrain models, harbour construction, roads, buildings, water bodies, texture and geological bodies in CityGML. Vectors in 3D and voxels may be converted in both directions. A Monet db example was presented in a BIM application.

Fusion of Laser Scanning and UAV data by Maxim Alyntsev, SSUGT: For a 5 km highway stretch in the Novosibirsk region mobile van laser scans and UAV Supercam S250 optical images were fused with half metre accuracy for map updating.

Mapping Agricultural Lands in the Volga Delta by Ksenia A. Troshko, Lomonossov University, Moscow: From 1965 to 1987 the Volga delta had 134 Mha of arable land. After the agrarian reform of 1990 this agricultural land was transformed to fallow land and is now being reforested. Abandoned land is now subject to desertification. The process was monitored by Landsat images at critical periods of the year in 1986, 2002 and 2014.

Land Use as Factor of National Soil Cover Conservation by Aleksey V. Dubrovsky, SSUGT: For part of the Novosibirsk Region nuclear power plant environments were investigated by soil surveys.

After the conclusion of Interexpo-GeoSiberia at noon of April 22, 2016 a farewell dinner has been hosted at SSUGT.

SSUGT will participate at international events in 2016, such as the ISPRS Congress in Prague in July 2016, and at the Intergeo in Hamburg in October 2016.

SSUGT published the proceedings of this workshop under ISBN 978-5-87693-900-5 and ISBN 978-80-01-05936-4

Gottfried Konecny, Hannover

Hochschulnachrichten

Technische Universität München

Dissertation von Tessio Novack

Herr Tessio Novack, M.Sc., promovierte am 18. Februar 2016 an der Ingenieurfakultät Bau Geo Umwelt (Photogrammetrie und Fernerkundung) der Technischen Universität München mit der Arbeit *Context-based classification of urban structure types using space-borne InSAR images* zum Dr.-Ing.

1. Gutachter: Prof. Dr.-Ing. Uwe Stilla, Technische Universität München (TUM)
2. Gutachter: Prof. Dr.-Ing. Uwe Sörgel, Technische Universität Darmstadt (TUD)

Zusammenfassung:
Das unkontrollierte Wachstum der städtischen Bebauung hat verschiedene soziale und ökologische Folgen, die zu Problemen führen können. Die Erfassung urbaner Strukturen und ihre Veränderung sind zur Bereitstellung von Basisinformationen für Monitoring und Planung in den verschiedensten Bereichen, wie Stadtplanung oder Geo- und Umweltwissenschaften, von hohem Interesse. Für bestimmte Aufgabenstellungen steht jedoch nicht die detaillierte geometrische Beschreibung urbaner Objekte im Vordergrund, sondern es sind vielmehr semantische Interpretationen von aggregierten Bereichen gefragt, wie beispielsweise bei der Kartierung von Stadtstrukturtypen. Dabei erschließt sich häufig ein spezieller Stadtstrukturtyp eines Bereiches nicht nur aus den Oberflächeneigenschaften der Objekte selbst, sondern erst aus ihrem Kontext oder ihrer funktionellen Bedeutung.

Ziel der Arbeit ist es, aus hochaufgelösten Radarsatellitenbildern eine Kartierung von Stadtstrukturtypen durch kontextbasierte Klassifikation abzuleiten und deren Leistungsfähigkeit zu untersuchen. Dazu werden Stadtstrukturtypen auf Ebene von Blöcken klassifiziert, die durch Verkehrswege wie Straßen, Schienen und Flüsse eingegrenzt sind. Als Klassifikationsmethoden werden die Verfahren „Random Forest“ und „Minimum-Distance“ auf Basis von relativer Entropie eingesetzt. Zur Erhöhung der Leistungsfähigkeit der Klassifikation wird die Berücksichtigung von kontextuellen Zusammenhängen über die Nachbarschaft vorgeschlagen, welche durch probabilistische graphische Modelle beschrieben werden. Dazu werden unterschiedliche Graphenstrukturen gegenübergestellt und die Parametrisierung der Modelle beschrieben.

Für die Experimente werden vier TerraSAR-X Satellitenbilder herangezogen, die aus zwei interferometrischen Bildpaaren der aufsteigenden und absteigenden Bahn bestehen. Die Bilder decken den zentralen Teil der Stadt München in Deutschland ab. Die Untersuchung wird auf Basis der Klassifikation von fünf repräsentativen Klassen mit verschiedenen Trainingsdatensätzen durchgeführt. Es werden die Leistungsfähigkeit der Klassifikationsmethoden sowie der Einfluss der Modellparameter und der Graphenstrukturen verglichen.

Es zeigt sich, dass die gemeinsame Verwendung der Bilder von beiden Bahnen bei der Extraktion von Attributen der Blöcke zu besseren Klassifikationsergebnissen führt. Die Wahl des Klassifikationsverfahrens („Random Forest“ oder „Minimum-Distance“) hat keinen wesentlichen Einfluss auf die Ergebnisse. Durch die Berücksichtigung von kontextuellen Zusammenhängen zwischen benachbarten Blöcken wird die Genauigkeit der Klassifikation bis zu 10% erhöht, wobei die beste kontextbasierte Klassifikation eine Genauigkeit von 78% erreicht. In der Schlussbetrachtung werden die Grenzen der automatischen Ableitung von Stadtstrukturtypen aus Fernerkundungsdaten diskutiert.

Die Dissertation ist verfügbar unter:
http://www.pf.bgu.tum.de/pub/2016/novack_phd16_dis.pdf

In eigener Sache: Verlagswechsel der PFG

Vor über einem Jahr hat am 16. März 2015 die außerordentliche Mitgliederversammlung der DGPF in Köln den Weg zu einem Verlagswechsel der PFG freigemacht. Kurz danach haben der Präsident und der Hauptschriftleiter den Vertrag mit dem neuen Verlag besiegelt. Das PFG-Heft 6/2016 wird das letzte sein, das beim Schweizerbart-Verlag in Stuttgart erscheint. Mit dem PFG-Heft 1/2017 wird die neue Ära beim Springer-Verlag in Heidelberg beginnen.

Mit dem Wechsel zum Springer-Verlag kommen viele Neuerungen auf die PFG zu. Der Springer-Verlag bedient weltweit rund 400 Bibliotheken mit einem umfangreichen Zeitschriftenpaket, in dem die PFG enthalten sein wird. Redaktion und Autoren werden sich auf eine rechnerbasierte Verwaltung der eingereichten Beiträge einstellen, den Editorial-Manager. Allen Mitgliedern der DGPF steht künftig die PFG ohne zusätzliche Kosten auch online zur Verfügung.

Gerade aus dem letztgenannten Grund werden wir, der Vorstand, in den nächsten Wochen an Sie als Mitglieder herantreten und Sie um Ihre Online-Daten bitten, vor allem die E-Mail-Adressen. Diese sind Voraussetzung dafür, dass wir für Sie den Online-Zugriff auf die PFG einrichten lassen können. In vielen Fällen dürften diese Daten bei uns bereits vorliegen, wir wollen sie jedoch in jedem Fall nochmals verifizieren. Für Ihre Unterstützung darf ich mich jetzt schon ganz herzlich bedanken!

Im Laufe des Jahres werden wir an dieser Stelle nochmals auf den Verlagswechsel zurückkommen und Sie über weitere Veränderungen im Zusammenhang mit der PFG informieren.

Wolfgang Kresse, Neubrandenburg

Veranstaltungskalender

2016

6. – 9. Juni: **EUSAR 2016 – 11th European Conference on Synthetic Aperture Radar** in **Hamburg.** eusar.de

14. – 16. Juni: **geoinfo.potsdam.2016 – 64. Kartographentag und Geoinformatik 2016** in **Potsdam.** geoinfo.dgfk.net

26. Juni – 1. Juli: **CVPR 2016 – International Conference on Computer Vision and Pattern Recognition 2016** in **Las Vegas,** USA. pamitc.org/cvpr16

10. – 15. Juli: **IGARSS 2016 – International Geoscience and Remote Sensing Symposium 2015** in **Peking,** China. igarss2016.org

12. – 19. Juli: **ISPRS Congress 2016** in **Prag,** Tschechien. www.isprs2016-prague.com

14. – 16. September: **GEOBIA 2016** in **Enschede,** Niederlande. geobia2016.com

22. – 23. September: **2nd Virtual Geoscience Conference (VGC 2016)** in **Bergen,** Norwegen. virtualoutcrop.com/vgc2016

26. – 29. September: **SPIE Remote Sensing 2016** in **Edinburgh,** UK. spie.org/conferences-and-exhibitions/remote-sensing

25. – 28. September: **ICIP 2016 – International Conference on Image Processing 2016** in **Phoenix,** USA. ieeeicip2016.org

4. – 7. Oktober: **SIBGRAPI – Conference on Graphics, Patterns and Images 2016** in **São José dos Campos,** Brasilien. gibis.unifesp.br/sibgrapi16

10. – 16. Oktober: **ECCV 2016 – European Conference on Computer Vision 2016** in **Amsterdam,** Niederlande. eccv2016.org

11. – 13. Oktober: **Intergeo 2016** in **Hamburg.** intergeo.de

16. – 17. Oktober: **GeoAdvances 2016 – ISPRS Workshop on Multi-dimensional & Multi-scale Spatial Data Modeling** in **Istanbul,** Türkei. geoadvances.org/

8. – 11. November: **ICPR 2016 – International Conference on Pattern Recognition 2016** in **Cancun,** Mexiko. icpr2016.org

Weitere Konferenzen und Workshops finden sich beispielsweise unter:
isprs.org/calendar/Default.aspx
conferences.visionbib.com

Korporative Mitglieder

Firmen

AEROWEST GmbH
AICON 3D Systems GmbH
aphos Leipzig AG
Bernhard Harzer Verlag GmbH
Blom Deutschland GmbH
Brockmann Consult GmbH
bsf swissphoto GmbH
Ing. Büro Dr. Carls, Luftbilddatenbank
DELPHI IMM GmbH
Deutsches Bergbau-Museum
EFTAS Fernerkundung Technologietransfer GmbH
ESG Elektroniksystem- und Logistik-GmbH
Esri Deutschland GmbH
EUROPEAN SPACE IMAGING
Eurosense GmbH
Exelis Visual Information Solutions GmbH
fokus GmbH
GAF GmbH
GeoCart Herten GmbH
Geoinform. & Photogr. Engin. Dr. Kruck & Co. GbR
geoplana Ingenieurgesellschaft mbH
GEOSYSTEMS GmbH
GGS - Büro für Geotechnik, Geoinformatik, Service
Hansa Luftbild AG
IAGB mbH
IGI - Ingenieur-Gesellschaft für Interfaces mbH
ILV-Fernerkundungs GmbH
Infoterra GmbH
INVERS - Industrievermessung & Systeme
Leica Geosystems Technologies GmbH
Linsinger ZT GmbH
Messbildstelle GmbH
MILAN Geoservice GmbH
M.O.S.S. Computer Grafik Systeme GmbH
PHOENICS GmbH
Planet Labs Germany GmbH
PMS - Photo Mess Systeme AG
RIEGL Laser Measurement Systems GmbH
RWE Power AG, Geobasisdaten/Markscheidewesen
technet GmbH
Terra-Messflug GmbH
topometric GmbH
TRIGIS GmbH
Trimble Germany GmbH
trimetric 3D Service GmbH
VDE Verlag GmbH, Herbert Wichmann Verlag
VEXCEL Imaging GmbH

Behörden

Bayerische Landesanstalt für Wald und Forstwirtschaft
Bundesamt für Kartographie und Geodäsie
Bundesministerium für Ernährung, Landwirtschaft und Verbraucherschutz
DB Netz AG
Hessisches LA für Bodenmanagement und Geoinformation
Innenministerium NRW, Gruppe Vermessungswesen
Institut für Umwelt- und Zukunftsforschung
LA für Digitalisierung, Breitband, Vermessung und Geoinformation, Bayern
LA für Geoinformation und Landentwicklung, BW
LA für Vermessung und Geoinformation, Schleswig-Holstein
LB Geoinformation und Vermessung, Hamburg
LB für Küstenschutz, Nationalpark und Meeresschutz, SH
Landeshauptstadt Düsseldorf, Vermessungs- und Liegenschaftsamt
Landesvermessung und Geobasisinformation Niedersachsen
Märkischer Kreis, Vermessungs- und Katasteramt
Regierungspräsident Tübingen, Abt. 8 Forstdirektion
Regionalverband Ruhr
Staatsbetrieb Sachsenforst
Stadt Köln, Amt für Liegenschaften, Vermessung und Kataster
Stadt Wuppertal, Vermessung, Katasteramt und Geodaten
Thüringer LA für Vermessung und Geoinformation
Zentrum für Geoinformationswesen der Bundeswehr

Hochschulen

BTU Cottbus, Lehrstuhl für Vermessungskunde
FH Frankfurt a.M., FB 1, Studiengang Geoinformation
FH Mainz, Institut für Raumbezogene Informations- und Messtechnik
HCU HafenCity Universität Hamburg, Geomatik
HfT Stuttgart, Vermessung und Geoinformatik
HS Bochum, FB Vermessung und Geoinformatik
HS Karlsruhe für Technik und Wirtschaft, Fakultät für Geomatik
HTW Dresden, FB Vermessungswesen/Kartographie
Jade Hochschule, Institut für Angewandte Photogrammetrie und Geoinformatik
LUH Hannover, Institut für Kartographie und Geoinformatik
LUH Hannover, Institut für Photogrammetrie und Geoinformation
MLU Halle, FG Geofernerkundung
Rhein Ahr Campus, Anwendungszentrum für multimodale und luftgestützte Sensorik
Ruhr-Uni Bochum, Geographisches Institut
RWTH Aachen, Geodätisches Institut
TU Bergakademie Freiberg, Institut für Markscheidewesen und Geodäsie
TU Berlin, Computer Vision & Remote Sensing
TU Berlin, Institut für Geodäsie und Geoinformationstechnik
TU Braunschweig, Institut für Geodäsie und Photogrammetrie
TU Clausthal, Institut für Geotechnik und Markscheidewesen
TU Darmstadt, Institut für Geodäsie, FG Fernerkundung und Bildanalyse
TU Dresden, Institut für Photogrammetrie und Fernerkundung
TU München, FG Photogrammetrie und Fernerkundung
TU München, Lehrstuhl für Geoinformatik
TU Wien, Department für Geodäsie und Geoinformation
Uni Bonn, Institut für Photogrammetrie
Uni Göttingen, Abt. Waldinventur und Fernerkundung
Uni Heidelberg, IWR Interdisziplinäres Zentrum für Wissenschaftliches Rechnen
Uni Kassel, FG Grünlandwissenschaften und Rohstoffe
Uni Kiel, Geographisches Institut
Uni Stuttgart, Institut für Photogrammetrie
Uni Trier, Institut für Umweltfernerkundung und Geoinformatik
Uni Würzburg, Geographisches Institut
Uni zu Köln, Geographisches Institut